NATIONAL AERONAUTICS AND SPACE ADMINISTRATION

Technical Report No. 32-1023

Surveyor I Mission Report

Part II. Scientific Data and Results

L. D. Jaffe, E. M. Shoemaker, S. E. Dwornik, J. J. Rennilson, J. L. Dragg, E. C. Morris, A. Turkevich, J. W. Lucas, J. E. Conel, R. R. Garipay, W. A. Hagemeyer, J. M. Saari, W. E. Brown, E. M. Christensen, S. A. Batterson, H. E. Benson, C. E. Chandler, R. H. Jones, R. F. Scott, E. N. Shipley, F. B. Sperling, G. H. Sutton, R. H. Norton, J. E. Gunn, W. C. Livingston, G. A. Newkirk, H. Zirin

JET PROPULSION LABORATORY
CALIFORNIA INSTITUTE OF TECHNOLOGY
PASADENA, CALIFORNIA

September 10, 1966

NATIONAL AERONAUTICS AND SPACE ADMINISTRATION

Technical Report No. 32-1023

Surveyor I Mission Report

Part II. Scientific Data and Results

L. D. Jaffe, E. M. Shoemaker, S. E. Dwornik, J. J. Rennilson, J. L. Dragg, E. C. Morris, A. Turkevich, J. W. Lucas, J. E. Conel, R. R. Garipay, W. A. Hagemeyer, J. M. Saari, W. E. Brown, E. M. Christensen, S. A. Batterson, H. E. Benson, C. E. Chandler, R. H. Jones, R. F. Scott, E. N. Shipley, F. B. Sperling, G. H. Sutton, R. H. Norton, J. E. Gunn, W. C. Livingston, G. A. Newkirk, H. Zirin

Approved by:

R J Parks

R. J. Parks, *Surveyor*
Project Manager

JET PROPULSION LABORATORY
CALIFORNIA INSTITUTE OF TECHNOLOGY
PASADENA, CALIFORNIA

September 10, 1966

Prepared Under Contract No. NAS 7-100
National Aeronautics & Space Administration

CONTENTS

CONTENTS (Cont'd)

TABLES

FIGURES

FIGURES (Cont'd)

FIGURES (Cont'd)

FIGURES (Cont'd)

PREFACE

This three-part document constitutes the Project Mission Report on *Surveyor I*, the first in a series of unmanned lunar soft-landing missions.

Part I of this Technical Report consists of a technical description and an evaluation of engineering results of the systems used in the *Surveyor I* mission. Part II presents the scientific data derived from the mission, and the scientific analysis conducted by the members of the *Surveyor* Scientific Evaluation and Analysis Team and the five associated working groups. Part III consists of selected pictures from *Surveyor I* and appropriate explanatory material.

The results given in this report are based upon data evaluation prior to September 10, 1966. It is expected that future evaluation and analysis of the *Surveyor I* data will provide additional scientific results.

I. SUMMARY

L. D. Jaffe and E. M. Shoemaker

Although *Surveyor I* did not carry any instrumentation for scientific experiments, considerable scientific information has been obtained from it. Over 11,000 pictures were taken by the TV camera during 2 lunar days after landing, and the lunar surface was observed through sun elevation angles ranging from 0.5° to approximately 88°.

Surveyor I landed on a dark, relatively smooth mare surface, encircled by hills and low mountains. The crestlines of a few of these low mountains are visible along the horizon. By comparison of the features observed by means of the TV camera with telescopic photographs of the region around the landing site, the position of the spacecraft was found to be 2.53°S, 43.32°W, in good agreement with data obtained by radio tracking from the surface. Observations of Sirius, Canopus, and Jupiter and of numerous points on the horizon show that the general slope at the terrain around the landing site is less than 3°.

Within 1 to 2 km surrounding the *Surveyor I* landing site, the lunar surface is gently rolling and studded with craters from a few centimeters to several hundred meters in diameter, and contains angular fragments that range in size from less than 1 mm to more than 1 m. The size–frequency distribution of the smaller craters is close to that predicted for an average mare surface by extrapolation of the crater size–frequency distributions observed in *Ranger* pictures. The larger craters observed resemble those seen in the *Ranger* photographs in both shape and spatial distribution.

The surface is composed of granular material of a wide size range; coarse blocks of rock and smaller fragments are set in a matrix of fine particles too small to be resolved. Observed angular fragments occupy approximately 8% of the surface area and have a volumetric median grain size of 130 mm. The volumetric median grain size of all fragmental material on the surface is much smaller, probably 1 mm or less.

Fragmental material was thrown out, pushed aside, and compressed under the spacecraft footpads and blocks during the landing; the footpads penetrated 3 to 8 cm into the surface. Further deformation under the weight of the

spacecraft, after it had come to rest, was not detected. Measurements of forces between the surface and the landing gear during touchdown, together with observations of the deformation so produced, indicate that the dynamic bearing resistance of the lunar surface was 4×10^5 to 7×10^5 dynes/cm^2 (6 to 10 psi) at the *Surveyor* touchdown velocity of 3.6 m/sec (11.6 ft/sec). The imprints left by the footpads and blocks and the shapes of small natural craters in the field of view show that the surface material has appreciable cohesion, but probably less than 10^5 dynes/cm^2. Clods were produced by the interaction of the footpads with the surface. The mechanical behavior of the lunar surface appears qualitatively similar to that of a damp, fine-grained terrestrial soil.

Near the spacecraft, the weakly cohesive material occurs as a layer that extends to an average depth of about 1 m, as indicated by the rim characteristics of craters that have been formed in the layer, and of larger craters that have penetrated the layer. This material is probably composed of fragments of a wide range of sizes, similar to those observed directly at the surface.

The local photometric function of the lunar surface was estimated from approximately 12 photometric target areas selected in a pattern around the spacecraft. The normal albedo of the lunar surface around the spacecraft is about 6%.

The brightness temperature of the lunar surface near the landing site was determined from measurements of spacecraft temperatures. From local noon to after sunset, it varied generally as expected for a thermal parameter between 250 and 1000. Some deviation during local forenoon may be attributed to directional thermal emission from the surface. Spacecraft thermal behavior indicated that the external spacecraft surfaces were not covered with dust.

The radar cross section of the lunar surface at 2.2- to 3.2-cm wavelength, measured over regions about 30 km to 4 m in diameter, was approximately as expected from earth-based measurements. An enhanced reflection is attributed to a crater-like surface anomaly about 2 km from the landing site. Echo was returned by the visible surface, or within 60 cm of the surface.

Solar photographs made from the lunar surface showed the corona out to at least 3 or 4 solar radii. The possible scattering of sunlight from a lunar atmosphere is being investigated.

II. INTRODUCTION

L. D. Jaffe and S. E. Dwornik

Surveyor I was launched from Cape Kennedy, Florida, on May 30, 1966, at 14:41:01 GMT. The primary objective of this flight was to demonstrate the capability of the spacecraft, launch vehicle, and ground stations to accomplish a flight that included soft-landing on the moon. The secondary objective was to obtain engineering data concerning the spacecraft performance during flight and on the lunar surface; tertiary objectives were to obtain post-landing TV pictures of a spacecraft footpad and surrounding lunar surface material and of the lunar topography, and to acquire data on the radar reflectivity and bearing strength of the lunar surface, and on spacecraft temperatures for use in the analysis of lunar surface temperatures.

This spacecraft was the first of a series of engineering models designed for soft-landing on the moon. The spacecraft carried a TV system, designed for operation on the lunar surface, and more than 100 engineering sensors, including resistance thermometers, voltage sensors, strain gages, accelerometers, and position indicators for movable spacecraft parts. No instrumentation for scientific experiments was carried.

The *Surveyor I* spacecraft configuration is shown in Fig. II-1. The main structure is of tubular aluminum; attached to it are three hinged landing legs, each with a landing pad and shock absorber. Two thermally controlled compartments house the electronic equipment. A vertical mast carries the movable solar panel and high-gain planar array antenna. Two deployable omnidirectional antennas are also available for communication.

Surveyor was launched directly into a lunar impact trajectory by an *Atlas–Centaur* launch vehicle. During cruise flight, *Surveyor* obtained attitude references from sun and Canopus sensors and from gyroscopes; small nitrogen thrusters provided attitude control. A midcourse maneuver was executed on May 31, 1966, using three liquid-fueled vernier propulsion engines. For the terminal descent, the solid-fuel main retro engine was ignited at a radar altitude signal. The vernier engines, each throttlable from 104 to 30 lb (460 to 120 newtons) thrust, provided attitude control during main engine firing. After main engine burnout and jettison, the vernier engines slowed the spacecraft under control of an autopilot and on-board computer, using radar measurements of altitude

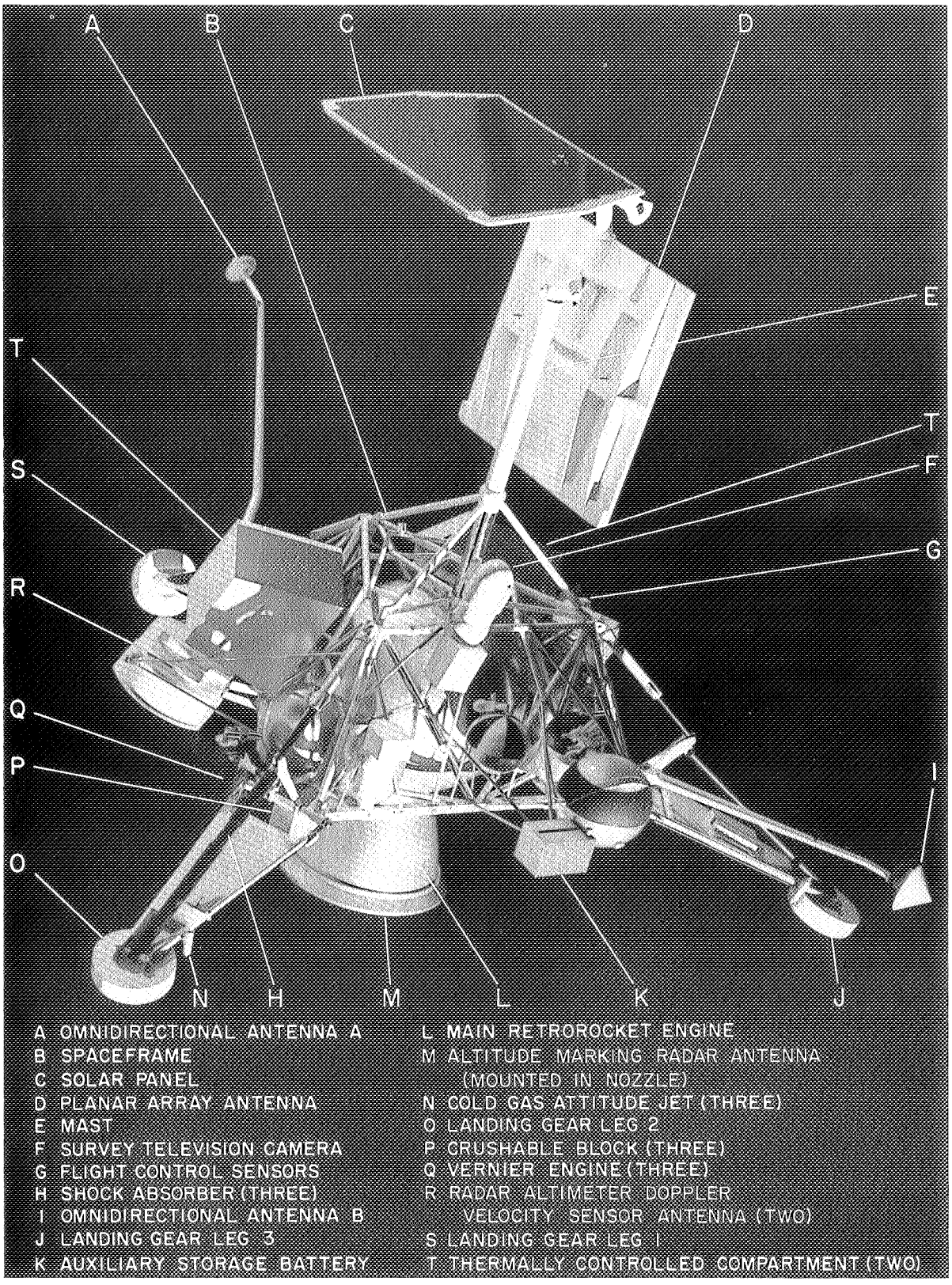

Fig. II-1. *Surveyor I* spacecraft configuration

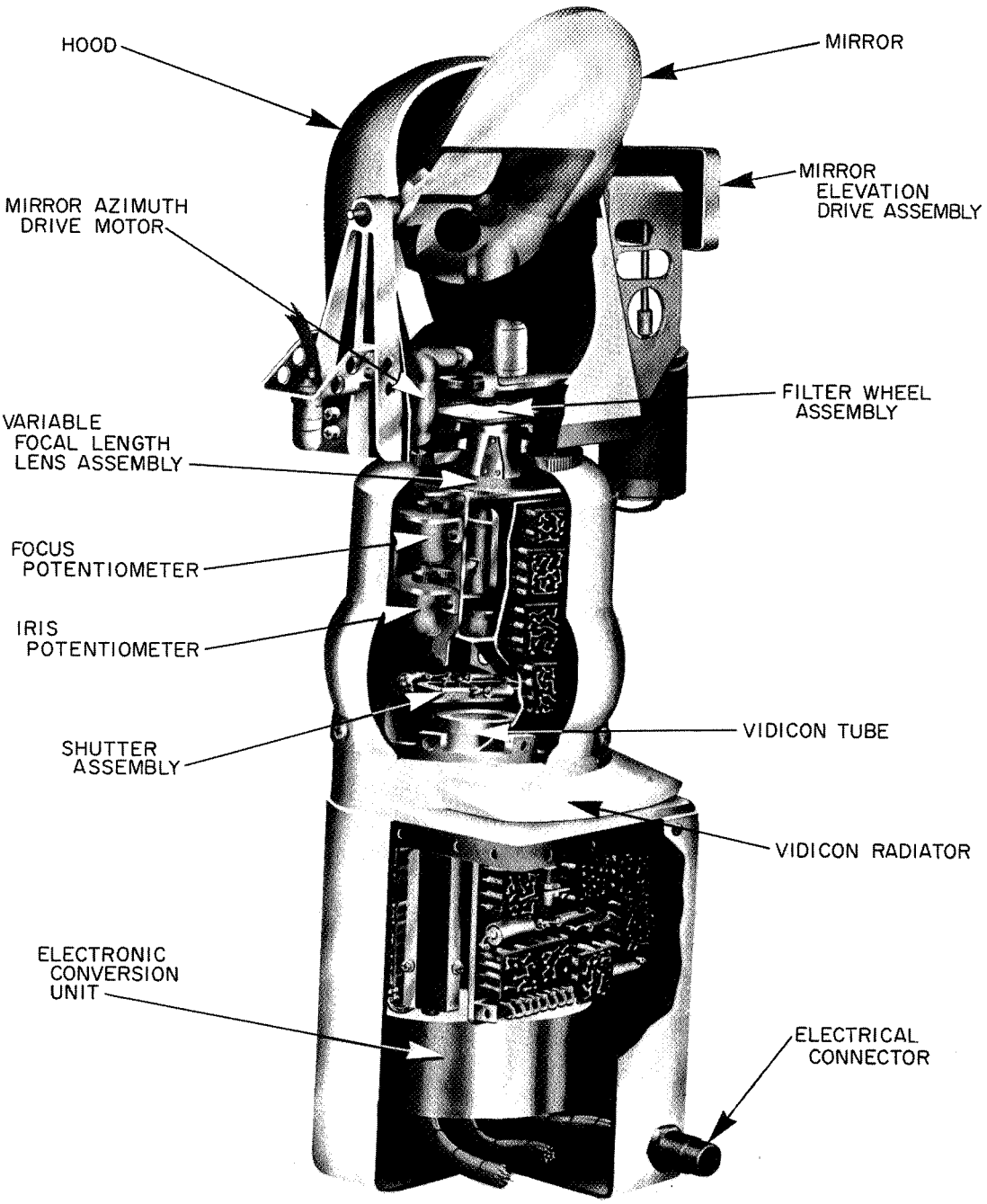

Fig. II-2. *Surveyor* TV camera

and velocity in a closed-loop system. The vernier engines were turned off, when the spacecraft altitude was 3.4 m (11 ft) and approach velocity was 1.5 m/sec (4.5 ft/sec), to reduce disturbance of the landing area by engine exhaust. From this height, the spacecraft fell freely to the lunar surface and landed on June 2, 1966, at 06:17:37 GMT. It weighed 2193 lb at launch (mass 990 kg) and 643 lb (earth weight; mass 292 kg) at touchdown; this weight difference was due to utilized propellants, attitude control gas, and the jettisoned main retro engine and altitude marking radar.

The lunar area selected for the landing of *Surveyor I* was the floor of an unnamed crater about 100 km in diameter, which appeared to be filled with mare material. Flamsteed lies on the southern edge of this crater, which is centered about 3°S and 44°W. The name "von Karman" is suggested for this crater in honor of Theodore von Karman, who initiated the program of rocket and space vehicle development that led to *Surveyor*. This area was chosen as a landing site because:

(1) From earth-based observation, it appeared to be relatively flat, contained few visible craters or rilles, and showed little coverage by rays.

(2) It was near the point of vertical descent for *Surveyor* trajectories.

(3) It was within the landing zone of interest for *Apollo* landings.

(4) The sun was fairly low over this area (28° elevation) at the expected time of landing.

During the flight, the estimated error circle for the landing point was reduced to about 60-km diameter (3 standard deviations). Accordingly, the aim was adjusted slightly northward for the midcourse maneuver, bringing the target area away from Flamsteed itself and into the northern half of the 100-km crater.

The TV camera used on *Surveyor I* is shown in Fig. II-2. The vidicon tube, lenses, shutter, filter, and iris were mounted along an axis inclined approximately 16° to the central axis of the spacecraft; they were topped by a mirror that could be turned in azimuth and elevation. The azimuth, elevation, focal length, focus, exposure, iris, and filter were adjusted as needed by commands from earth. The first picture, using 200 scan lines, was taken on June 2, 1966, at 06:53 GMT and was transmitted over an omnidirectional antenna. After 14 pictures were taken in this way, the directional antenna was oriented toward earth so that 600-line pictures could be transmitted. Over 11,000 pictures from the lunar surface were obtained.

TV operations were usually commanded, and pictures received, by the Deep Space Station (DSS 11) at Goldstone, California. Some picture sequences were conducted through the Deep Space Stations near Canberra, Australia (DSS 42) and at Johannesburg, South Africa (DSS 51), which served as prime stations for tracking and receiving engineering telemetry. Other stations at Madrid, Spain (DSS 61) and Goldstone (DSS 14 and DSS 12) provided some receiving capability.

Surveyor I operated throughout the local lunar day ending June 14, 1966; it was shut down most of the ensuing lunar night, but was turned on again the next lunar day and operated until the next sunset on July 14, 1966. The engineering features of the operation are described in Ref. II-1.

The *Surveyor* Project is supported by the National Aeronautics and Space Administration. The Jet Propulsion Laboratory, California Institute of Technology, is responsible for project management; the Hughes Aircraft Company is responsible for *Surveyor* spacecraft design and fabrication.

REFERENCE

II-1. *Surveyor I Mission Report: Part I. Mission Description and Performance*, Technical Report No. 32-1023, Jet Propulsion Laboratory, Pasadena, Calif., August 31, 1966.

III. LUNAR SURFACE TOPOGRAPHY

J. J. Rennilson, J. L. Dragg, E. C. Morris, E. M. Shoemaker, and A. Turkevich

Over 11,000 pictures have been taken by the TV camera on the *Surveyor I* spacecraft during the 2 lunar days after landing. The lunar surface has been observed through sun elevation angles ranging from 0.5 to approximately 88°.

During the first lunar day, from lunar sunrise to lunar noon, pictures were taken at sun elevation angles from 28 to 88°. No pictures were taken during the early afternoon because the temperatures were too high for camera operation. The operation of the camera was resumed at a sun elevation of 78° and continued until after sunset. One picture of footpad 2 and the surrounding lunar surface was taken by earthshine approximately 54 min after sunset. Because of temperature and battery problems, only 821 pictures were taken during the second lunar day. These pictures were obtained during the lunar afternoon with sun elevation angles ranging from about 0 to 20°.

The *Surveyor* TV camera was operated in two modes: one in which the picture is composed of 200 TV scan lines, and a second, higher-resolution mode, in which the picture is composed of 600 scan lines. From the total of over 11,000 pictures taken, 23 were in the 200-line mode; the remainder, in the 600-line mode, are of superior quality and may be compared favorably with the lunar TV pictures acquired by the *Ranger* spacecraft. The pictures taken by *Surveyor* are exceptionally free of coherent noise and show very little shading of the field because of the relatively uniform response of the vidicon target.

The calibrated angular resolution of the *Surveyor* camera (0.5 mr at 15% relative response) is approximately half the angular resolution of the human eye. Near one of the spacecraft footpads, 1.6 m from the camera, as measured from pictures for which the modulation transfer function has been compensated (Fig. III-1), the ground resolution is about 0.5 mm. Higher ground resolution can be achieved directly beneath the camera. It is of interest to note that the highest resolution obtained in the *Ranger* pictures represents an improvement by three orders of magnitude over the best resolution of the lunar surface achieved by the telescope, and that the *Surveyor* pictures represent a gain in resolution by an additional three

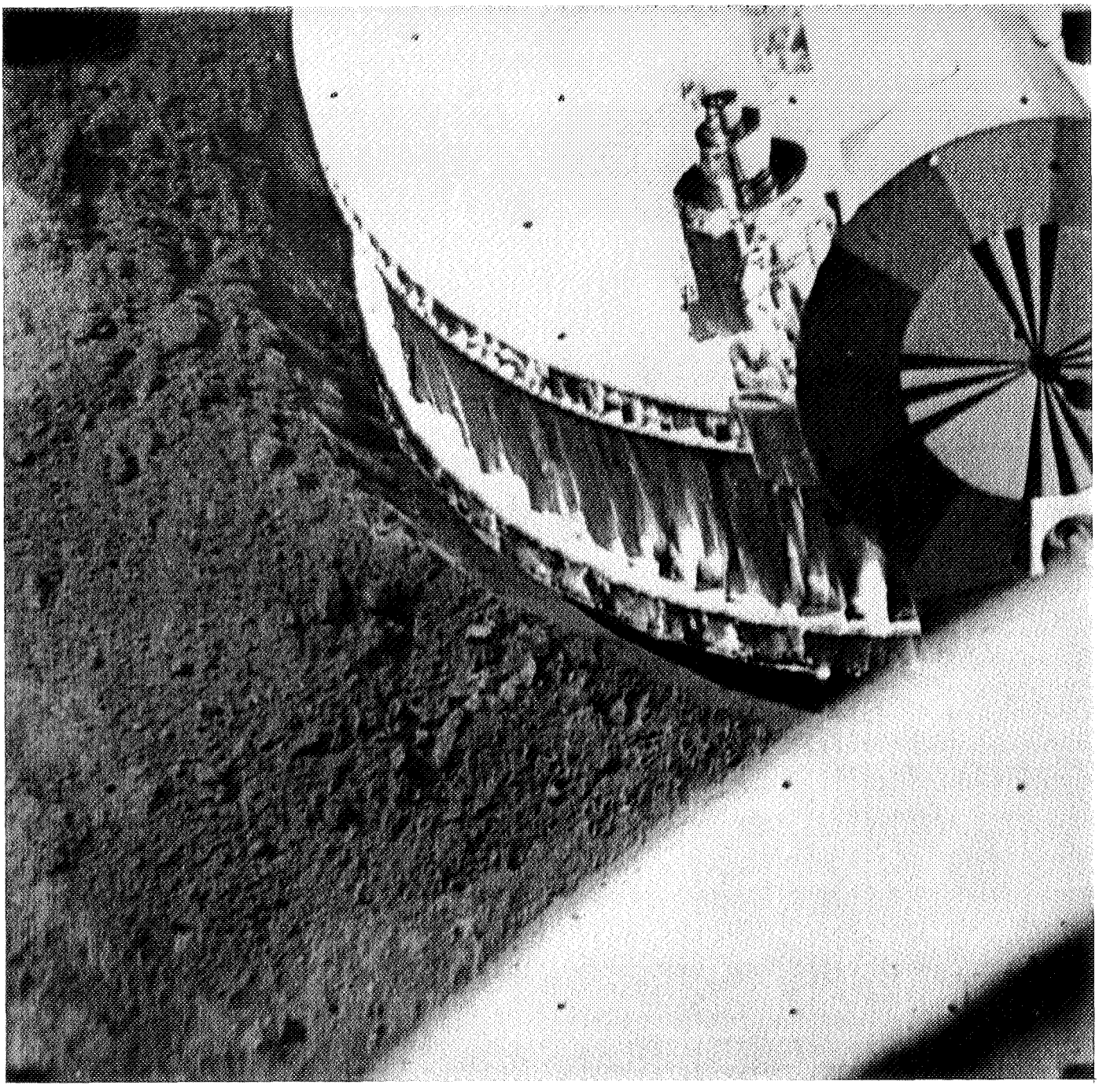

Fig. III-1. Narrow-angle picture of footpad 2

orders of magnitude over the highest-resolution *Ranger* pictures. The *Surveyor I* TV pictures exhibit a significant gain in resolution over the pictures acquired this year by the Soviet spacecraft, *Luna 9*.

The total range of response of the *Surveyor I* camera is approximately 1,000,000 to 1, which enables it to record stars as faint as sixth magnitude, and to photograph the brightest parts of the lunar surface. Thus, the dynamic range of the *Surveyor* TV camera is within a factor of 10 of the dynamic range of the human eye. Photometric response of the *Surveyor I* camera on the moon, observed by means of repeated pictures of a photometric calibration target mounted on a leg of the spacecraft, has proved

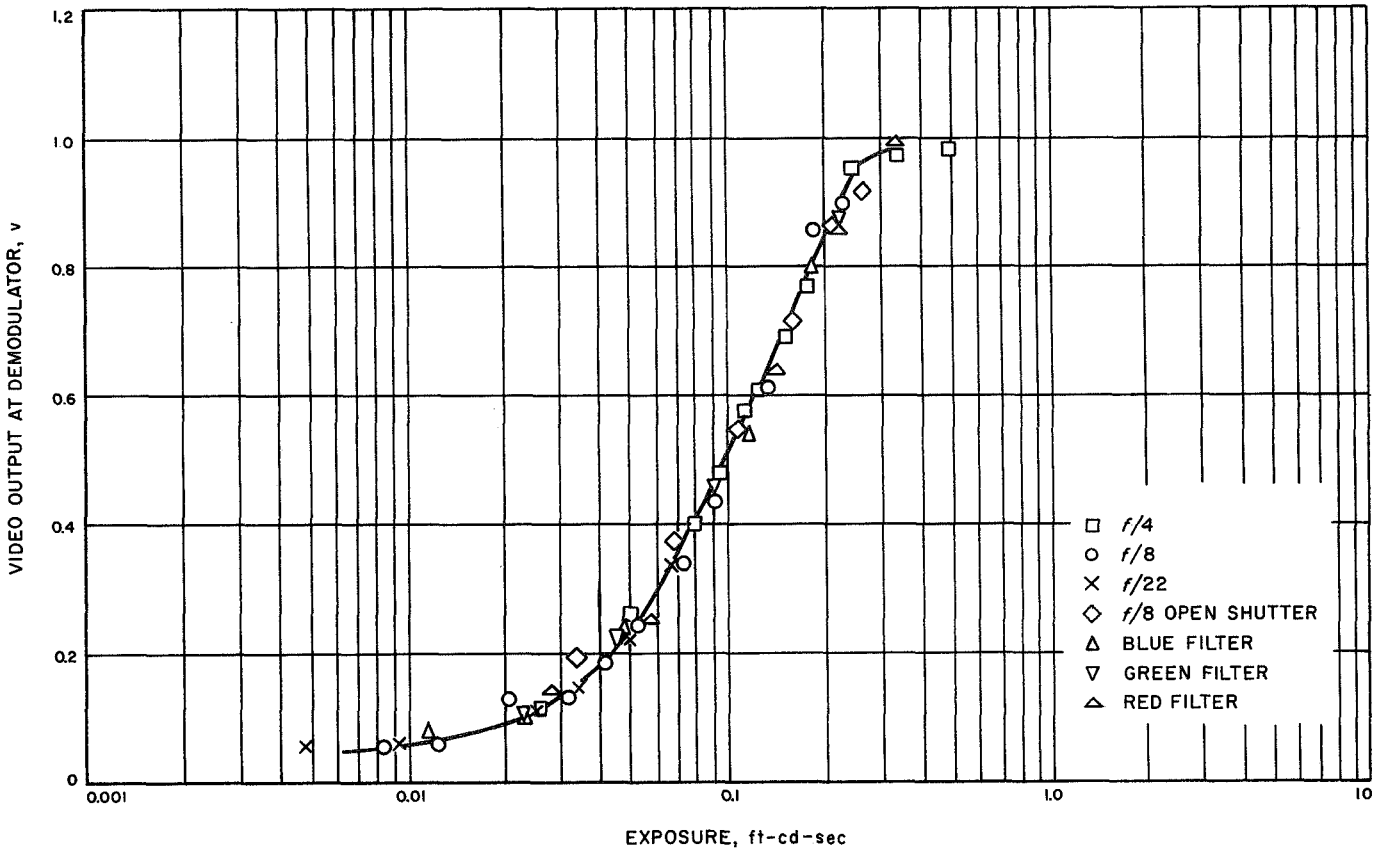

Fig. III-2. Calibration data for *Surveyor I* TV camera, showing dynamic range

to be fairly stable and close to the response observed in preflight calibrations. In its normal mode of shutter operation, which provides a 150-msec exposure, the total dynamic range of the vidicon tube is approximately 25 to 1; the logarithm of the video voltage is nearly a linear function of the logarithmic lunar scene luminance over a range of about 5 to 1 (Fig. III-2).

The great dynamic range of the camera system is achieved by means of an iris, filters in the optical train, and alternate modes of shutter operation and electron-beam scanning cycle. By using the variable iris aperture, which provides nominal focal ratios from $f/4$ to $f/22$, the dynamic range of the camera is increased from 25 to 1 to somewhat more than 800 to 1. Rotation into the optical train of color filters on a camera-filter wheel can be used to increase the dynamic range to approximately 3000 to 1. By using a 1.2-sec exposure (open-shutter mode), the dynamic range of the camera can be extended to about 25,000 to 1; the sensitivity of the camera to very faint objects can be increased even more, by a factor of about 40 over the open-shutter mode, by means of several minutes of exposure (integration mode).

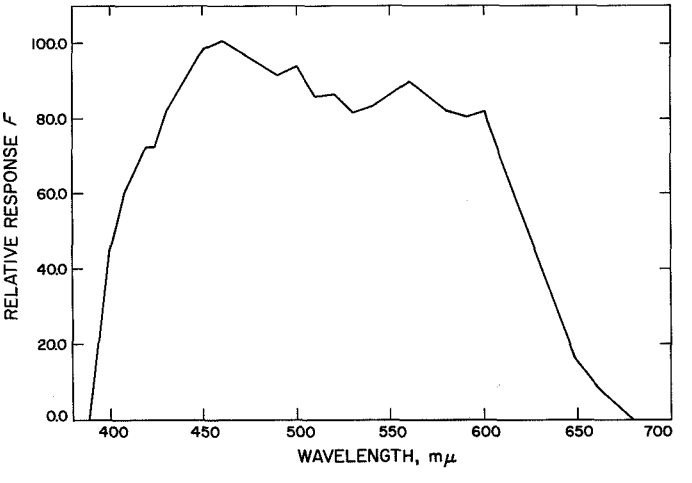

Fig. III-3. Spectral response curve of *Surveyor I* TV camera at clear position of filter wheel

The color filters in the camera-filter wheel were selected so that the overall camera-filter spectral response (Fig. III-3) would duplicate the standard color-matching functions of colorimetry as well as possible using single filters. Figure III-4 is a graph of the overall camera-filter

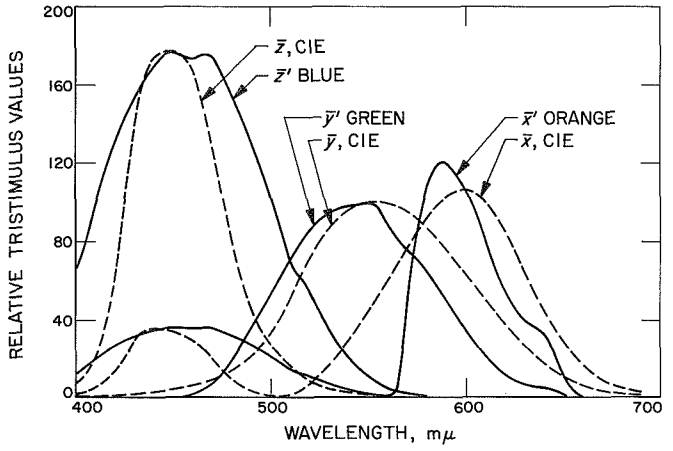

Fig. III-4. Overall camera-filter spectral response

spectral response showing the fit to the standard Commission Internationale d'Eclairage 1931 (CIE) color-matching functions. In this figure, the second maximum in the $\bar{x}'$ curve is obtained from a reduced value of the $\bar{z}'$ function added to the original camera-filter response. The solid lines are camera-filter response curves; the dashed lines are the CIE color-matching functions. In order to maintain colorimetric calibration and to enhance the detection of color differences, the photometric target is equipped with three colors of purity and dominant wavelength that bound the range of normal rock colors. Figure III-5 (a), (b), and (c) shows the appearance of the target as seen through the three color filters.

The lens assembly of the *Surveyor* TV camera is constructed to provide a variable focal length that ranges from 25 to 100 mm and is normally operated at either the long or short focal-length extreme. The 25-mm focal length results in a 25.3° field of view, and the 100-mm focal length provides a 6.4° field of view. For convenience, the former is referred to as a wide-angle frame; the latter is referred to as a narrow-angle frame.

The camera has been operated to provide a great variety of information. Wide-angle panoramas have been taken of the lunar scene on different days and with different color filters. (A complete wide-angle panorama requires about 120 frames.) All sectors of the complete panorama have also been taken in narrow-angle frames on different days and with different color filters. (A complete narrow-angle panorama requires about 1000 frames.) Surveys have been conducted of two of the spacecraft footpads and of lunar surface imprints left by crushable blocks beneath the frame of the spacecraft. On 2 days, the attitude-control jets, mounted on the legs of the spacecraft, were fired in an experiment to determine whether the emitted gas would disturb the surface; the results were sought by comparing the TV pictures taken during and after the firing of the jets with the pictures taken before. To provide control for the photometric reduction of the pictures, repeated photographs were taken of the photometric and color calibration target on each earth day. Objects of special interest, such as large rocks close to the spacecraft, were examined by means of additional photographic coverage in order to provide maximum information on the shape, texture, and color of these objects.

To measure the photometric function of the local lunar surface and of various objects on the surface and to map the surface topographically by the use of shadows and by photometric techniques, the surface must be surveyed repeatedly at different elevations of the sun. At different angles of solar illumination, different kinds of information are provided about the surface. The fine texture and very shallow relief features are best seen at low sun elevation angles, whereas differences in albedo and color are best determined when the sun is high or when the phase angle of a given image element is very small.

A. Landscape Features on Horizon

At least five features in the *Surveyor* panoramic pictures can be identified as distant elevated terrain; these features lie beyond the near horizon, which is approximately 2 km from the spacecraft (Fig. III-6). A low mountain ridge to the northeast is an outstanding example. The horizon in front of the distant features can generally be identified by a relatively sharp demarcation between the foreground and the distant elevated terrain, which is brighter than the foreground and smoother in silhouette. All distant features recognized lie north of the spacecraft.

Pictures taken during the late afternoon of the first and second lunar days revealed some details in the hills comprising feature A (Fig. III-7), which is composed of at least two main parts. The westernmost part is a separate hill that lies in front of the eastern part. The approximate position of some of the details in the separate components of this feature are listed in Table III-1.

Pictures, taken 32 days apart, of the eastern part of feature A provided one of the most sensitive tests of stability of the attitude of the spacecraft on the moon. The position of reseau marks superimposed on this terrain feature did not change more than 0.2° over this period of time.

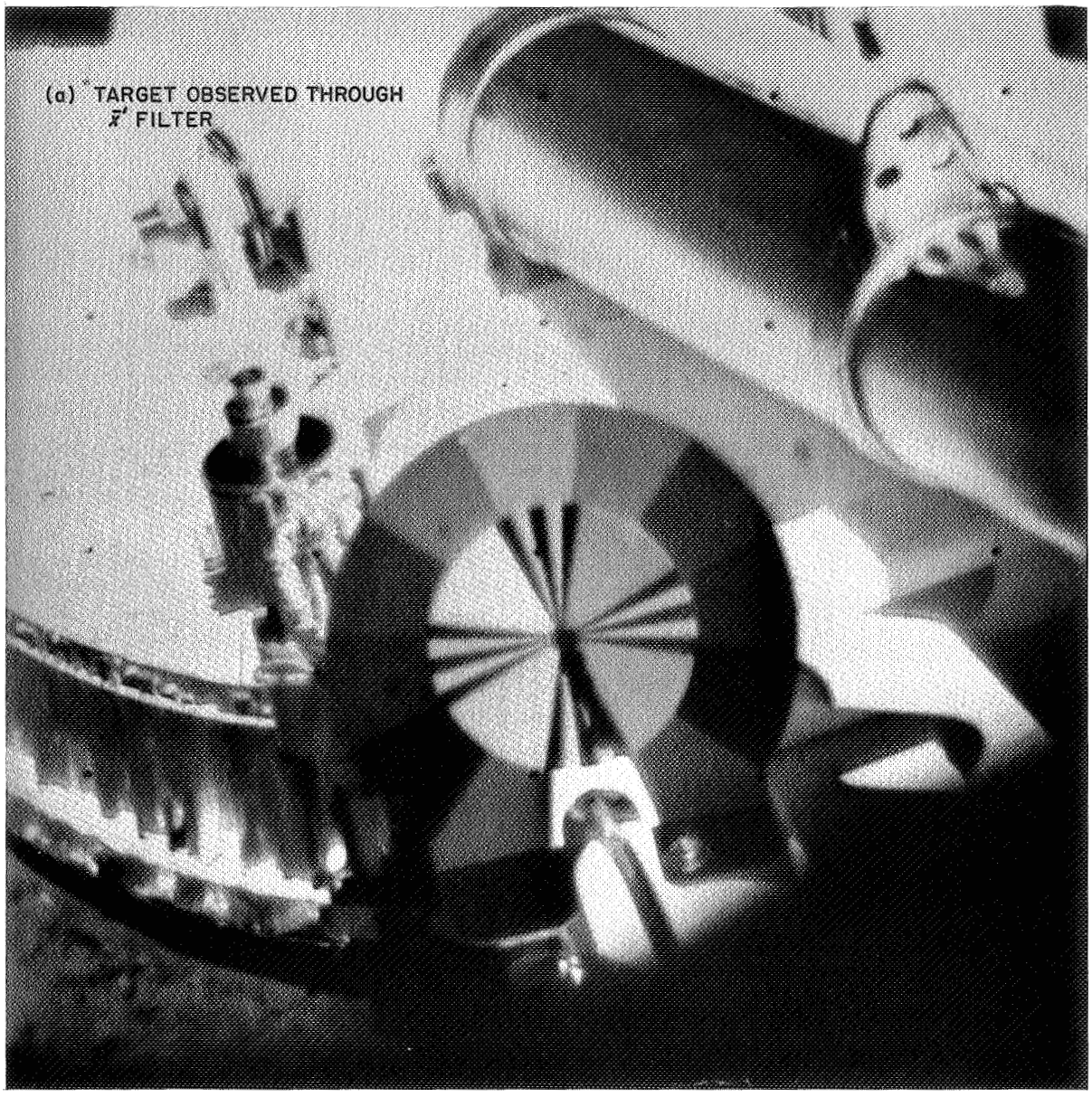

Fig. III-5. Photometric target on footpad 2

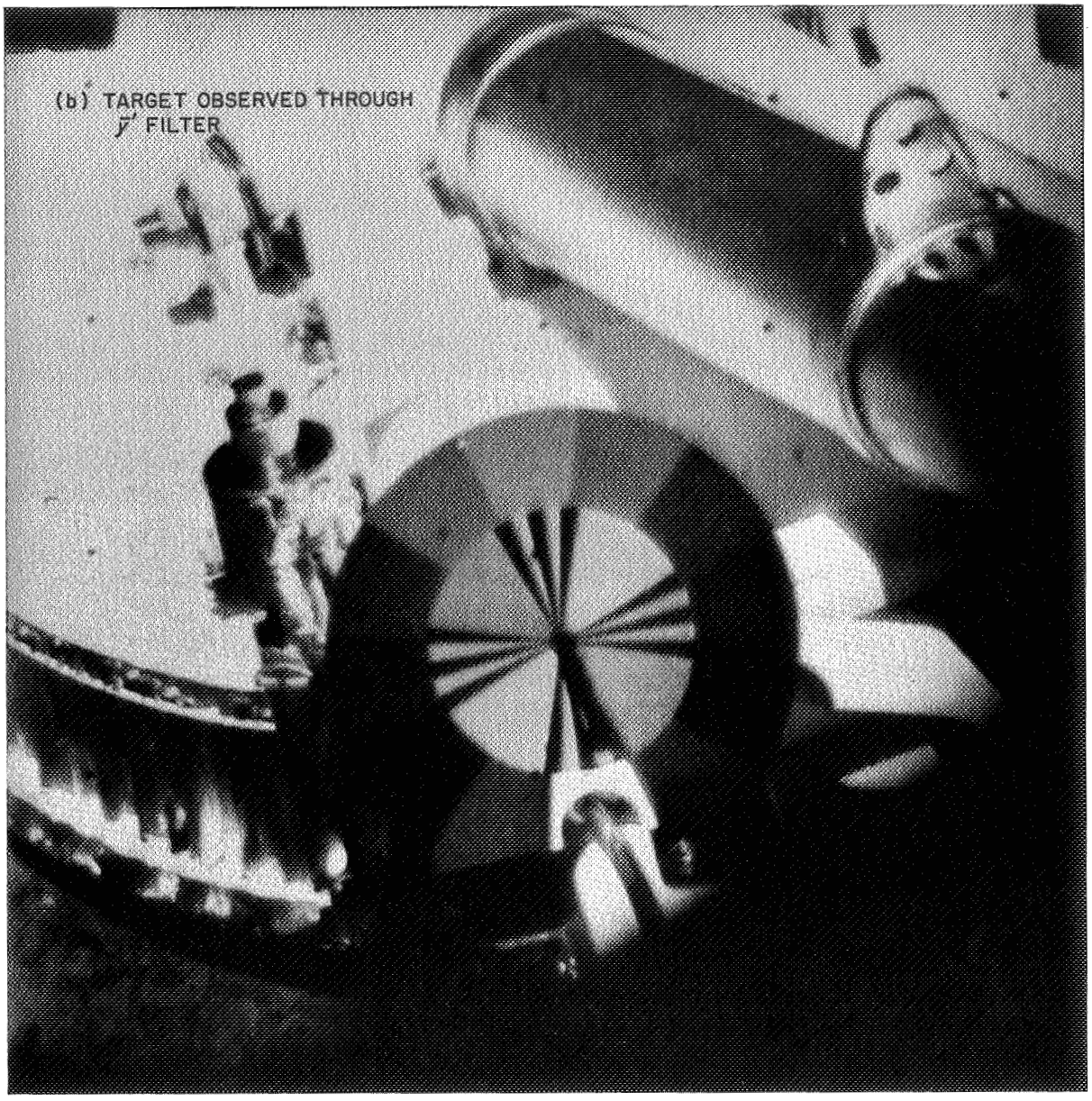

Fig. III-5. Photometric target on footpad 2 (cont'd)

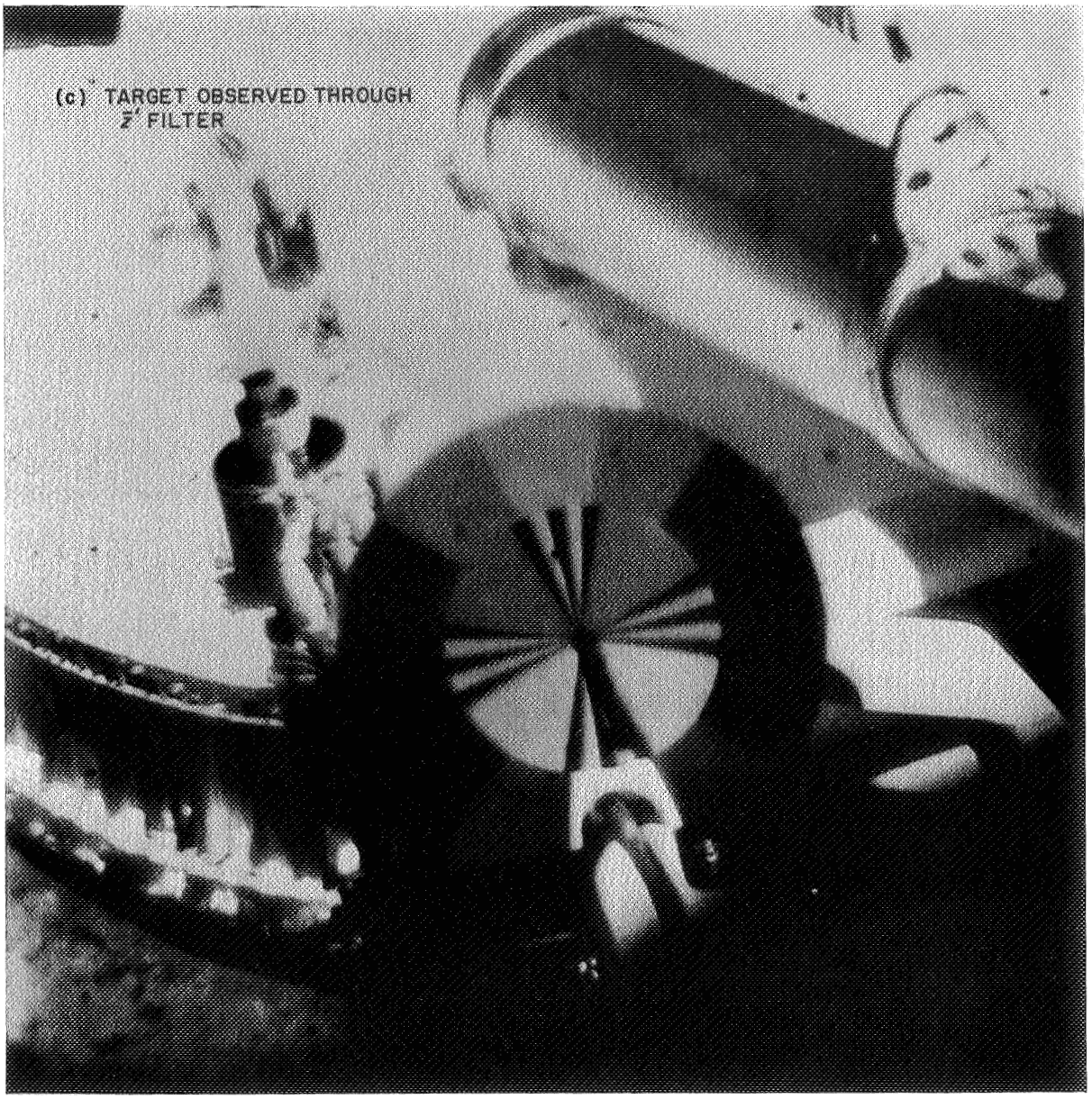

Fig. III-5. Photometric target on footpad 2 (cont'd)

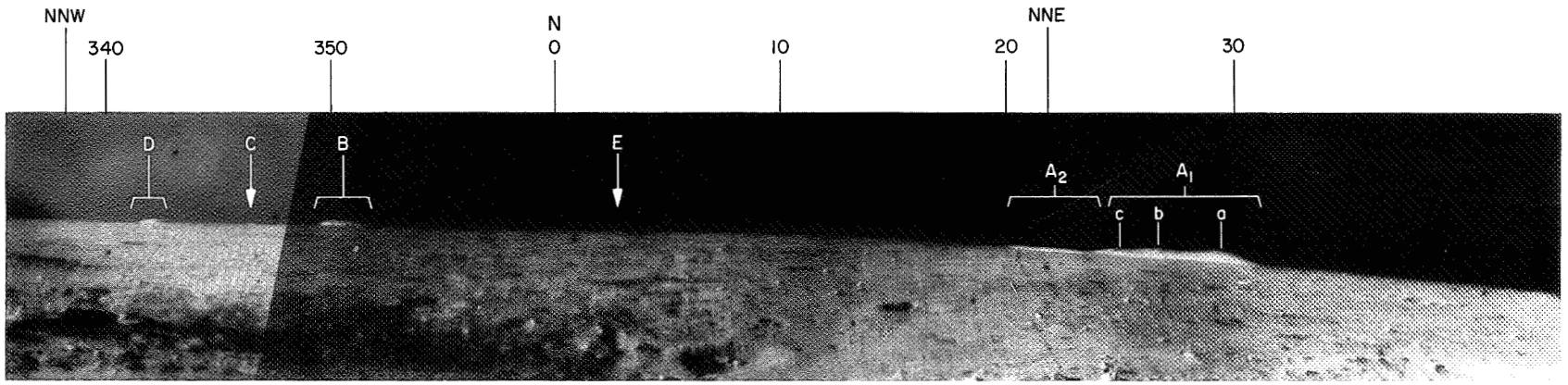

Fig. III-6. Wide-angle panorama of lunar horizon in northern quadrant, as observed by *Surveyor I*. (Sun angle is approximately 15°; most of the curvature at the horizon is a result of camera inclination.)

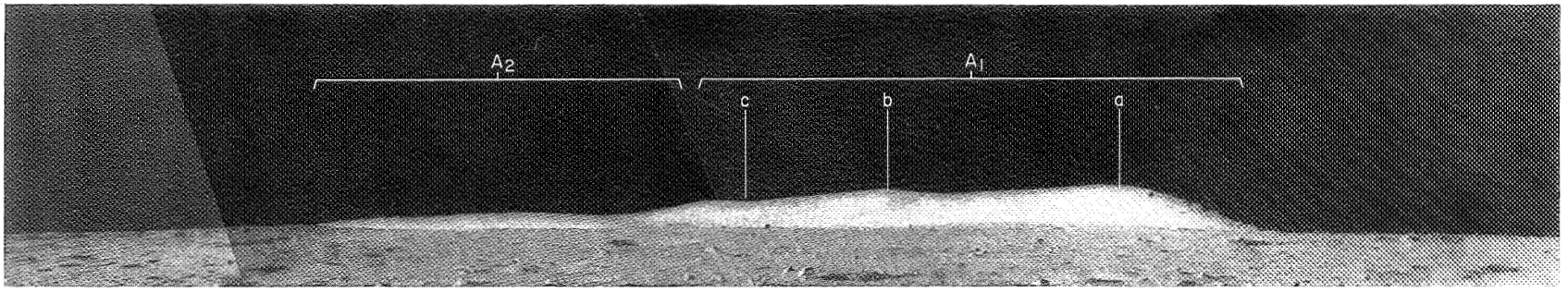

Fig. III-7. Enlargement of feature A in Fig. III-6

Table III-1. Characteristics of horizon features[a]

Feature	Width, deg	Visible height, deg	Azimuth	
			Camera, deg	Selenographic, deg
A	10.4			
A_1 (east end)			59.8	N 29.4 E
a		0.46	61.2	N 28.0 E
b		0.44	63.8	N 25.5 E
c			65.9	N 23.5 E
A_2 (east end)			66.5	N 22.9 E
(middle)		0.18	68	N 21.5 E
(west end)			70.2	N 19.3 E
B (east end)	2.1		98.1	N 7.9 W
(middle)			99.6	N 9.4 W
(west end)		0.24	100.2	N 10.6 W
C (middle)	0.4	0.06	102.7	N 12.7 W
D (middle)	1.5	0.16	105.8	N 15.1 W
E (middle)	0.48	0.04	88.0	N 2.1 E

[a]The characteristics of the features listed in the table differ slightly from the corresponding numbers published in Ref. III-3 and Ref. III-4. Additional narrow-angle pictures have helped to refine the relative camera azimuths to ±0.2°.

A comparison of the horizon features shown in the *Surveyor* pictures with the telescopic photographs of the region around Flamsteed has permitted an accurate determination of the landing site of the spacecraft (Fig. III-8). This comparison indicates that the landing site is 2.53°S and 43.32°W (referred to the lunar coordinates), close to site II mentioned in Ref. III-1, and coincident with the site computed from post-landing tracking data (2.58 ±0.16°S and 43.35 ± 0.10°W). The identification of features observed by *Surveyor* with the hills photographed by the telescope is the same as that made by Whitaker (Ref. III-2). His solution for the landing site (2.57°S and 43.34°W) was based on measurements of the hill positions given in Ref. III-2. It should be noted that the selenographic coordinate positions of telescopically observed features in this area of the moon have an uncertainty on the order of ±0.03°.

B. General Slope of Surveyor I Landing Site

The position of the horizon on the *Surveyor* panoramic pictures (particularly in the narrow-angle frames), together with the calibrated camera pointing angles, can be used to establish the local average inclination of the landing site terrain relative to the camera axis. This inclination can be determined to a fraction of a degree.

Observations of the horizon positions can be used to determine the average slope of the terrain once the camera attitude, relative to the local astronomical vertical, is known. The attitude of the camera may be found, in turn, from pictures of stars and the planet Jupiter. These pictures were obtained by operation of the camera in the open-shutter mode. Light scattered from the lunar terrain, however, produced a high background in daytime pictures of the sky; therefore, the images of only two very bright stars, Sirius and Canopus, were recorded during daytime (Table III-2). Additional stars and Jupiter were recorded in three narrow-angle pictures after sunset of the first lunar day using the integrating mode of the camera. These stars were identified as (Fig. III-9): ε Gemini (3.2 magnitude), μ Gemini (3.2 magnitude), η Gemini (3.4 magnitude, variable), and 1 Gemini (4.3 magnitude). The exposure time of each of the frames was approximately 30 sec. Additional exposure time would have yielded considerable increase in camera sensitivity, and more stars would have been detected.

Table III-2. Celestial objects observed during first lunar day

Object	Day	Time (GMT)	Number of frames
Sirius	156	12:30 to 12:44	8
Sirius	157	12:30 to 12:36	4
Canopus	157	12:37 to 12:45	12
Sirius	162	16:56 to 17:04	12
Jupiter	165	16:11	12

The attitude of the camera, in celestial coordinates, can be determined, in principle, from any group of two simultaneous celestial observations. The attitude, in celestial coordinates, can then be transformed to an attitude in selenographic coordinates, employing the solution for the selenographic position of the spacecraft. Each of the stellar pictures, however, has been obtained at a different time; it is, therefore, necessary to use the estimated selenographic position of the spacecraft in the initial solution of camera attitude.

For convenience, the transformation matrix that defines the attitude of the camera was determined from groups of three celestial observations. The solution for the transformation matrix was obtained from the vector equation

$$\mathbf{Y} = A\mathbf{X}$$

where $\mathbf{X}$ is a unit vector to the celestial object from the camera and $\mathbf{Y}$ is a unit vector to the same object in the selenographic coordinate system. The transformation

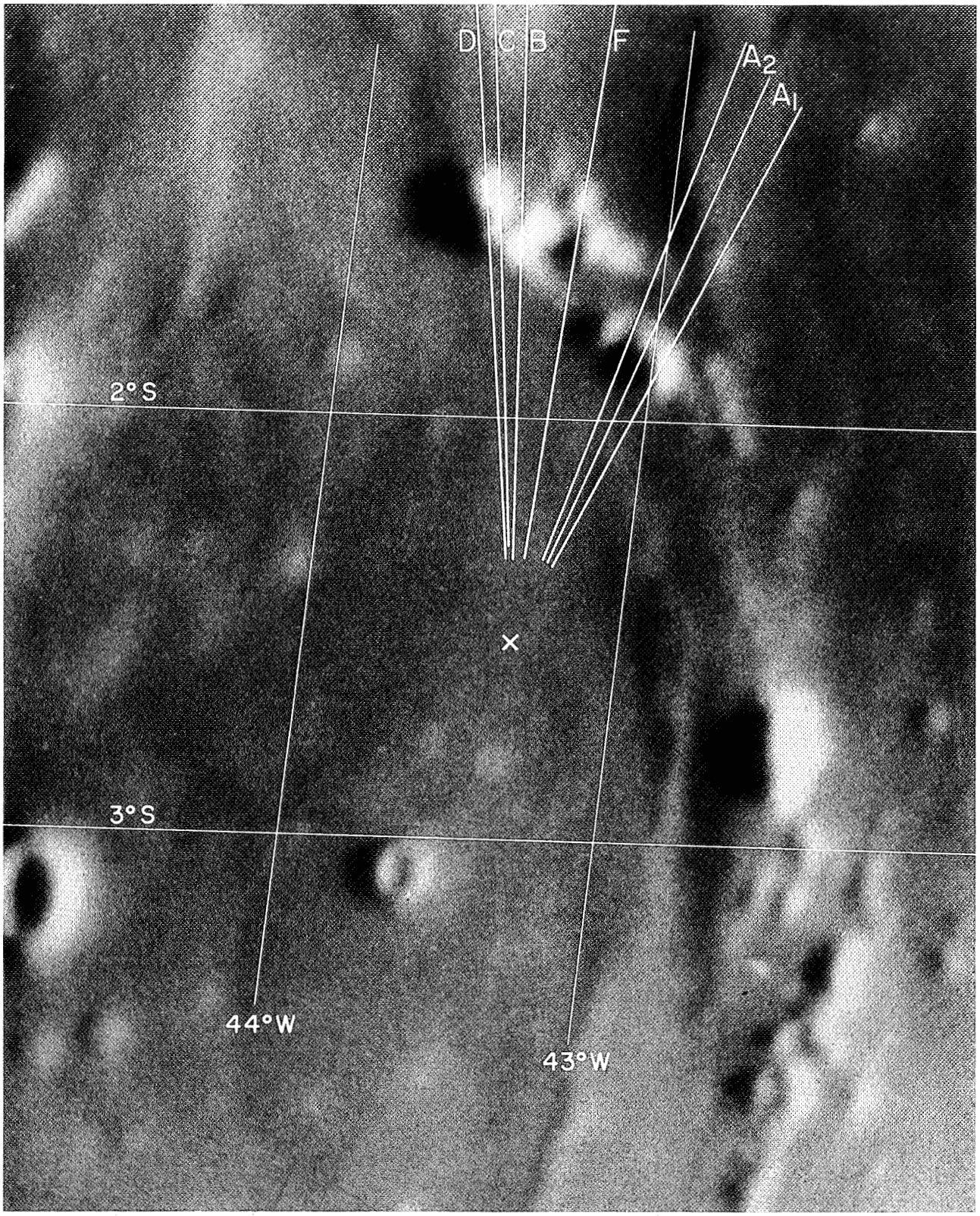

Fig. III-8. Relationship of horizon features to *Surveyor* landing site (lunar photograph by courtesy of E. A. Whitaker of the Lunar and Planetary Laboratory, University of Arizona)

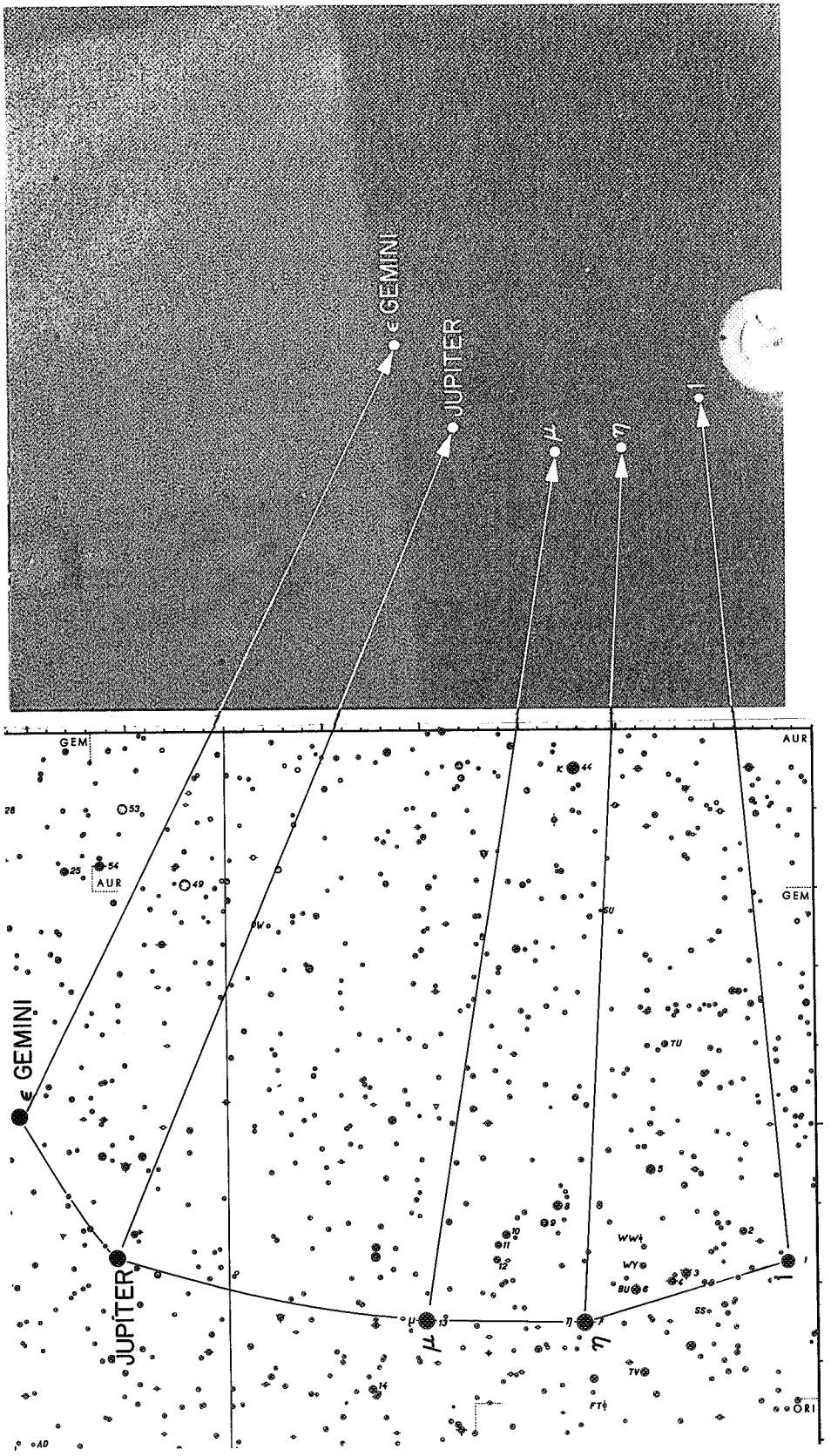

Fig. III-9. Jupiter and constellation Gemini taken on June 14, 1966, 16:14:22 GMT. (Additional marks on photograph are the reseau dots and vidicon surface blemishes.)

matrix, which is a rotational matrix between rectilinear coordinate systems, is orthonormal. In actuality, the camera introduces pointing errors that require an application of the Gram–Schmidt construction for orthonormalizing a matrix. These errors are an order of magnitude larger than the uncertainty in the selenographic position of the spacecraft. The pointing errors are due primarily to uncertainties in the alignment of the optical axis with the reseau and to positional inaccuracies of the mirror.

The sub-celestial object points on the lunar surface were computed using a Jet Propulsion Laboratory computer program (Ref. III-5), followed by a simple rotation to the selenographic coordinates of the landing site. This resulted in a determination of each celestial object's altitude and azimuth at the landing site. The transformation or attitude matrix can be broken down into the zenith angle of the camera's axis and the azimuth of inclination. These angles, computed from five observations and averaged over the resultant matrices, resulted in a zenith angle of 15.1 $\pm 0.5°$ at an azimuth of 37.1 $\pm 0.4°$ from lunar north.

The nominal camera orientation with reference to spacecraft coordinates is 16° tilt from the Z axis at 55° counterclockwise from the $-Y$ axis. The azimuth from lunar north of the $-Y$ spacecraft axis (assuming the nominal orientation of the camera) is 89.6 $\pm 0.4°$. If the assumption is made that the orientation of the camera after landing is still nominal, then the Z axis of the spacecraft has a zenith angle of 0.9° at an azimuth of 220° from lunar north. This attitude is in general agreement with that determined from solutions of the orientation of the solar panel–planar array and with the positions of the attitude gyro on the spacecraft before and after touchdown.

Using this attitude determination, the *Surveyor I* landing site is observed to be smooth on a kilometer scale, consistent with location in a maria area. The elevation of the horizon, as seen in the pictures, usually varies $<0.5°$ within any 45° azimuth sector. The absolute horizon position indicates a possible slight slope ($<3°$) of the terrain from northeast down toward southwest.

C. Morphology and Structure of Terrain Around Spacecraft

The terrain within 1 to 2 km surrounding the landing site, as observed from the *Surveyor* pictures, is a gently rolling surface studded with craters ranging in diameter from a few centimeters to several hundred meters. Several craters that probably range in size from a little less than 100 m to perhaps as much as 0.5 km have been recognized along the horizon. Their true diameters cannot be accurately estimated. They range in angular width from about 15 to 36°. One of these craters, which lies slightly south of east of the spacecraft, has a prominent raised rim about 5 m high (Fig. III-10). The exterior slopes of this crater rim exhibit a maximum inclination to the horizon of about 11.5°. The visible rim crest and exterior slopes of the rim are strewn with coarse blocky debris. Two larger, but more distant, craters southeast of the spacecraft have relatively low, inconspicuous rims, although patches of coarse blocks can be seen close to the horizon on the rim of one of these craters.

Several dozen craters, which range in diameter from about 3 to 100 m, have been recognized in the field of view below the horizon. One of the most prominent of these craters (Fig. III-11) lies about 11 m from the spacecraft; it is about 3 m wide and approximately ⅔ m in depth. It has a distinct raised rim and an inner wall, pocked by small craters, which slopes somewhat less than 28°. Most of the other craters in the size range of 3 to 20 m have low, rounded, inconspicuous rims or are rimless. The larger craters taken together resemble, in distribution and form, the craters of equivalent size observed in the *Ranger* pictures in Mare Cognitum and Mare Tranquillitatis.

The smaller craters, ranging in diameter from a few centimeters to 3 m, are generally shallow and difficult to observe under high solar illumination, but are conspicuous at low illumination angles. Most of them either have low, rounded rims or are apparently rimless. Where the small craters can be observed, close to the spacecraft, they are relatively closely spaced and cover over 50% of the surface.

D. Size Distribution of Small Craters

Two sample areas were selected near the spacecraft for a preliminary investigation of the size–frequency distribution of craters in the size range of a few centimeters to 4 m. The sample areas (area A, 6 m^2; area B, 47 m^2) lie approximately 4 and 7 m mean distance from the spacecraft (areas A and B, Fig. III-12). Wide-angle pictures, taken at low sun elevations (approximately 8° and 20°), were used to identify the craters (Figs. III-13 to III-17). A total of 616 craters were counted; less than 10 of them in the size range of 10 cm to 4 m had recognizable raised rims.

The integral frequency distribution of the craters, normalized to 100 m^2 for each sample area, is shown in Fig. III-18. The two sample areas overlap in resolution.

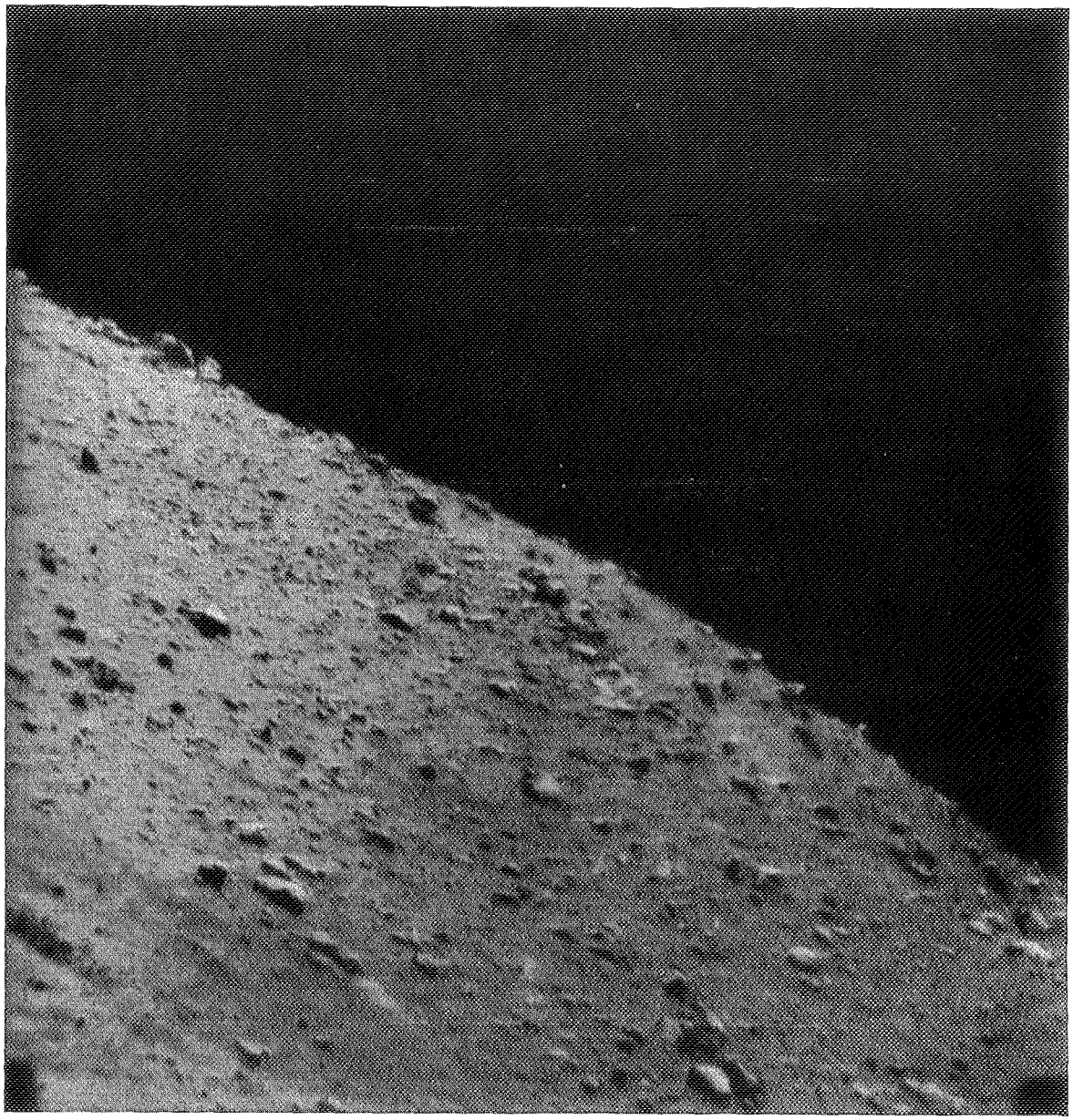

Fig. III-10. Large crater, southeast of spacecraft. [This crater is shown at a different sun elevation in Fig. III-24(g).]

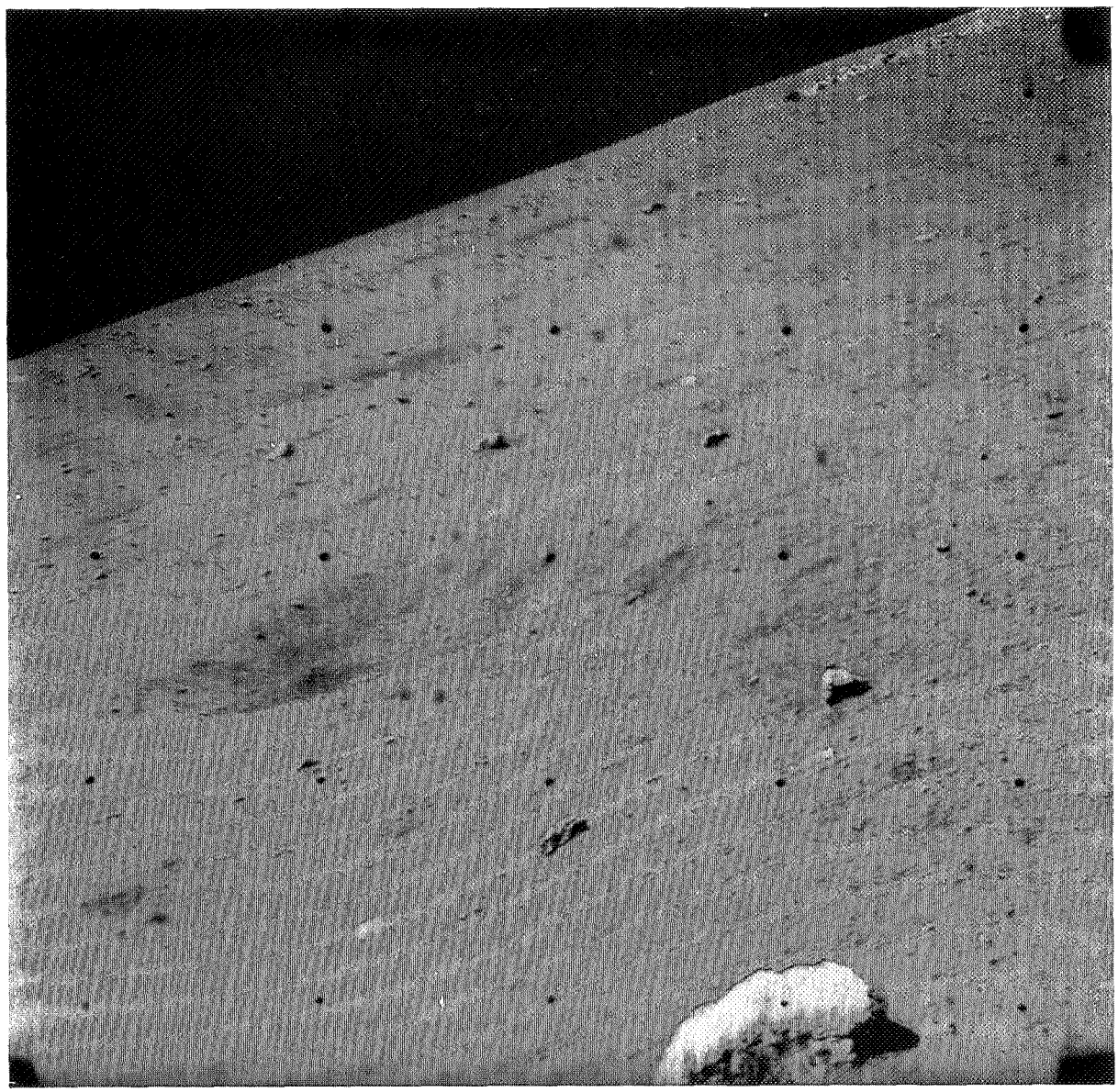

Fig. III-11. Crater approximately 3 m in diameter, southeast of spacecraft

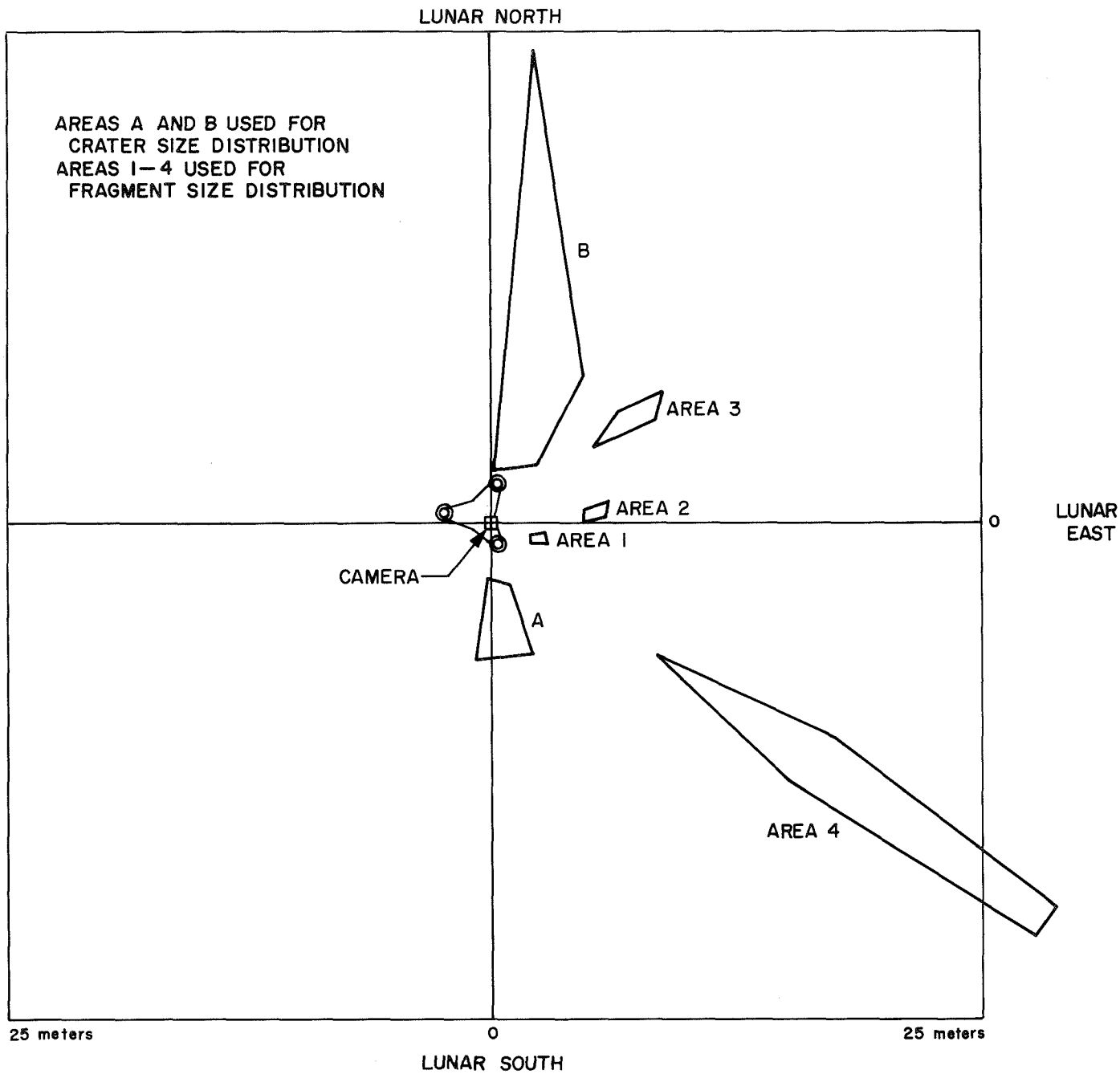

Fig. III-12. Location of areas used in determination of size–frequency distribution of craters and fragments that comprise lunar surface

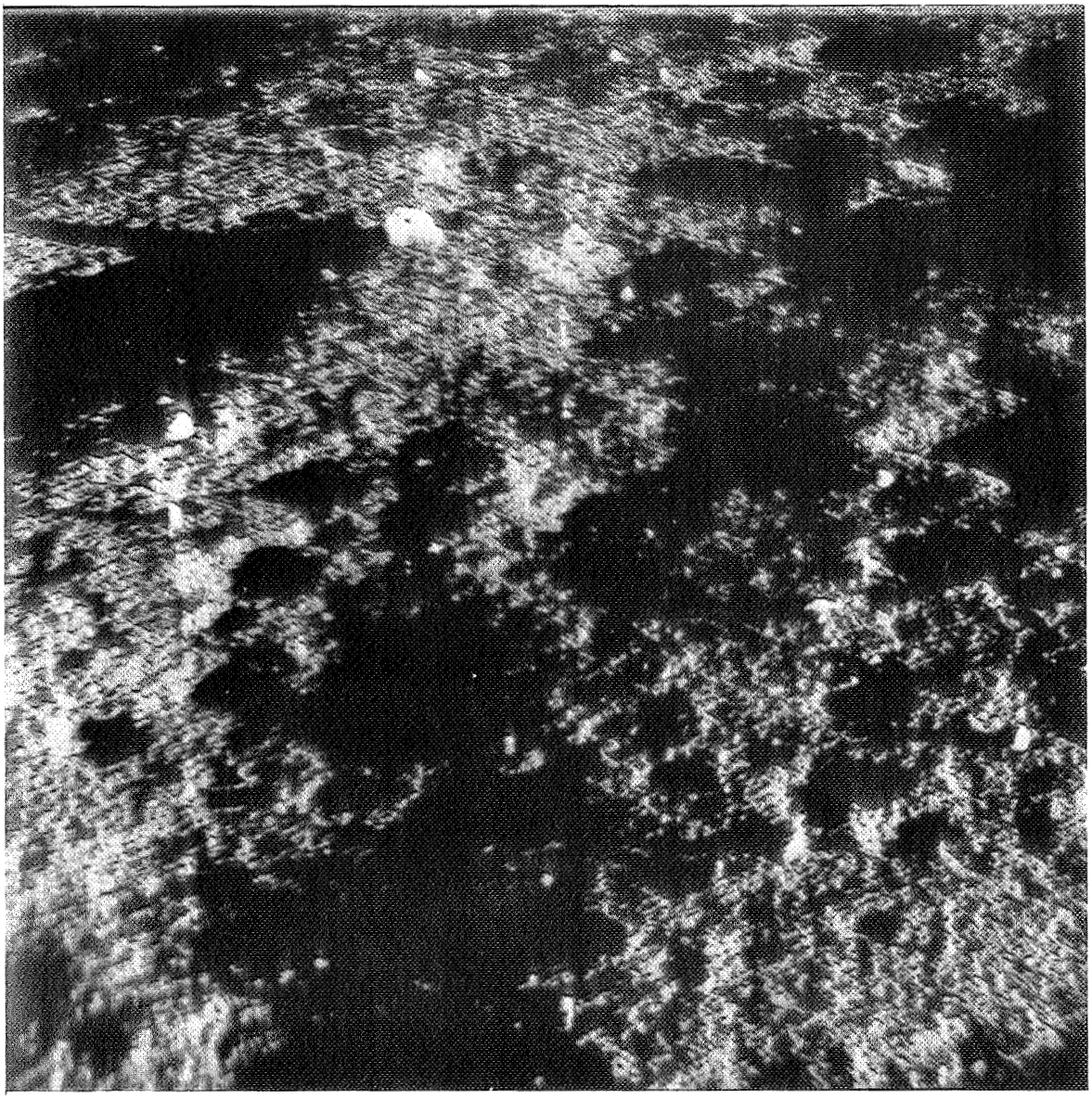

Fig. III-13. Area A: sun elevation of approximately 8°

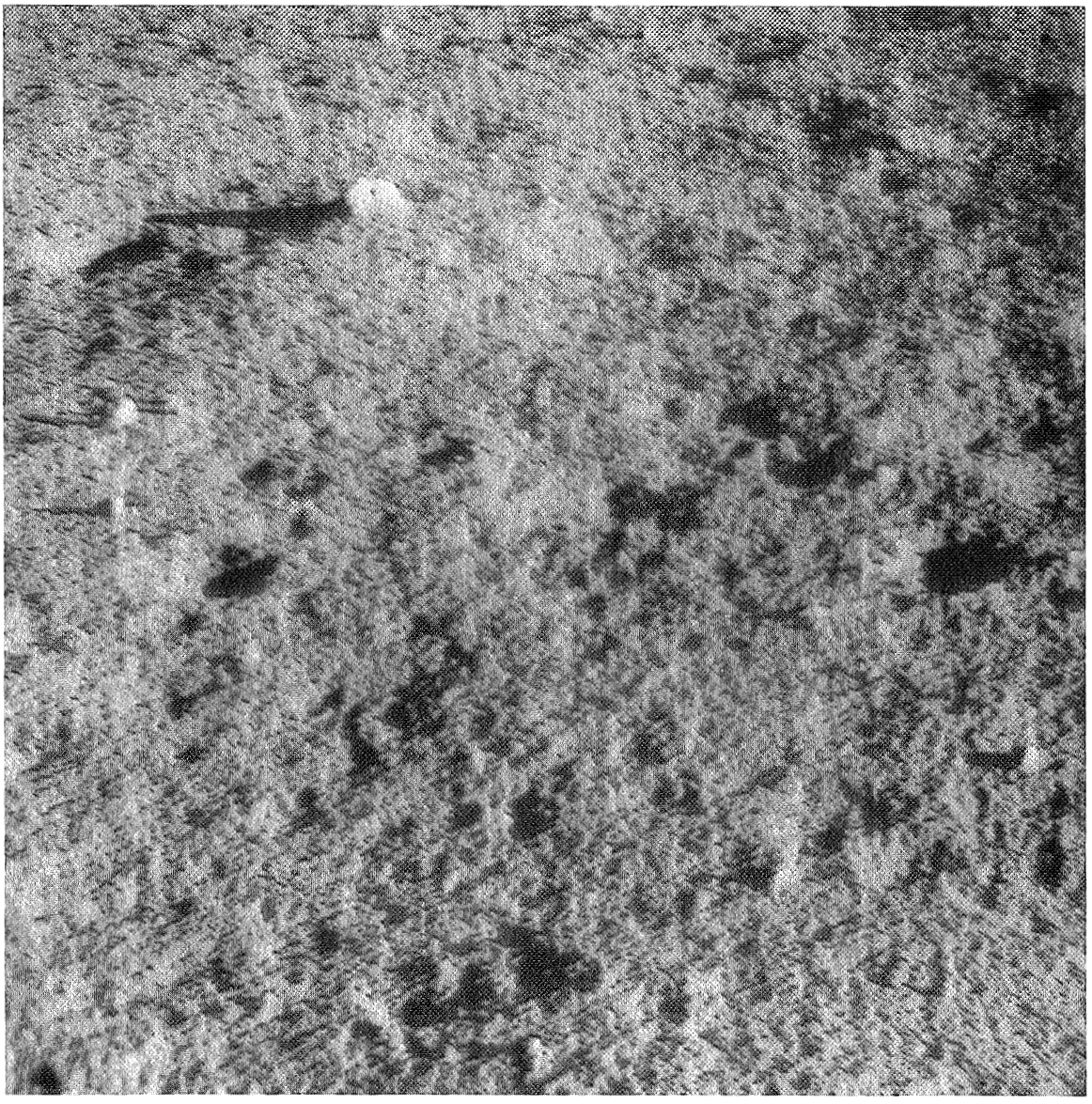

Fig. III-14. Area A: sun elevation of approximately 20°

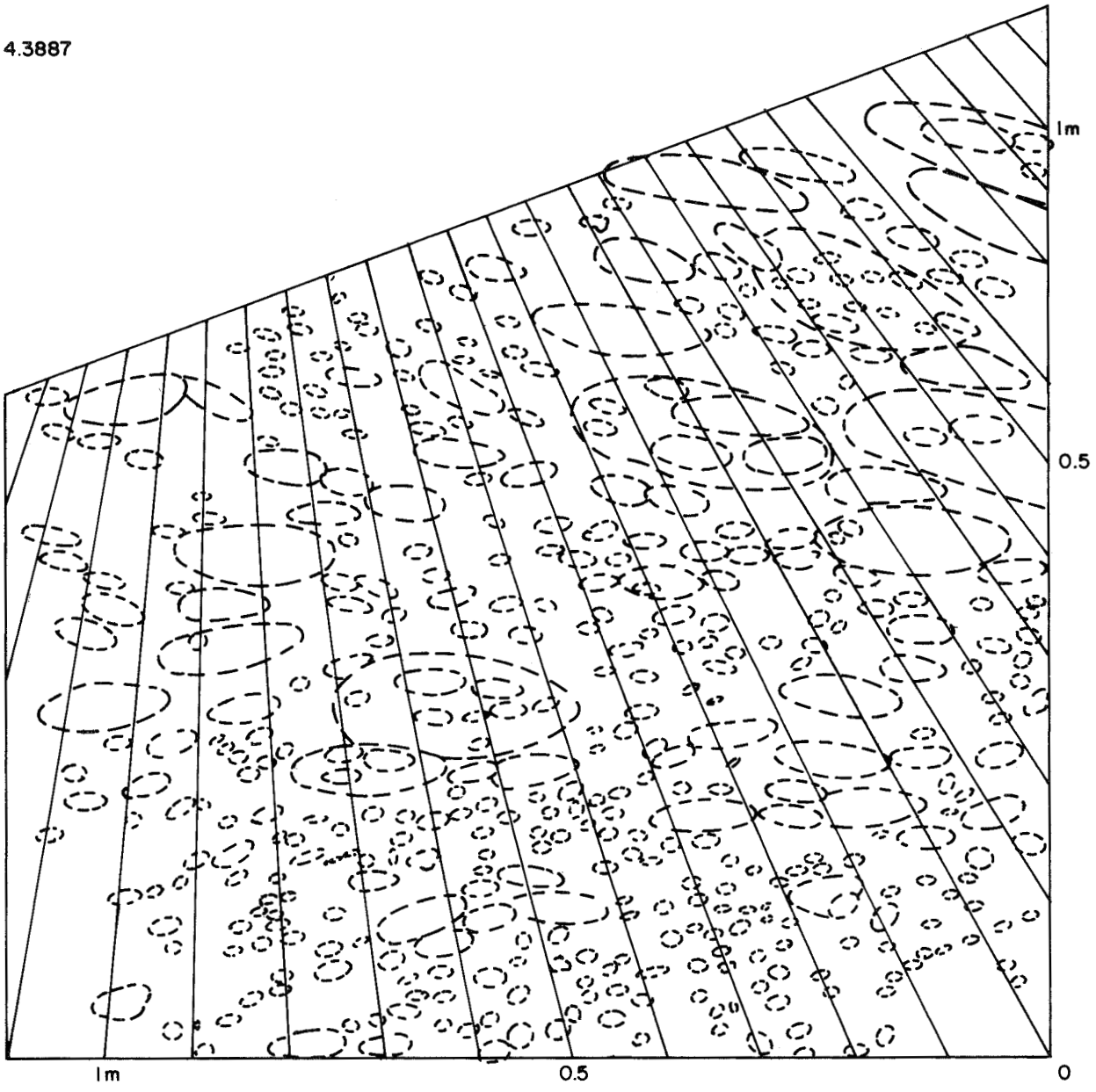

Fig. III-15. Sketch map of craters measured in area A

Fig. III-16. Area B: sun elevation of approximately 20°

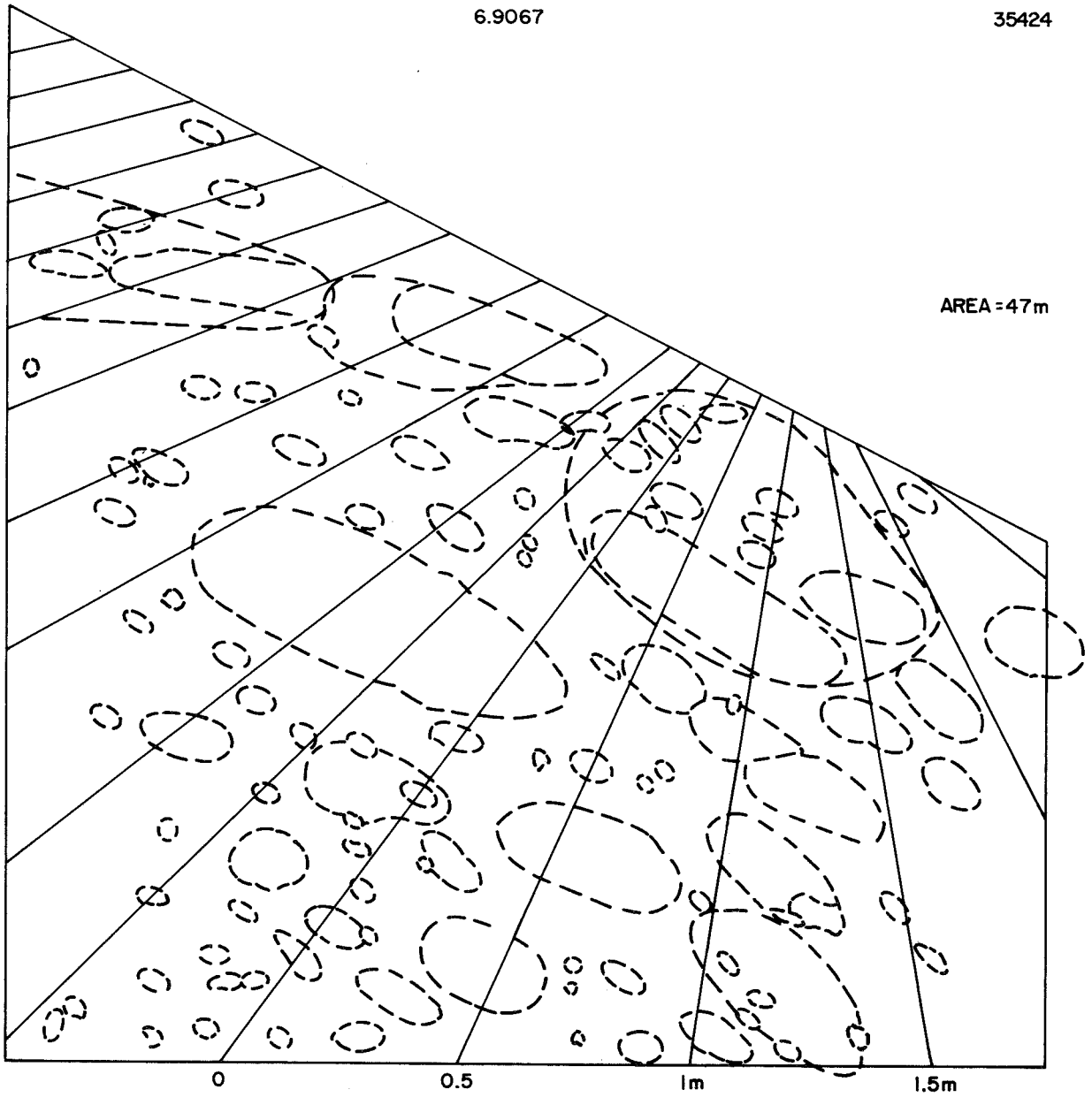

Fig. III-17. Sketch map of craters measured in area B

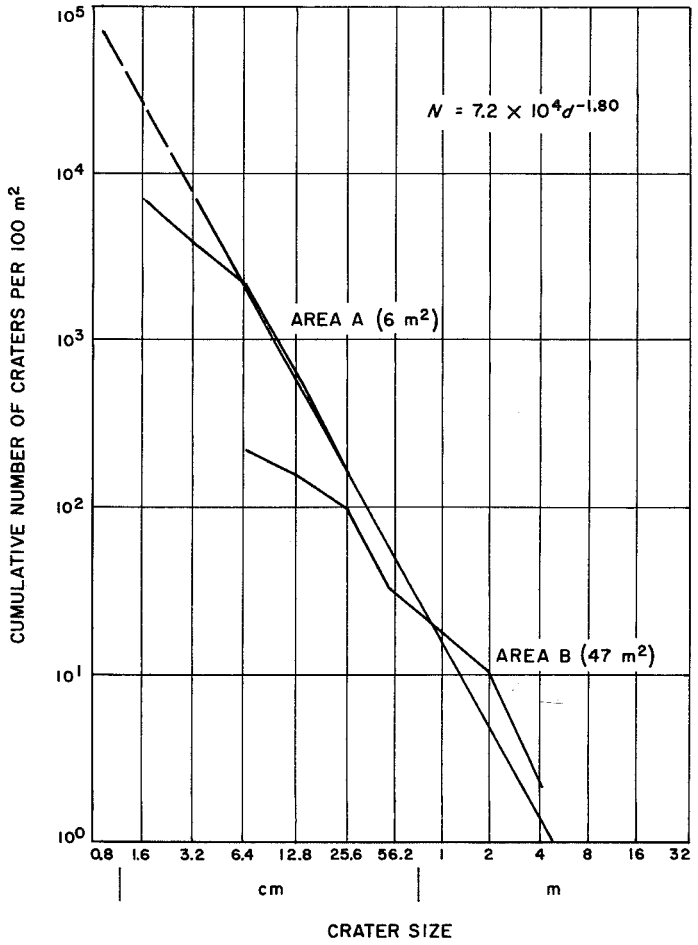

Fig. III-18. Cumulative size–frequency distribution of craters on lunar surface determined from *Surveyor I* pictures

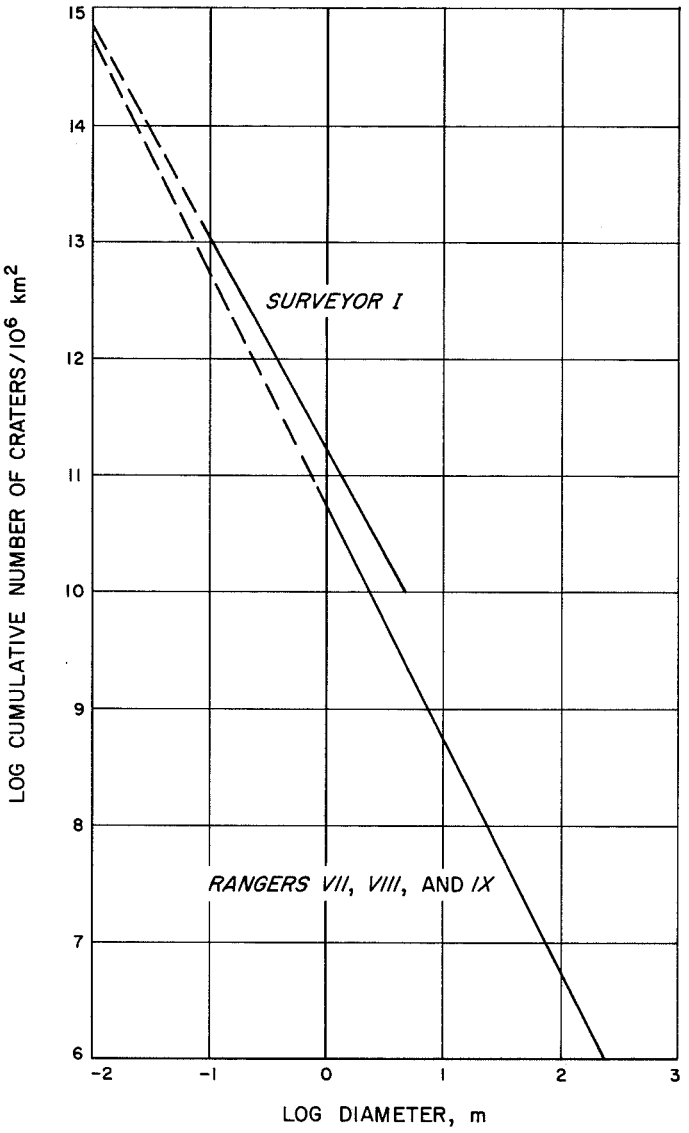

Fig. III-19. Cumulative size–frequency distribution of craters on lunar surface determined from *Surveyor I* pictures and from *Ranger VII–IX* pictures

The scale of the pictures changes rapidly from the near field to the far field. Smaller craters, of a size easily recognized close in to the spacecraft, cannot be resolved in the distant parts of the sample areas; therefore, the small craters counted are too few in proportion to the number of large craters. The estimated general size–frequency distribution of the craters is shown by the solid line in Fig. III-18, in which account has been taken of the error in the number of small craters. This line is the plot of the following equation:

$$N = 7.2 \times 10^4 \, d^{-1.80}$$

where N is the cumulative number of craters and d is the diameter of craters in centimeters. The curve is bounded at an upper limit of crater diameters of approximately 5 m. One crater, approximately 5 m in diameter, would be expected in each 100-m surface area.

Figure III-19 shows the comparison of the cumulative size–frequency distribution determined for the surface around *Surveyor I* with the cumulative size–frequency distribution of craters observed by *Rangers VII* through *IX* (Ref. III-6). In the crater size range of 1 to 5 m, more craters have been observed per unit area in the *Surveyor* pictures than in the *Ranger* pictures. This may be due chiefly to greater ease of recognition of craters of this size in *Surveyor* pictures as compared with *Ranger* pictures.

E. Distribution of Blocks and Coarser Debris

The lunar surface in the vicinity of the spacecraft is littered with coarse blocks and fragments. Most of the more prominent blocks in the field of view appear to

have a nearly random distribution over the surface; however, significant concentrations of blocks and finer rubble occur in certain locations. A strewn field of very coarse, relatively closely spaced blocks surrounds the crater noted on the eastern horizon (Fig. III-10). This field extends from the rim crest of the crater out to a distance of about 1 crater diameter in each direction along the horizon. It is highly probable that the large majority of these blocks is a part of a more or less continuous blanket of ejected debris surrounding the crater and that most of these blocks have been derived from within the crater.

A fairly large number of the blocks observed on the horizon, formed by the crest of the crater rim, have angular widths as great as 15 min of arc. The rim of the crater is about 300 m from the spacecraft, and these blocks must all be more than 1 m across. Other blocks, associated with a still more distant crater rim, are also probably more than 1 m across; some have angular widths of more than 20 min of arc.

Patches of rubble are scattered in the foreground and middle distance; these patches have an average grain size much less than that of the nearby coarser blocks, but significantly greater than the average resolvable grain size of nearby parts of the surface. These patches resemble flattened piles of rubble derived from the slow-speed impact of weakly coherent material thrown out of experimental craters produced by explosion and impact on earth. Some of the patches around *Surveyor I* occur within shallow depressions, which may be secondary-impact craters.

Most of the coarser blocks scattered about the surface appear to be similar in shape and are angular to subangular; some are sub-rounded. The majority of the angular blocks appear to rest on the surface, with perhaps 80 to 90% of their bulk above the surface level, whereas many of the round blocks seem to be partially buried; in some cases, perhaps 50% or more of the block is below the surface level. None of the fragments or blocks are seen to rest on pedestals, as suggested by Lebedinskiy (Ref. III-7) on the basis of *Luna 9* pictures.

The angular blocks, especially those on the rim of the prominent crater on the eastern horizon, are typically faceted as through broken along joints or pre-existing fractures. Some of the large blocks along the horizon appear to be resting on top of the surface and have demonstrable overhangs (Fig. III-10). These blocks must have substantial cohesion and shear strength, particularly if they have arrived in their present position by ejection from the crater. The very large majority of the coarse blocks have, in addition, a demonstrably higher albedo than most of the rest of the lunar surface in the field of view. This is particularly noticeable under high sun, when the blocks stand out prominently as bright spots. These data suggest that the blocks are composed of material somewhat different physically from the general finer-grained matrix of the lunar surface and that most of them consist of relatively strong single pieces of rock.

Two blocks relatively close to the spacecraft are of special interest. One of these blocks (Fig. III-20) is about 0.5 m across and lies some 5 m southeast; the other (Fig. III-21) is slightly more than 0.5 m across and lies about 5 m southwest of the camera. The rock to the southeast is distinctly rounded on its upper side, although it is faceted in places and has overhangs on the side facing the camera. The narrow-angle frames show that the block is distinctly marked with close-spaced dark spots a few millimeters across. Most of the spots are clearly shadows within pores or cavities in the rock surface. They are so close in size to the resolution limit of the pictures that the character of the cavities cannot be determined with confidence. They may be intergranular pore spaces in a relatively coarse-grained rock, or they may be vesicles. The spots exhibit a distinct elongation and pattern, however, which resembles that produced by flowage and distortion of vesicles in a volcanic rock. It seems probable that the block observed is a rock congealed from a gaseous melt. Such a melt could have been produced either by strong shock or by vulcanism, and the rock could be an impactite, a volcanic bomb, or a fragment from the top of a vesicular lava flow.

The second block close to the spacecraft is quite different from the first. It is angular in shape, with well developed facets that are slightly rounded at the corners and at the edges. This block appears to be devoid of resolvable granularity, but it is distinctly mottled. The lighter parts of the block tend to stand out as small knobs. The block has the appearance of being somewhat eroded, and the brighter knobs may stand out as a result of differential erosion. One of the most striking things about this block is a very pronounced set of fractures that appear to intersect; these fractures resemble the cleavage planes produced during plastic flow of rock under moderately high shock pressure. Another striking feature is that the block lies in a swarm of somewhat similar smaller fragments that are strewn out in the direction of the main block. At least 50 separate pieces are

Fig. III-20. Rock approximately 0.5 m long, southeast of spacecraft. (Dark spots are pores or cavities.)

present in the swarm. Many of these fragments and part of the base of the block appear to be partially buried in the lunar surface; a few fragments seem to rest on the surface. The impression gained is that the main piece has broken, perhaps on impact with the surface, and that it may have relatively low shear strength; no impact or skid marks are observable around the block or pieces. The swarm of fragments may have been lying on the surface for a considerable period of time and have been partially buried by younger, finer debris.

F. Size Distribution of Debris on Lunar Surface and Characteristics of Fine Matrix

The spacecraft appears to be located in a relatively representative part of the terrain in the field of view, and a first attempt has been made to evaluate the size–frequency distribution of fragments making up the observable lunar surface from a series of narrow-angle pictures of small areas relatively near the spacecraft. The pictures used were taken under comparatively high sun; therefore, only the more prominent grains were counted. It is expected that these first estimates of the size–frequency distribution will be slightly biased toward underestimating the actual average grain size.

Four sample areas (Fig. III-22), 0.23, 0.90, 3.5, and 50 m^2 in size, were selected on the undisturbed surface, ranging in mean distance from 2.5 to about 20 m from the camera (Fig. III-12). The areas and grain sizes were estimated by transformation of the pictures to a nominal flat surface defined as being at a base of the spacecraft footpads. All sharply formed fragments and grains that are easily recognizable in the pictures were measured and counted; these amounted to a total of 825, and ranged in diameter from 1 mm to more than 1 m.

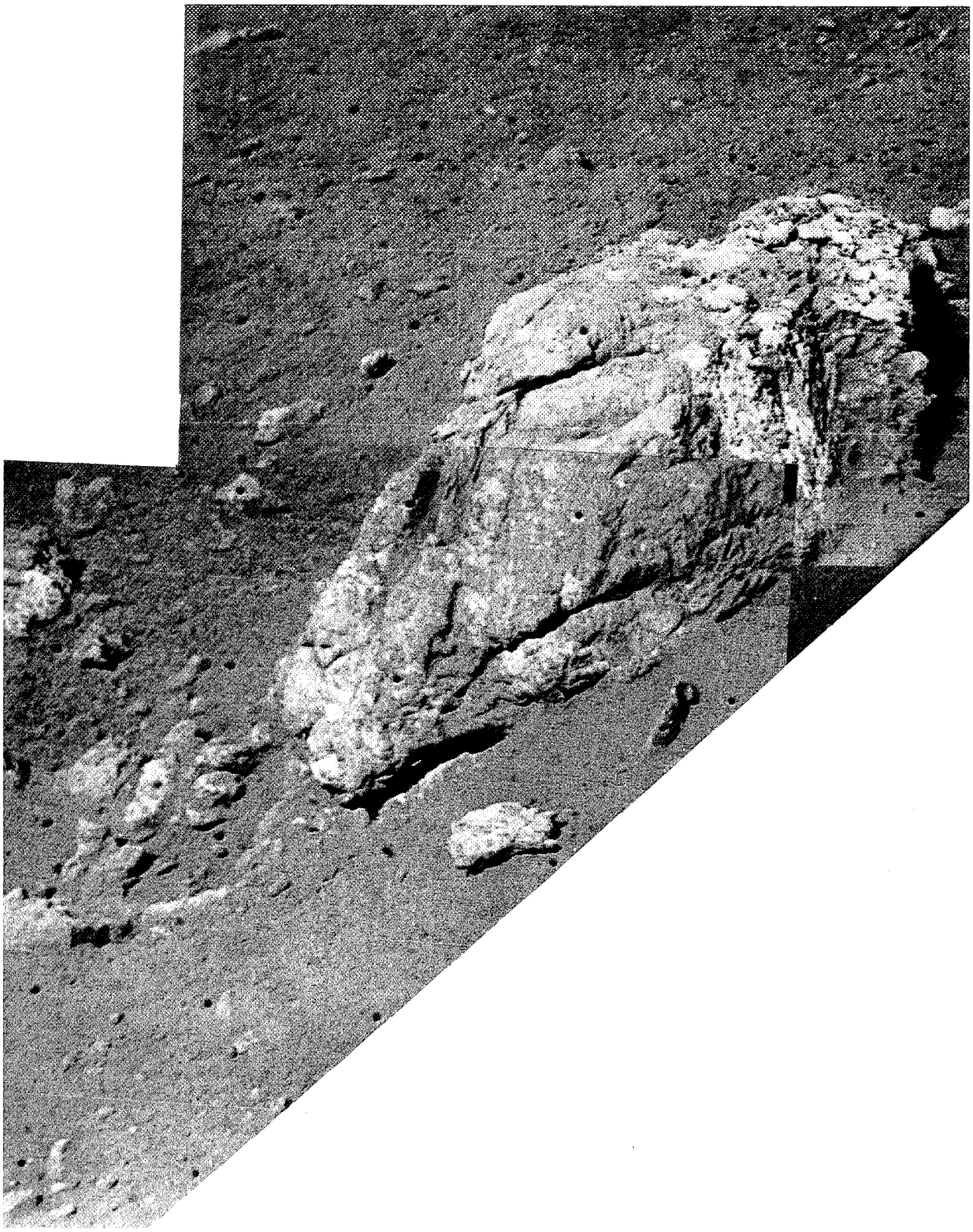

Fig. III-21. Block with rounded edges and associated fragments, southwest of spacecraft.(Note mottling and fractures on main block.)

Fig. III-22. Sample areas

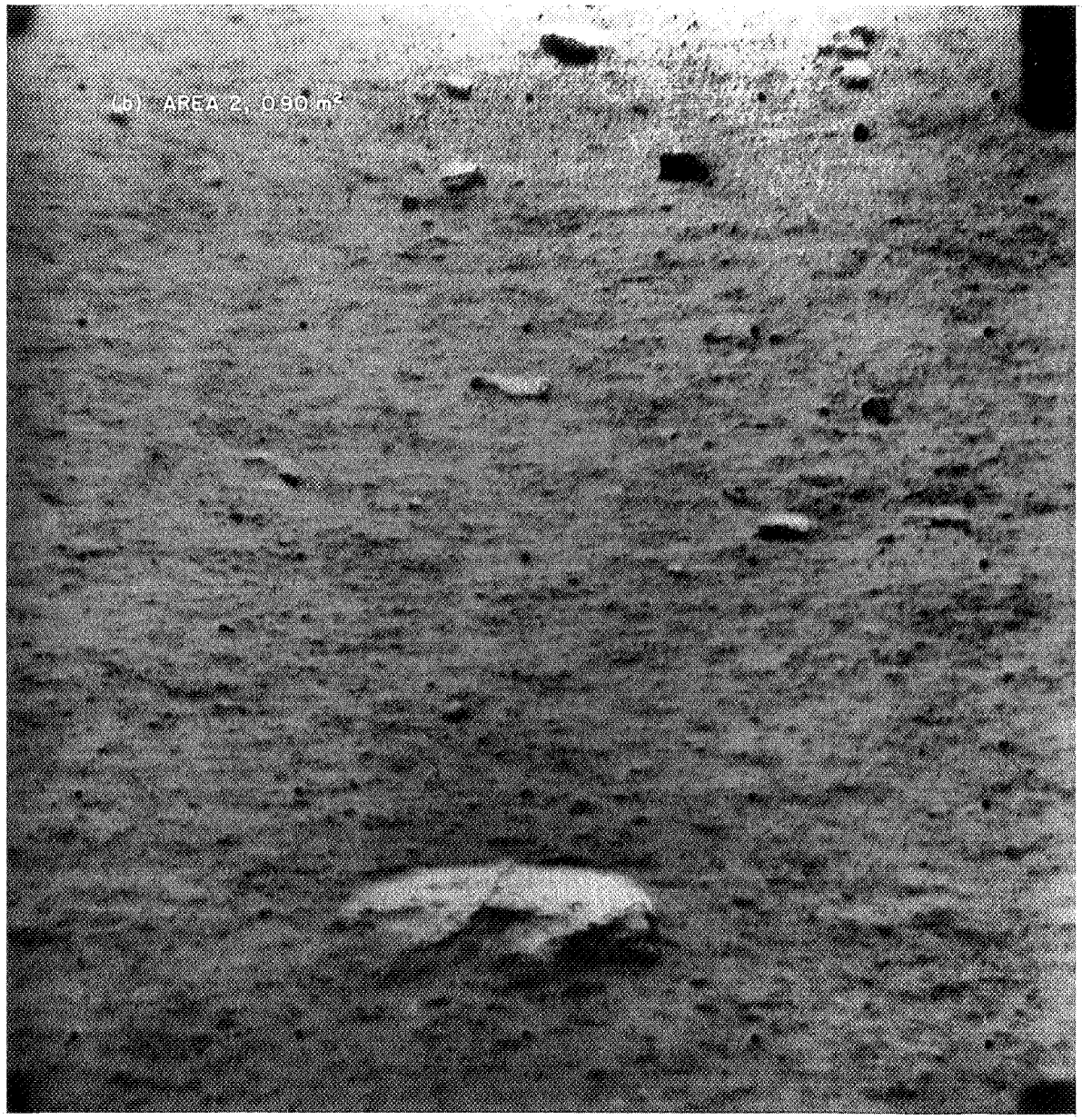

Fig. III-22. Sample areas (cont'd)

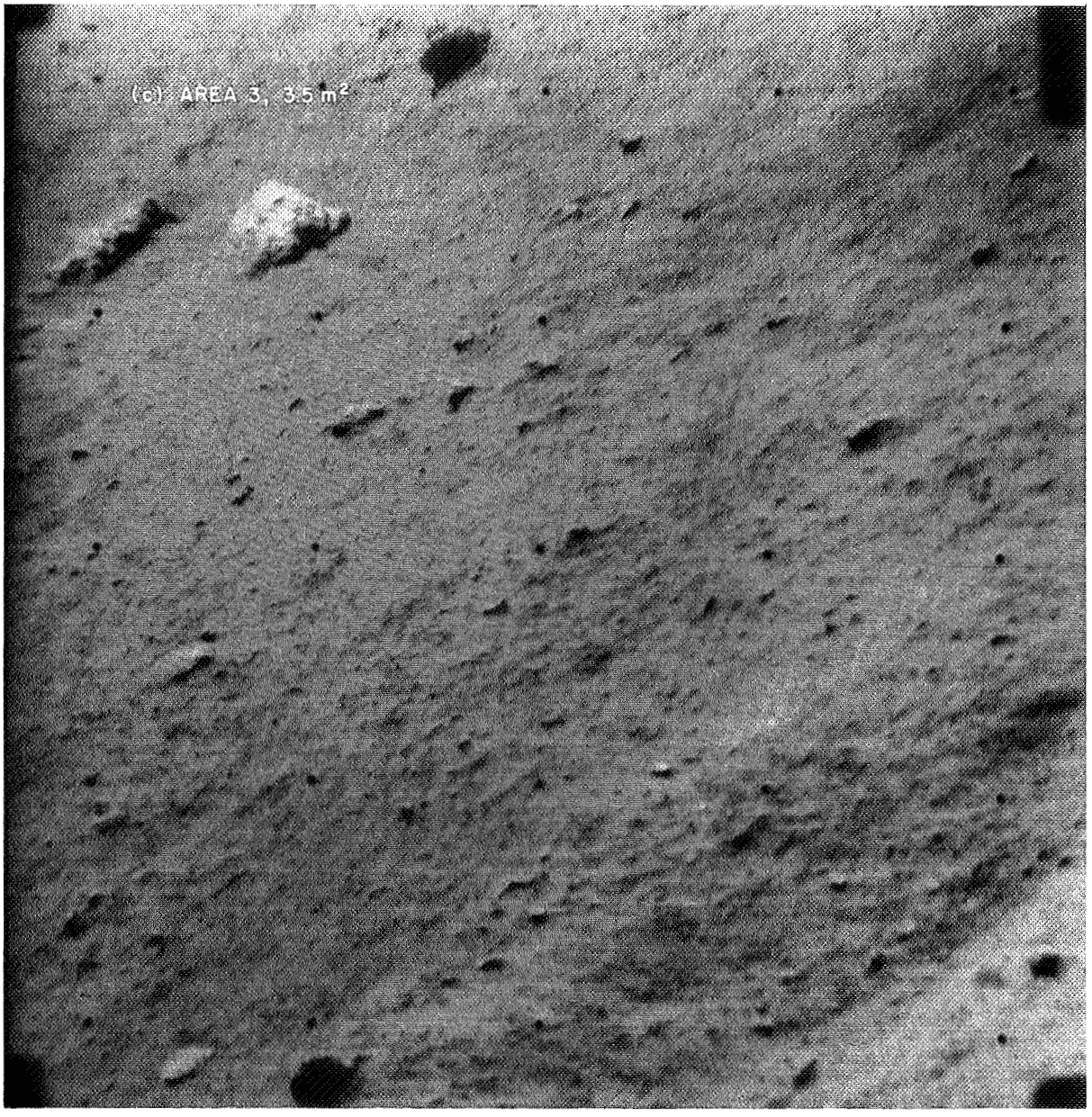

Fig. III-22. Sample areas (cont'd)

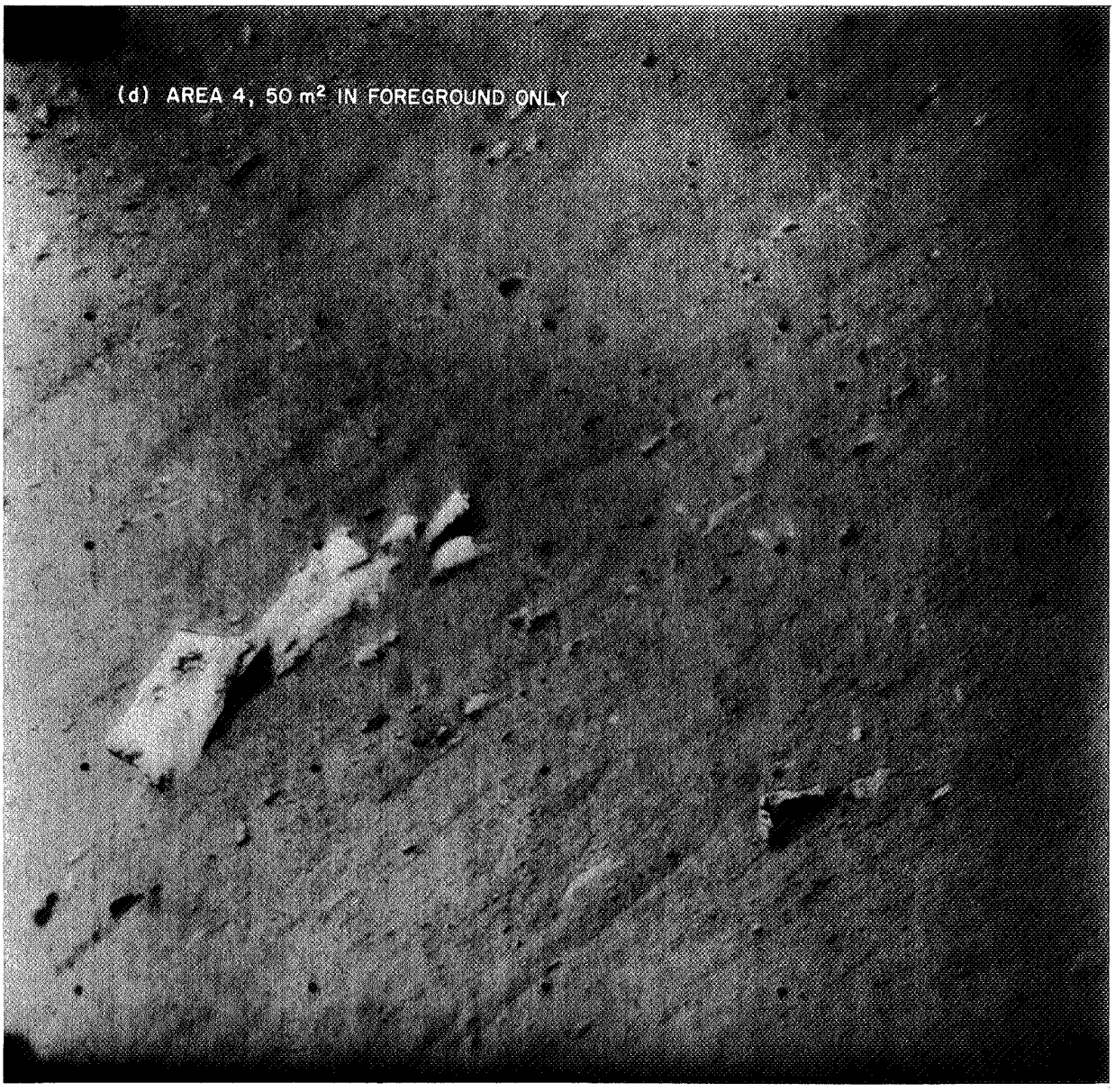

Fig. III-22. Sample areas (cont'd)

The integral size–frequency distribution of the grains, normalized to an area of 100 m², for each of the sample areas is shown in Fig. III-23. It can be seen from this figure that the sample areas selected provide overlapping coverage in resolution and that the size–distribution functions of the grains in each area may be roughly described as segments of one overall distribution function. There is clearly some heterogeneity from one small area to another, as would be expected from examination of the lunar surface within the field of view; however, the general size–frequency distribution of fragments on the local lunar surface is probably fairly well estimated by the lower solid line in the figure. This line is the plot of the following equation

$$N = 3 \times 10^5 y^{-1.77}$$

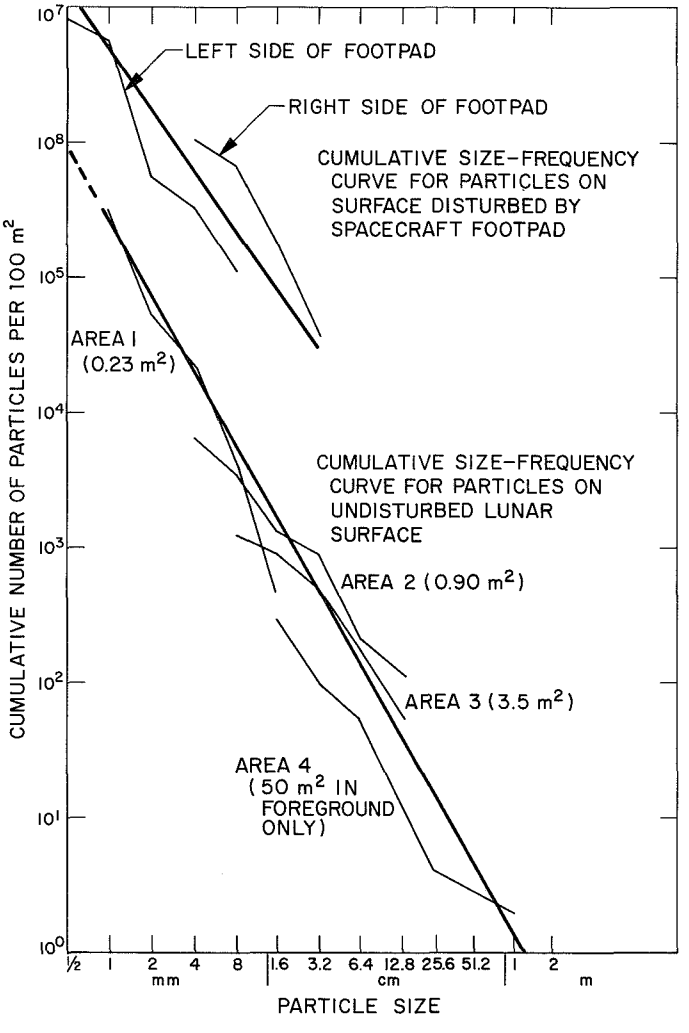

Fig. III-23. Cumulative frequency distribution of particles on lunar surface, as determined from Surveyor I pictures

where N is the cumulative number of grains and y is the diameter of grains in millimeters. This function is bounded at an upper size limit of about 1 to 2 m, but probably extends to particle sizes considerably below the limit of the observational data (1 mm). About one block, 1 m across, is expected to be found on each 100 m² of the surface. The observed angular fragments occupy 7.6% of the surface area and have a volumetric median grain size of 130 mm. The volumetric median grain size of all fragmental material on the surface is probably 1 mm or less. The form and constants of this size-distribution function are closely similar to the size–frequency distribution of fragments produced by crushing and grinding of rocks in ball mills and by repetitive impact of rock surfaces.

The matrix of the unresolved material between the grains, where observed very close to the spacecraft, shows a peculiar patchiness of albedo when observed under high sun. These patches may be caused by successive thin deposits of very fine-grained material derived from different areas.

G. Cohesion and Thickness of Surficial Fragmental Layer

The shapes and grain size of ejecta from small impact craters are closely related to the cohesion of the target material (Refs. III-8 and III-9). Many craters, up to 1 m across, with relatively smooth raised rims are scattered about in the near field around the spacecraft. Craters such as these can be produced experimentally by impact only in a relatively fine-grained fragmental medium with very low cohesion (less than 10^4 or 10^5 dynes/cm²). Impact craters formed in more cohesive matter or in very coarse-grained material tend to have irregular rims with pronounced lumps or blocks. Such craters also generally exhibit local slopes on their inner walls much steeper than the angle of repose—a feature that has not been observed in the small craters around *Surveyor I*.

The thickness of the fragmental layer in the area around the spacecraft can be estimated from the depth of the smallest craters that exhibit rims of coarse, blocky material. A survey of craters with raised rims (Table III-3) shows that craters up to about 3.3 m in diameter have smooth rims, and larger craters of this type have blocky rims [Figs. III-24 (a) through (g)]. All of the craters listed in Table III-3 have well developed raised rims except crater 6, which appears to be near the lower limit of the size range for blocky rimmed craters. Depth can be estimated directly only for a few of the craters listed;

it is therefore, necessary to assume some probable original depth-to-diameter ratio in order to estimate the depth of the craters with blocky rims. This ratio is typically between one-fourth and one-third for fresh impact craters in the size range of a few meters to a few tens of meters. If this range of depth-to-diameter ratio is assumed for the possible original shapes of the blocky rimmed craters, the indicated depth of the relatively fine grained and loose surficial fragmental layer is approximately 1 m.

Table III-3. Characteristics of craters with raised rims as a function of crater diameter

Crater	Azimuth of center of crater (camera coordinates), deg	Estimated diameter, m	Rim characteristics
1 [Fig. III-24(a)]	+38	0.7	Smooth
2 [Fig. III-24(b)]	+26	1.3	Smooth
3 [Fig. III-24(b)]	+36	1.7	Smooth
4 [Fig. III-24(c)]	+74	2.0	Smooth
5 [Fig. III-24(d)]	−49	3.3	Smooth
6 [Fig. III-24(e)]	+46	3.4	Partially blocky
7 [Fig. III-24(f)]	−109	6.3	Blocky
8 [Fig. III-24(g)]	−26	80	Blocky

The surficial fragmental layer can be expected to vary erratically in thickness from place to place over the area in the field of view of *Surveyor I* (Ref. III-10). Because very few craters have been observed that provide a means of estimating the thickness, the derived figure of 1 m should be taken as a very rough estimate for the average thickness. Material with a grain-sized distribution much like that observed directly at the surface may extend to this depth.

Beneath the surficial fragmental layer, the material of the shallow lunar sub-surface must be either significantly more cohesive or composed of very much coarser grained fragments. The angular shapes of the ejected blocks suggest that the shallow sub-surface is relatively strong rock.

H. Material Ejected by Impact of Spacecraft Footpads

Around footpads 2 and 3 are ray-like deposits of ejected material extending as far as several tens of centimeters from the edge of each footpad (Fig. III-25). These deposits form a distinct raised ridge near each of the footpads. The ejected material differs both in albedo and in texture from the material exposed on the adjacent undisturbed parts of the lunar surface. The average albedo of the ejected material is nearly 30% lower than that at the undisturbed surface, as estimated by the methods described in the following paragraphs. The material is composed of distinctly coarser lumps or fragments of ejecta than the adjacent undisturbed surface material.

The integral size–frequency distribution of the lumps of the spacecraft footpad ejecta was estimated from two sample areas of about 100 and 50 cm^2, respectively, on either side of footpad 2. An estimated total of 250 grains and lumps were counted. The observed size–frequency distributions are shown in Fig. III-23; it can be seen that the footpad ejecta are about an order of magnitude coarser than the material of the surrounding lunar surface. These data strongly suggest that the observed lumps in the freshly ejected material are probably aggregates of much finer grains. The size distribution of the finer grains composing the aggregates may be given by the mean size-distribution function for the general surrounding surface. In all likelihood, the lumps are only weakly consolidated and could be disaggregated into their constituent grains under a modest pressure or agitation. Similar lumps that may be formed around natural impact craters are probably quickly broken down by the ballistic rain of small particles on the lunar surface.

I. Photometry and Colorimetry

One of the important functions of the *Surveyor* TV camera is its use as a photometer. For the first time, the observable photometric function of part of the lunar surface can now be compared with the macroscopic texture of the surface. Furthermore, a more complete measure of the function can be obtained at one lunar location than from earth-based observation, and it will be possible to test in detail the assumed symmetry or degeneracy of the photometric function.

Because the location of the landing site was near the lunar equator, measurements of the surface luminance could be made over a wide range of illumination angles in planes defined by the vector to the sun and the normals to the surface. The measurements were calibrated by photographing the photometric target before and after each survey. The photometric stability of the camera between these measurements appears to be within 10%.

The video signal from the spacecraft was converted to film images by a flying spot scanner photo recorder. The latitude of the film (SO-337) is great enough so that the entire video transfer characteristic may be recorded on the linear portion of the film. A high degree of stability exists between different film records. A transfer characteristic from such a negative, determined from observation of the photometric target on the spacecraft during lunar operation, is shown in Fig. III-26.

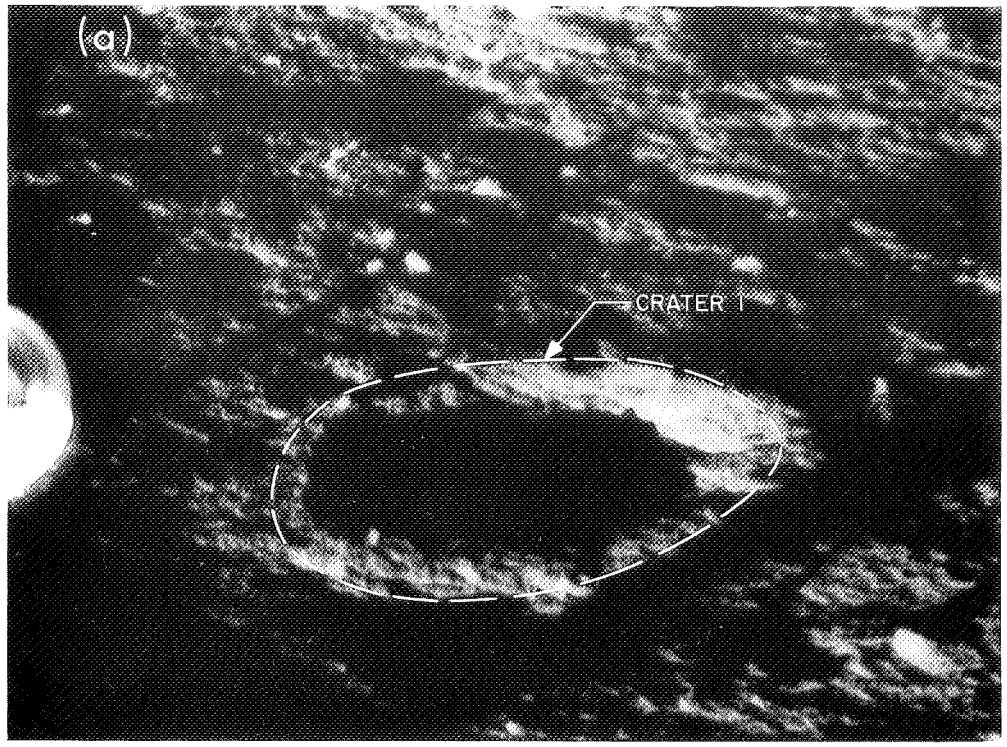

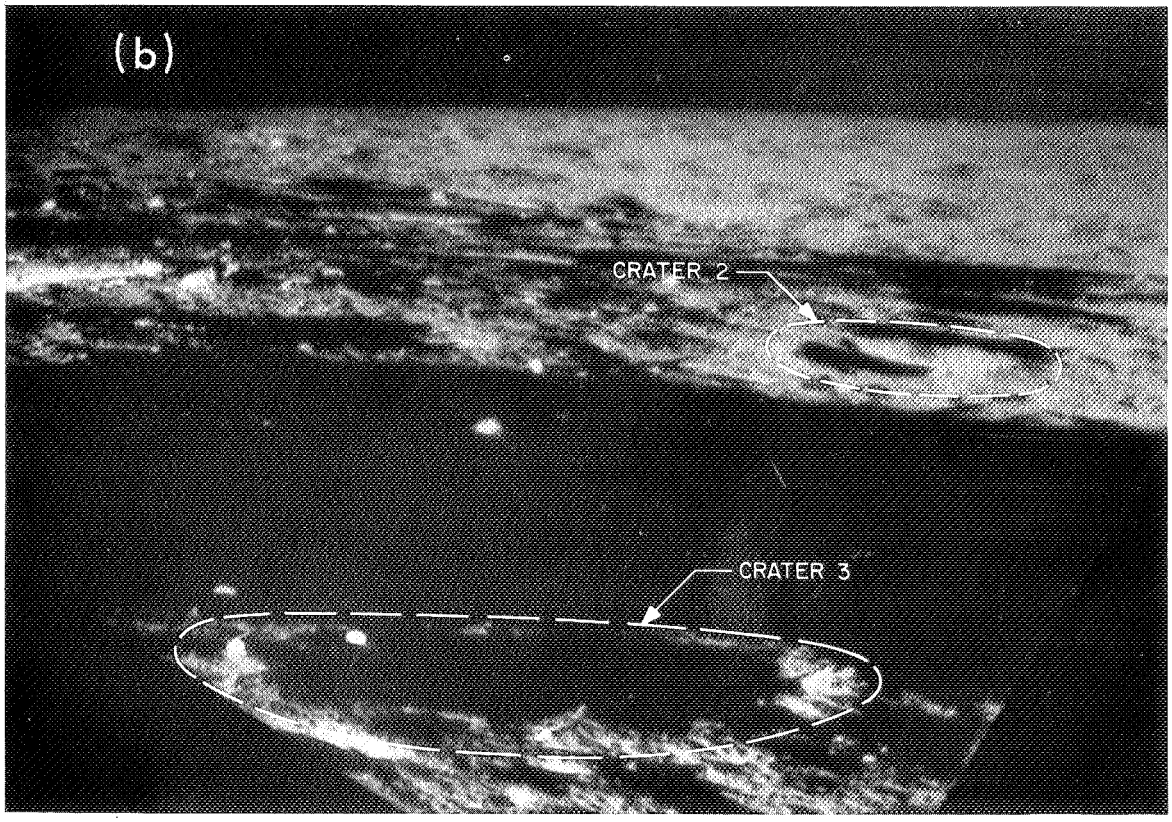

Fig. III-24. Typical examples of craters with raised rims

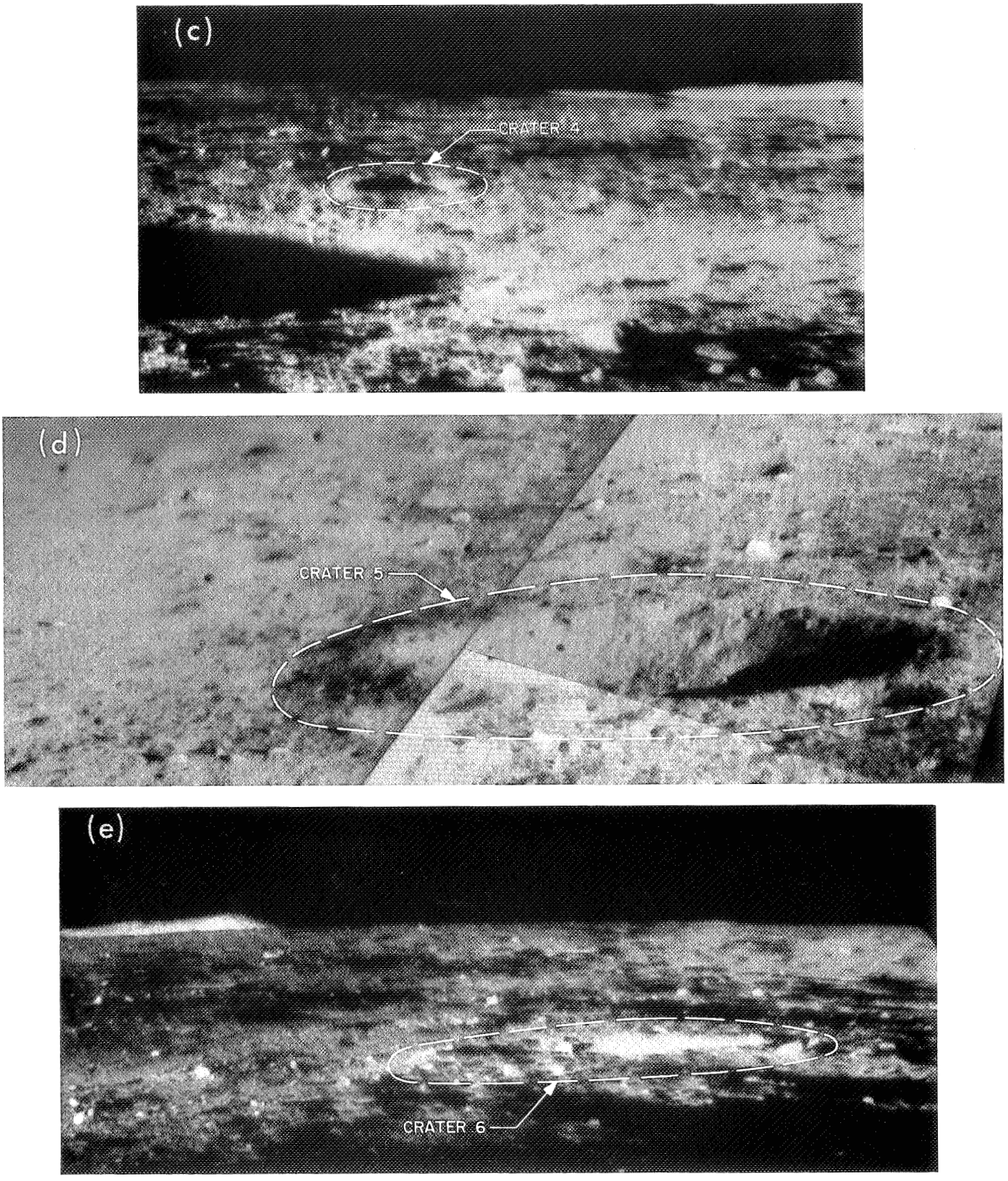

Fig. III-24. Typical examples of craters with raised rims (cont'd)

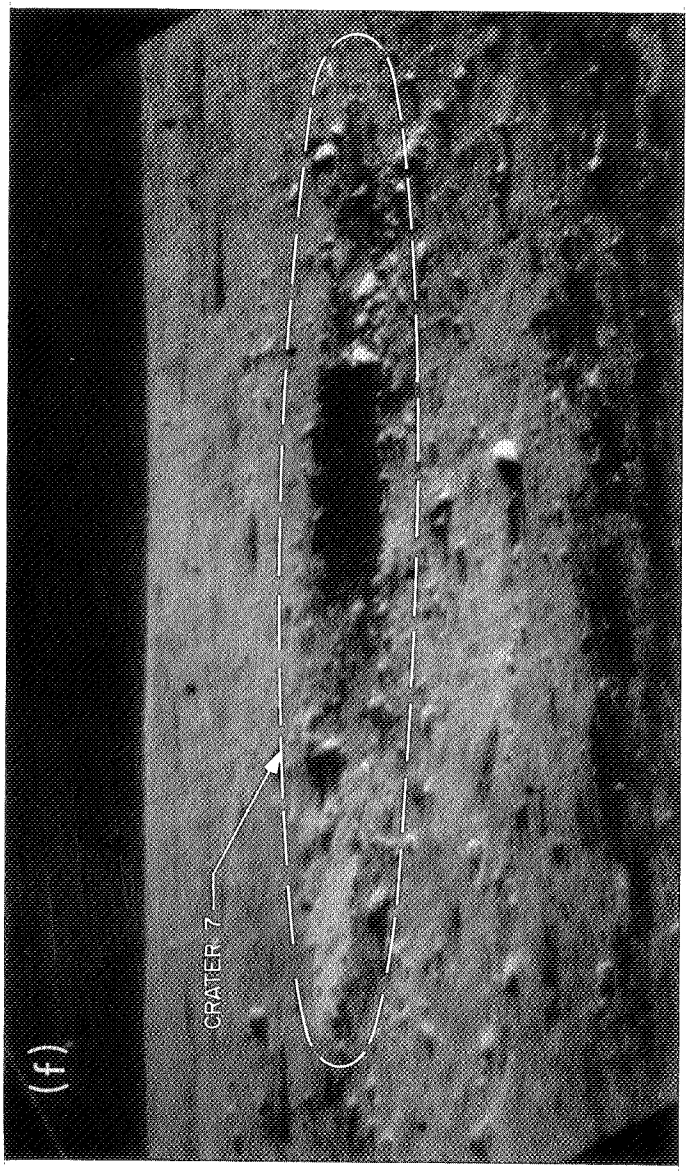

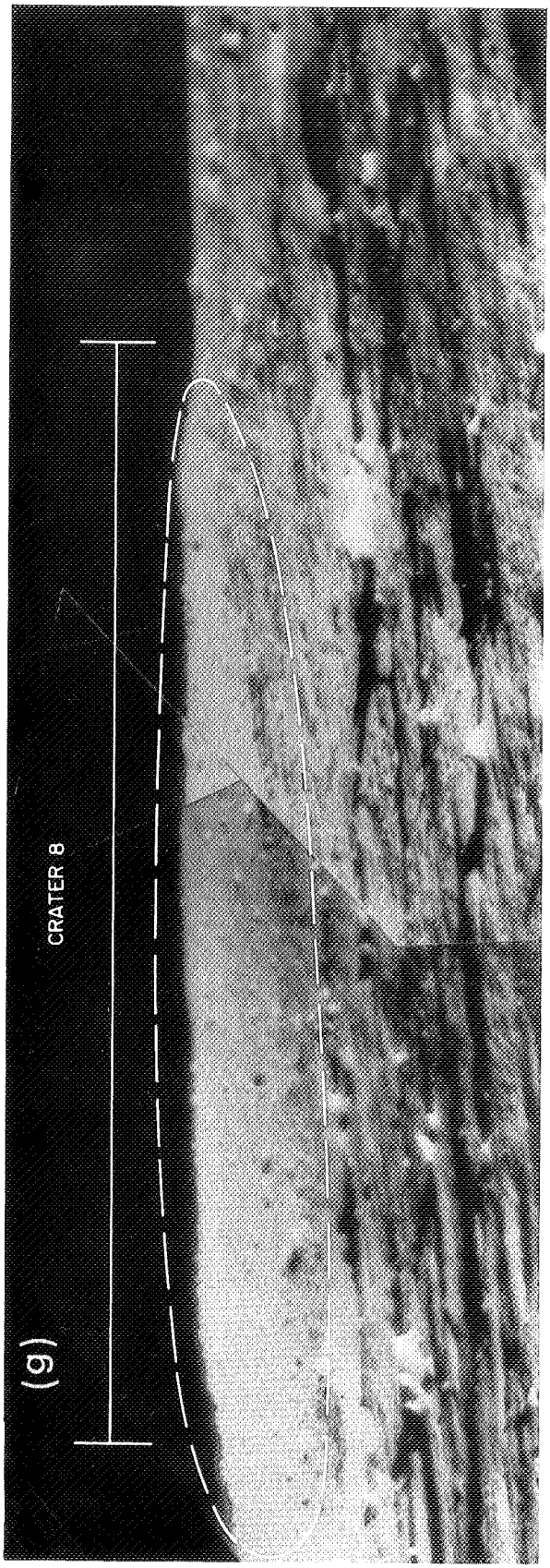

Fig. III-24. Typical examples of craters with raised rims (cont'd)

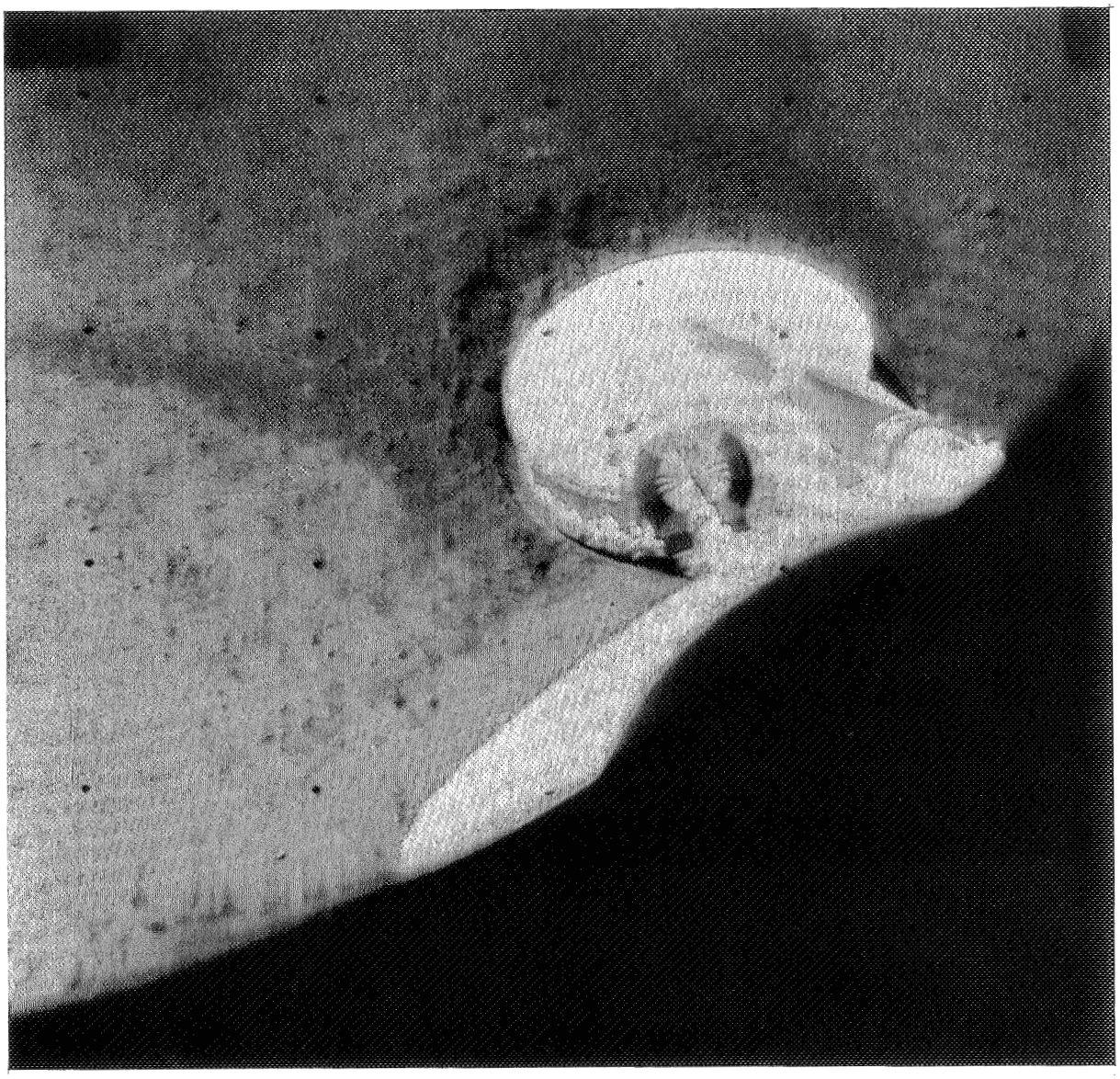

Fig. III-25. Wide-angle picture of footpad 2

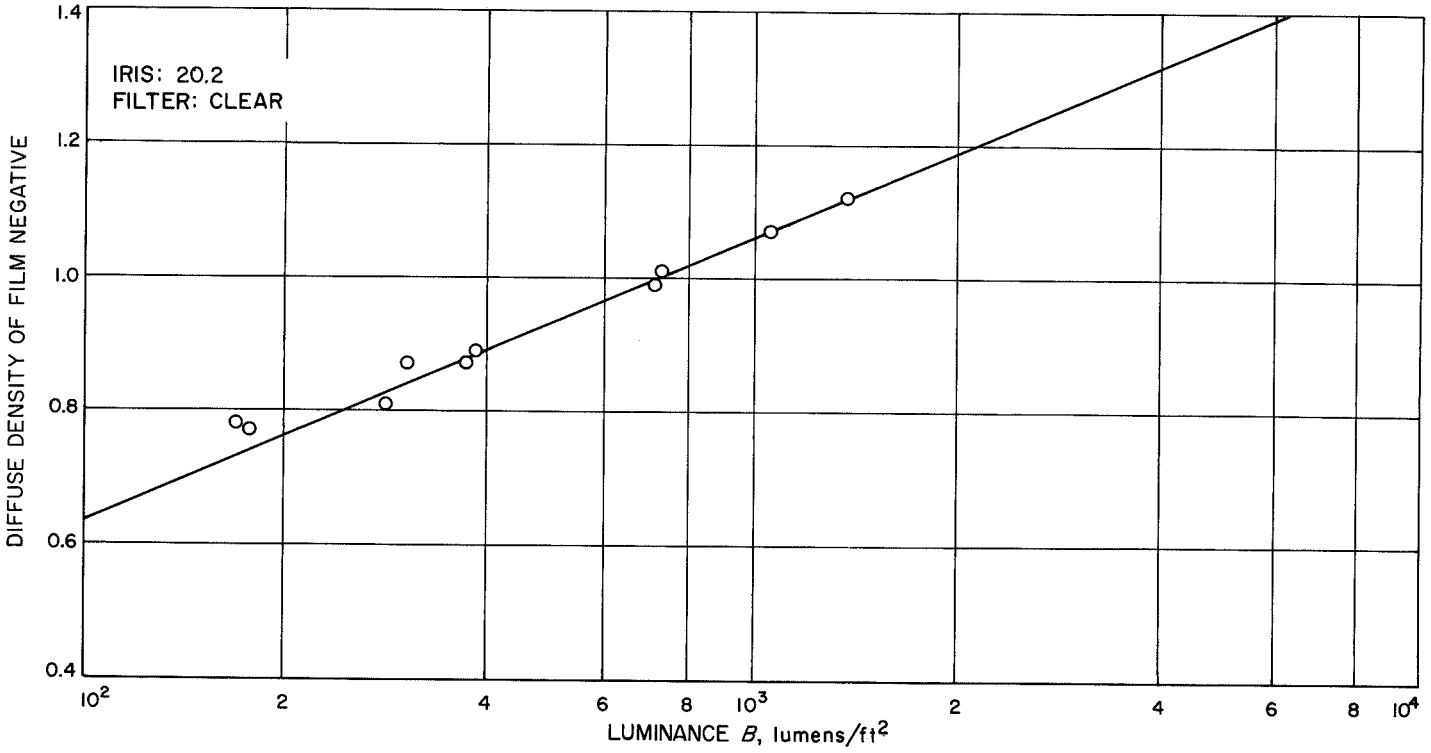

Fig. III-26. Total TV system transfer characteristic function

Photometric control was maintained in the ground-recording system by an eight-step electronic grey scale recorded with each TV image. This scale was generated so that the camera black level and a predetermined white level formed the maximum and minimum density limits, with the remaining steps equally divided with respect to the video signal voltage output. The electronic scale could then be used for photometric control between frames; thus, it was possible to relate film density to camera video voltages.

The estimated luminance from each step of the photometric target was computed using the preflight calibration data in conjunction with the photometric angles of phase, incidence, and emergence. The photometric targets were mounted on spacecraft leg 2 and omni-antenna B so that the normal to the target was approximately colinear with the camera center line-of-sight vector, thus simplifying the calculation of the angles of incidence. The steps on the photometric target were calibrated during preflight tests by a goniophotometer arranged for normal observation, while the angle and plane of incidence were varied. The radiance factor, defined as the ratio of the radiance to that of the irradiance at normal incidence, was plotted against the angle of incidence (Fig. III-27). A simple multiplication of the radiance factor at a given angle of incidence by the estimated solar illumination gives an estimated luminance of the grey steps on the photometric target.

Terrain target areas for photometric measurements of the lunar surface were selected on the basis of surface flatness and homogeneity. The areas were selected at azimuth angles of approximately 0, 45, 90, 135, 180, 225, and 220° and at elevation angles of −15, − 30, −45, and −60° in the local selenographic coordinate system. The photometric geometry must be reconstructed in order to make meaningful measurements. The target area photocoordinates were reduced by graphical transformation to elevation and azimuth. The line-of-sight vector to a selected target area represents the negative of the emergent flux vector. By assuming that the target areas selected for the photometric measurements are level, the angles of incidence, emergence, and phase can be computed from the sun vector and the emergent flux vector. From these angles, the "brightness longitude" angle α may be computed as well as the azimuth angle A between the incident and emergent planes.

Density of the film was measured with a densitometer with a constant sampling aperture equivalent to 0.8° for the wide-angle frames and 0.2° for the narrow-angle

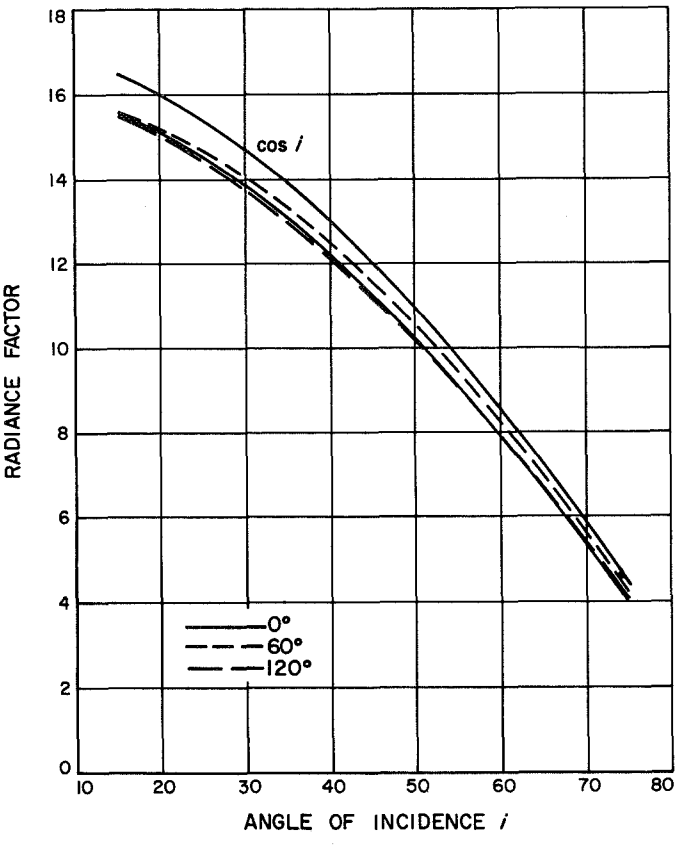

Fig. III-27. Photometric chart calibration

frames of the photometric target. Typical plots relating the electronic-generated grey scale and photometric target are shown in Figs. III-28 and III-26.

The film densities of the selected areas were first compared to the electronic grey scale of that frame, and the luminances were read from the transfer characteristic of the frame of the photometric target closest in time. Corrections for iris and filter differences were applied to the luminance values computed for the selected areas.

A preliminary reduction has been made of ten photometric measurements at 0° camera azimuth (east), eight measurements at −90° camera azimuth (south), and one measurement of an area with a phase angle of 3° and $\alpha = +45°$ (Fig. III-29). These data, when fitted to a photometric function similar in form to that obtained by Fedorets and others (see Ref. III-11), suggest that the average normal albedo or direct reflectance of the lunar surface in the vicinity of the spacecraft is about 6%.

Preliminary reduction of colorimetric measurements from film-recorded data reveals that only minor color differences can be present in the lunar surface materials.

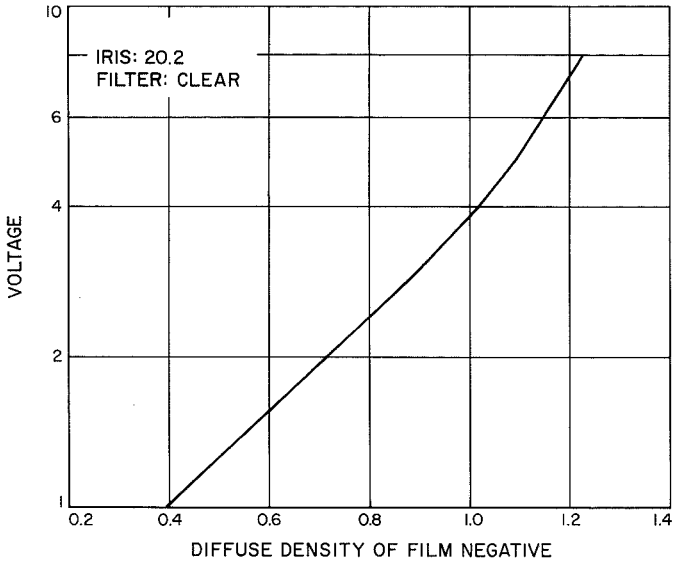

Fig. III-28. Typical plot of measured film density versus voltage from electronic grey scale

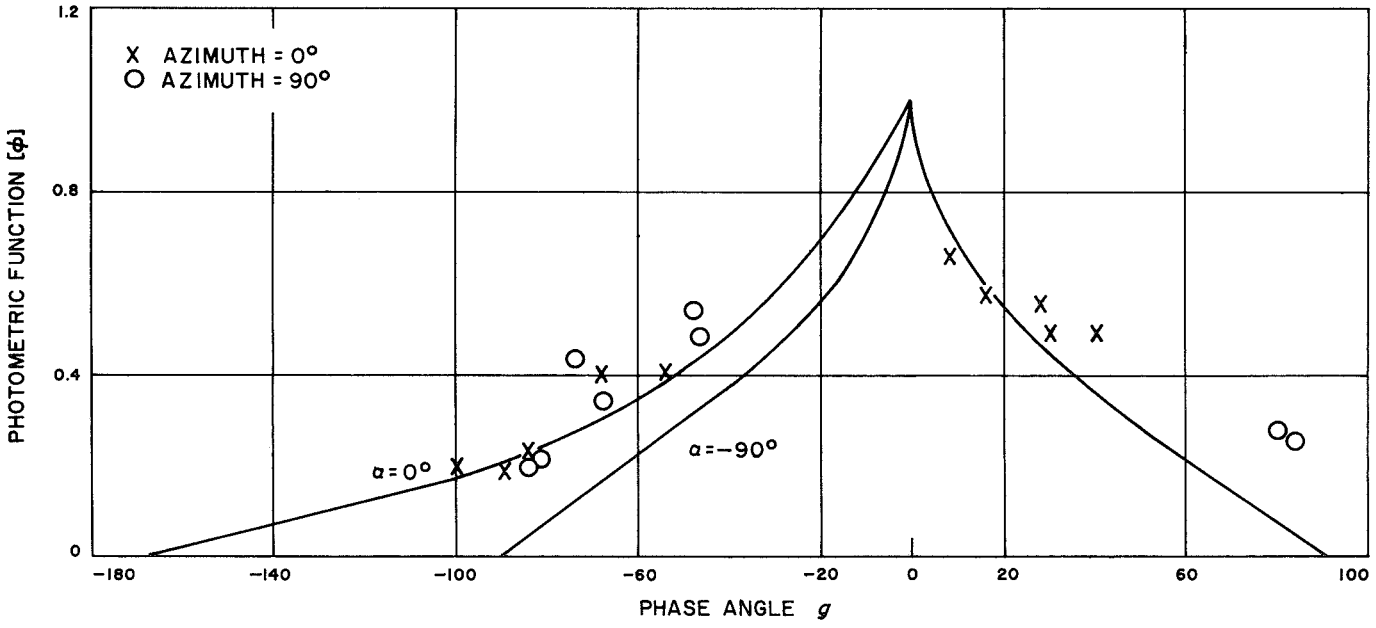

Fig. III-29. Photometric function versus phase angle. (Curves are mean values of terrestrially observed data.)

The absence of major color differences in the lunar surficial materials is somewhat surprising in view of the observed differences in albedo. The overall color appearance of the lunar surface is dark grey.

REFERENCES

III-1. *Surveyor I Preliminary Results: National Aeronautics and Space Administration Five-Day Science Report*, Project Document No. 97, Jet Propulsion Laboratory, Pasadena, Calif., June 30, 1966.

III-2. Whitaker, E. A., "Surveyor I: Landing Site Location," *Science*, July 1966 (to be published).

III-3. Jaffe, L. D., et al., "Surveyor I: Preliminary Results," Science, Vol. 152, No. 3730, pp. 1737–1750, June 24, 1966.

III-4. *Surveyor I: A Preliminary Report*, NASA SP-126, Compiled by Lunar and Planetary Programs Division, Office of Space Science and Applications, National Aeronautics and Space Administration, Washington, D.C., June 1966.

III-5. White, Robert, J., Rosenberg, Alan D., Fisher, Peter S., Harris, Raymond A., Newhall, Nicholas S., *SPACE — Single Precision Cowell Trajectory Program*, Technical Memorandum No. 33-198, Jet Propulsion Laboratory, Pasadena, Calif., January 15, 1965.

III-6. Trask, N. J., "Size and Spatial Distribution of Craters as Estimated From the *Ranger* Photographs," *Rangers VIII and IX: Part II. Experiments, Analyses, and Interpretations*, Technical Report No. 32-800, pp. 252–263, Jet Propulsion Laboratory, Pasadena, Calif., March 15, 1966.

III-7. Lebedinskiy, A. I., *Scientific Results of Processing of Panoramas Obtained From Photographs of the Lunar Surface Taken From Luna 9*, National Aeronautics and Space Administration, Goddard Space Flight Center, Contract No. NAS-5-9299, ST-LPS-10493/Revision 1, from Reprint of the USSR Academy of Sciences, Izdatel'stbo "NAUKA," 1966.

III-8. Moore, H. J., "Cohesion of Material on the Lunar Surface," *Rangers VIII and IX: Part II. Experiments, Analyses, and Interpretations*, Technical Report No. 32-800, pp. 263–270, Jet Propulsion Laboratory, Pasadena, Calif., March 15, 1966.

III-9. Gault, D.E., Quaide, W. L., Overbeck, V. R., and Moore, H. J., "Luna 9 Photograph; Evidence for a Fragmental Surface Layer," *Science*, Vol. 153, No. 3739, pp. 985–988, August 26, 1966.

III-10. Shoemaker, E. M., *Ranger VII: Part II. Experiments, Analyses, and Interpretations*, Technical Report No. 32-700, Jet Propulsion Laboratory, Pasadena, Calif., February 10, 1965.

III-11. Willingham, D. E., *Lunar Reflectivity Model for Ranger Block III Analysis*, Technical Report No. 32-664, Jet Propulsion Laboratory, Pasadena, Calif., November 2, 1964.

ACKNOWLEDGMENT

Many thanks are extended to all the individuals who contributed technical support to the topographic section of this report. Special appreciation is extended to Henry Holt, U.S. Geological Survey, for his major contribution to the photometric reduction.

IV. LUNAR SURFACE THERMAL CHARACTERISTICS

J. W. Lucas, J. E. Conel, R. R. Garipay, W. A. Hagemeyer, and J. M. Saari

Surveyor I presented the first opportunity to obtain *in situ* estimates of the lunar surface temperature and thermophysical characteristics, in addition to engineering data on the thermal behavior of the spacecraft during operation on the lunar surface. It is to be emphasized that the spacecraft carried no instruments, as such, to measure lunar surface temperatures or surface thermal characteristics. In fact, the spacecraft was, to the greatest extent possible, thermally isolated from the lunar surface to provide operation at the same temperature in flight and during daytime on the surface. Fortunately for the present analysis, temperatures of the outer surfaces of two electronic compartments were highly dependent on the local thermal radiation environment and largely independent of internal spacecraft temperatures. These spacecraft temperatures have been used to estimate the average brightness temperature[1] of those portions of the surface viewed by each compartment.

In this manner, *Surveyor I* provided estimates of surface temperature out to approximately 18 m from the compartments. Compared to the best previous infrared telescopic observations with a resolution of 18 km, this is an improvement in ground resolution of a factor of 1000. During the first lunar day, the spacecraft operated until approximately 21:00 GMT, June 16, 1966; temperature data from both compartments are available to that date, which is 2 days after local sunset.

The calculated lunar surface temperatures and their variation with time throughout the lunar day and night have been used to estimate the local thermal properties of the surface. This is accomplished by comparing the *Surveyor I* results with theoretically predicted surface temperatures throughout a lunation. The temperature scales on curves in Ref. IV-1 have been adjusted to correspond with values of surface albedo and solar insolation at the *Surveyor I* site. On this basis, *Surveyor I* thermal data indicate the surface to be highly insulating, as predicted from earth-based observations. Furthermore, the effects of non-Lambertian surface thermal emission, a feature of lunar infrared behavior also observed from earth and often ascribed to surface roughness, were apparently sensed by *Surveyor I*. Together with detailed photographic cover-

[1]Brightness temperature is the temperature that the surface would have if its emittance were unity.

age of the surface, these thermal data provide a unique advantage in studying the peculiar radiative behavior of the surface.

In the following paragraphs, a summary is given of pertinent terrestrial infrared and photometric observations of the *Surveyor I* site. Then the procedures used to arrive at surface temperatures are described in detail. A comparison is presented of *Surveyor I* data and theory. The section concludes with a discussion of dust coverage of the spacecraft from a thermal standpoint.

A. Earth-Based Lunar Surface Data

1. Albedo of *Surveyor I* Landing Site

The albedo of the landing site was determined from full moon measurements (Ref. IV-1) of the reflected light from the illuminated lunar disk. A value of 0.052 was obtained using the scale given in Ref. IV-2, which refers to the brightness at a 7° average phase angle. Statistical studies of the distribution of albedo over the disk (*unpublished*) show that the darkest regions on the moon have a value of 0.050 on this scale; the brightest region has a value greater than 0.20. On this basis, the landing site has an albedo only 4% greater than the darkest regions on the moon.

The measurements from which this value was obtained were to a resolution of 10 sec of arc, or 18 km at the center of the disk. Therefore, the albedo of the region in the immediate vicinity of the spacecraft could depart considerably from the quoted value of 0.052.

2. Thermophysical Properties of *Surveyor I* Landing Site

The thermophysical properties are generally determined from eclipse or lunation cooling curves. The most extensive measurements are those of Refs. IV-3 and IV-4, made during the December 19, 1964, eclipse. Isotherms during totality for the equatorial region have been published (Ref. IV-5); these measurements reveal that the lunar surface exhibits a heterogeneity previously unsuspected. The most prominent features are "hot spots" usually associated with craters, which are distributed over the entire disk. Isotherms in the region of the *Surveyor I* landing site have been transferred to the Lunar Aeronautical Chart for the area (Fig. IV-1). In the area, the craters Flamsteed and Flamsteed B are prominent hot spots. It can be seen that the region where *Surveyor I* landed is in an area with small horizontal thermal gradients; thus, it has the highly insulating properties that typify the general lunar surface. However, the eclipse measurements revealed anomalous cooling of features of a wide range of sizes, varying from craters several kilometers in diameter to maria. It would not, therefore, be surprising if thermal heterogeneity were found to dimensions much smaller than possible to measure by the eclipse measurements; for example, any areas strewn with sizable boulders should appear to cool more slowly than unstrewn areas.

3. Predicted Local Surface Temperatures

Figure IV-2 shows predicted local surface temperatures (derived from Ref. IV-6) for the *Surveyor I* site for June 1966. The curves, taken in part from Ref. IV-6, are for different values of the thermal parameter $(k\rho c)^{-1/2}$, where k is the thermal conductivity, ρ the density, and c the heat capacity. The temperature scale was adjusted so that the maximum temperature for the $(k\rho c)^{-1/2} = 1000$ curve corresponds to the calculated temperature for the *Surveyor I* site, taking into account the sun–moon distance and the effect of local albedo. The latter correction was made using data of Ref. IV-1, in particular, the authors' infrared and visible measurements on the full moon in the region of the sub-solar point, where the change of temperature, which resulted from the change in albedo, was determined.

B. Spacecraft Raw Data

1. Spacecraft Description

The basic structure of the *Surveyor* spacecraft (Fig. IV-3) is made up of tubular aluminum, which serves as a tetrahedral mounting structure for the electronic gear and propulsion subsystems. The three spacecraft legs are attached at the three corners of the structure's base. The spherical main retro engine is nestled in the center of the tetrahedral structure during the transit portion of the mission and is ejected following burnout; consequently, the inner structural members are exposed to the lunar surface throughout the lunar day. The high-gain antenna and solar panel, which are mounted on a mast that protrudes approximately 1 m above the apex of the structure, cast varying shadow patterns on the structural members and spacecraft subsystems throughout the lunar day. Changes in shadow patterns result from repositioning of the antenna and solar panel, as well as from the normal movement of the sun at about 0.5°/hr.

The thermal finish of the structural members is a combination of inorganic white paint and polished aluminum. Generally, the white paint is applied to all top and visible-side surfaces of the structure; the underside of the surface is polished metal. This thermal finish distribution provides a low-solar-absorptance white paint surface in

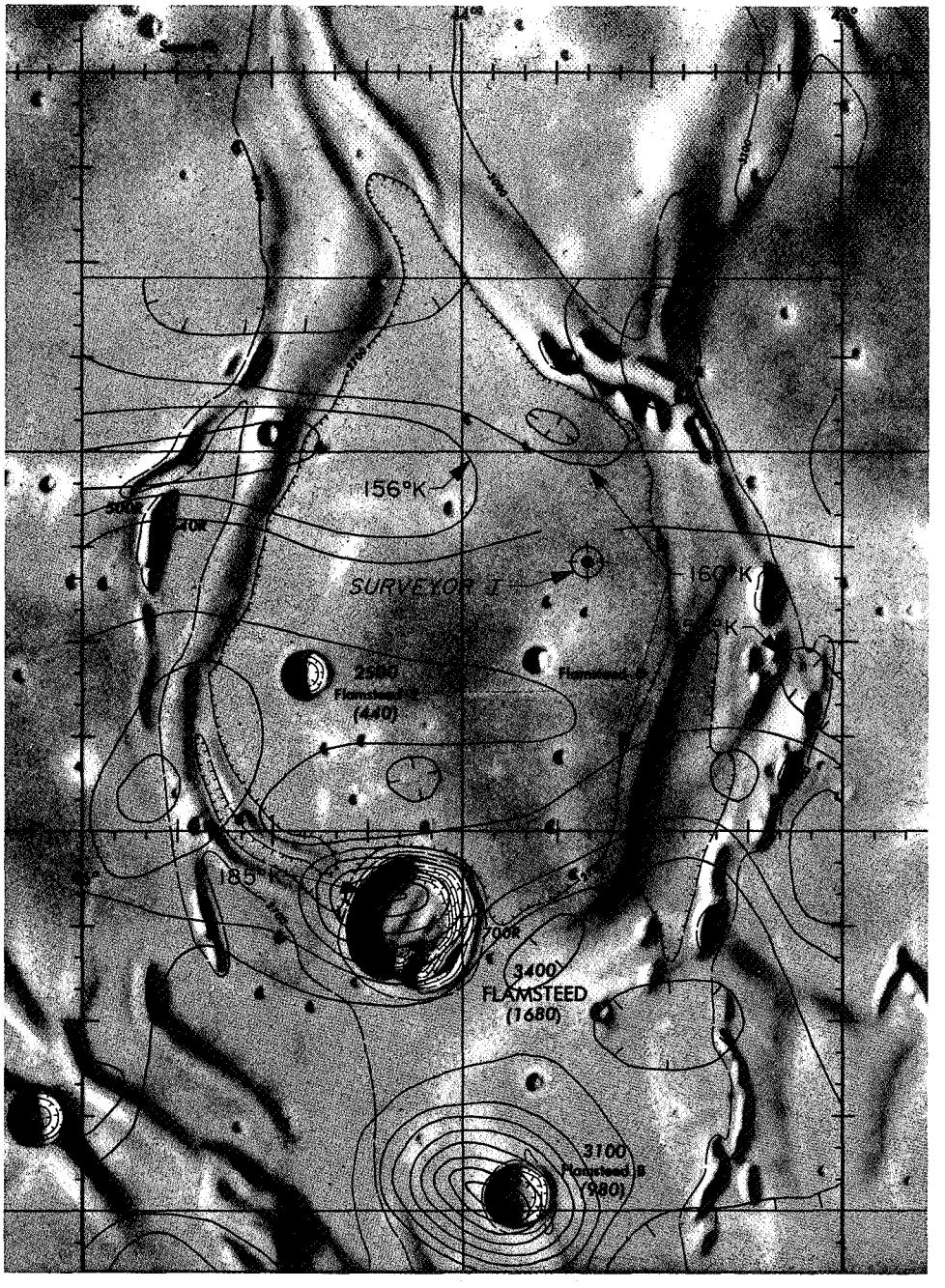

Fig. IV-1. Isotherms in landing site region during totality of lunar eclipse (Ref. IV-1)

the sun-illuminated areas with a high-emittance coupling to space in the infrared regions; the polished aluminum underside of the structure tends to isolate the spacecraft from the hot lunar surface.

a. Thermal instrumentation. *Surveyor* carries 75 platinum resistance temperature sensors, which are located at various points throughout the spacecraft; primary consideration was given to operational hardware and key thermal interfaces. Each sensor is individually calibrated to $\pm 1°C$; other system inaccuracies degrade the data to $\pm 3°C$.

For the purpose of calculating apparent lunar surface temperature as a function of time of lunar day, it is desirable to use sensors that have a strong coupling to the lunar surface, but are well-isolated from spacecraft in-

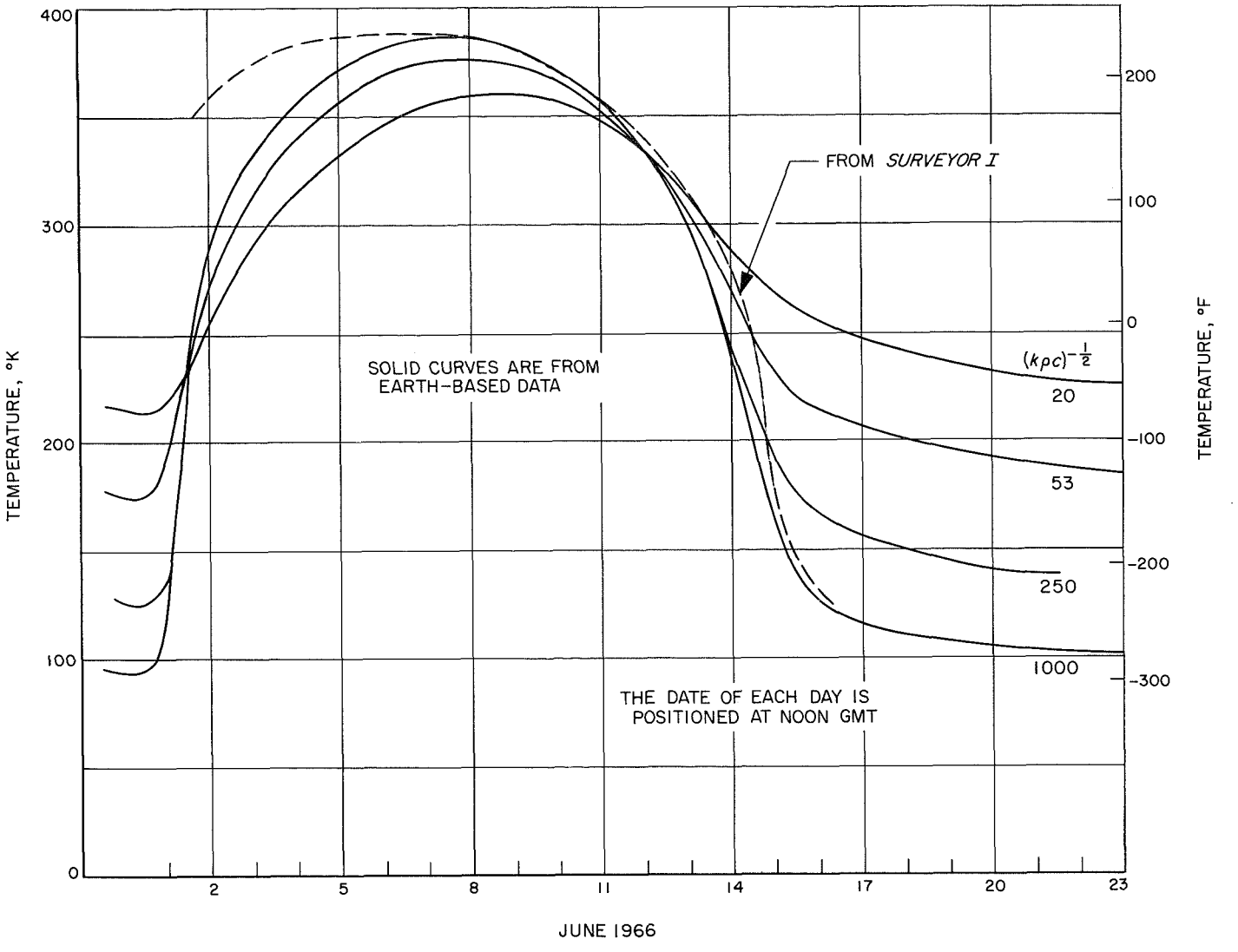

Fig. IV-2. Lunar surface brightness temperature at *Surveyor I* site

fluences. Two temperature sensors seem to satisfy these requirements; they are located on the outboard faces of compartments A and B. Because the design is the same for each compartment, the following discussion applies to both.

Compartment canister and environment description. The compartment A and B canisters (Figs. IV-4 and IV-5) are thin aluminum shells [0.4 mm (0.016 in.), 2024 aluminum]; their purpose is to contain a 75-layer blanket of superinsulation that surrounds each compartment. The largest part of the top surface of each compartment is covered with Vycor glass second-surface mirrors. These mirrors are part of the bimetallic-actuated thermal switches used to reject heat from the temperature-controlled compartments. The selected temperature sensors are mounted approximately in the geometric center of the outboard face. (It should be noted that this face contains corrugations.) The sensors are bonded to the polished aluminum inner surface of the canister (i.e., the surface facing the superinsulation).

The canisters are reasonably well isolated from the remainder of the compartment and spacecraft structure; therefore, they are in thermal equilibrium with their environment, which is made up primarily of the lunar surface, space, and a variable amount of solar energy input. The superinsulation isolates the surfaces from the inside of the compartment so that the heat input from that boundary is negligible during the lunar day. This assumption is not valid when an attempt is made to calculate lunar surface temperatures during the lunar night.

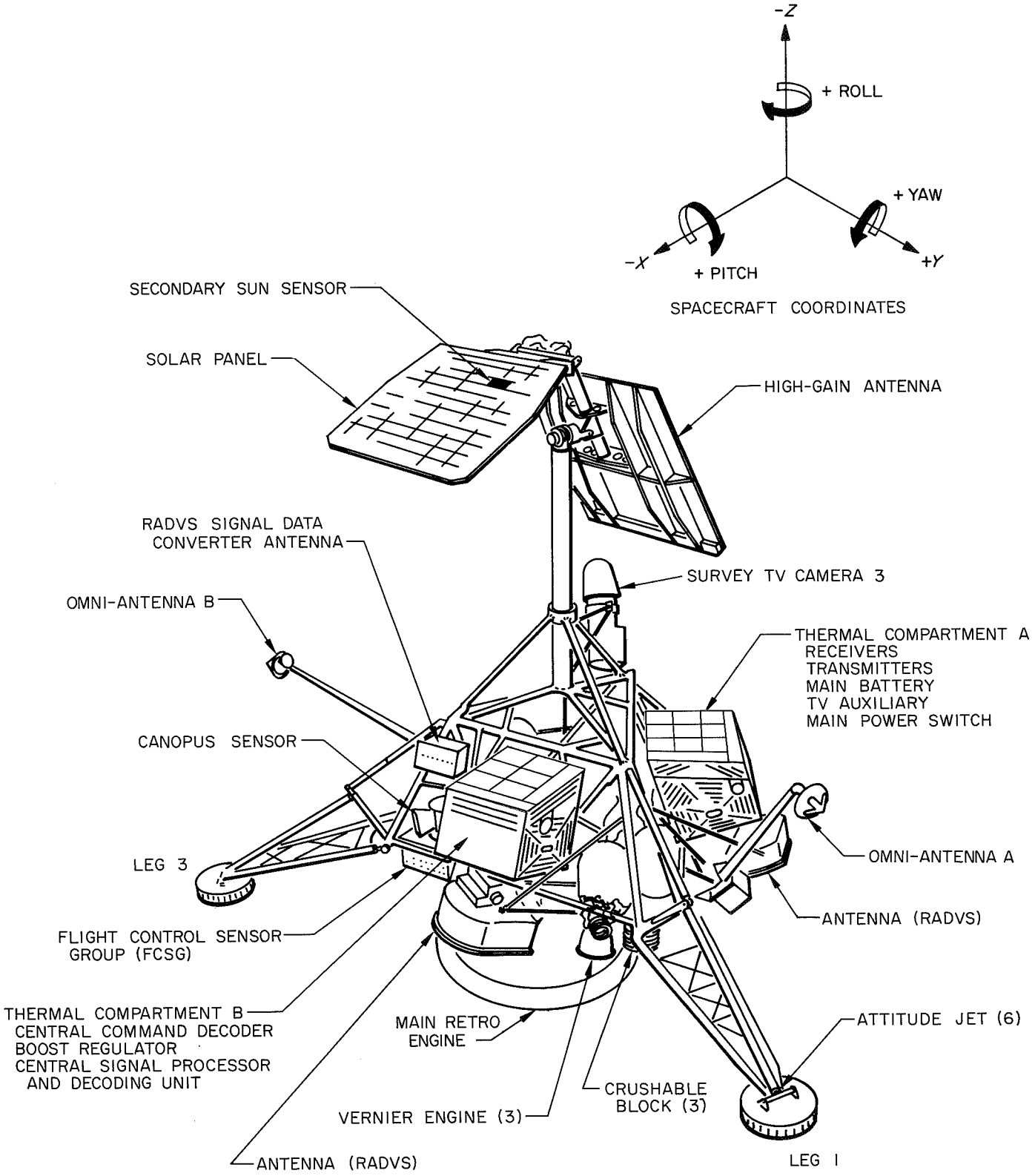

Fig. IV-3. *Surveyor* spacecraft configuration

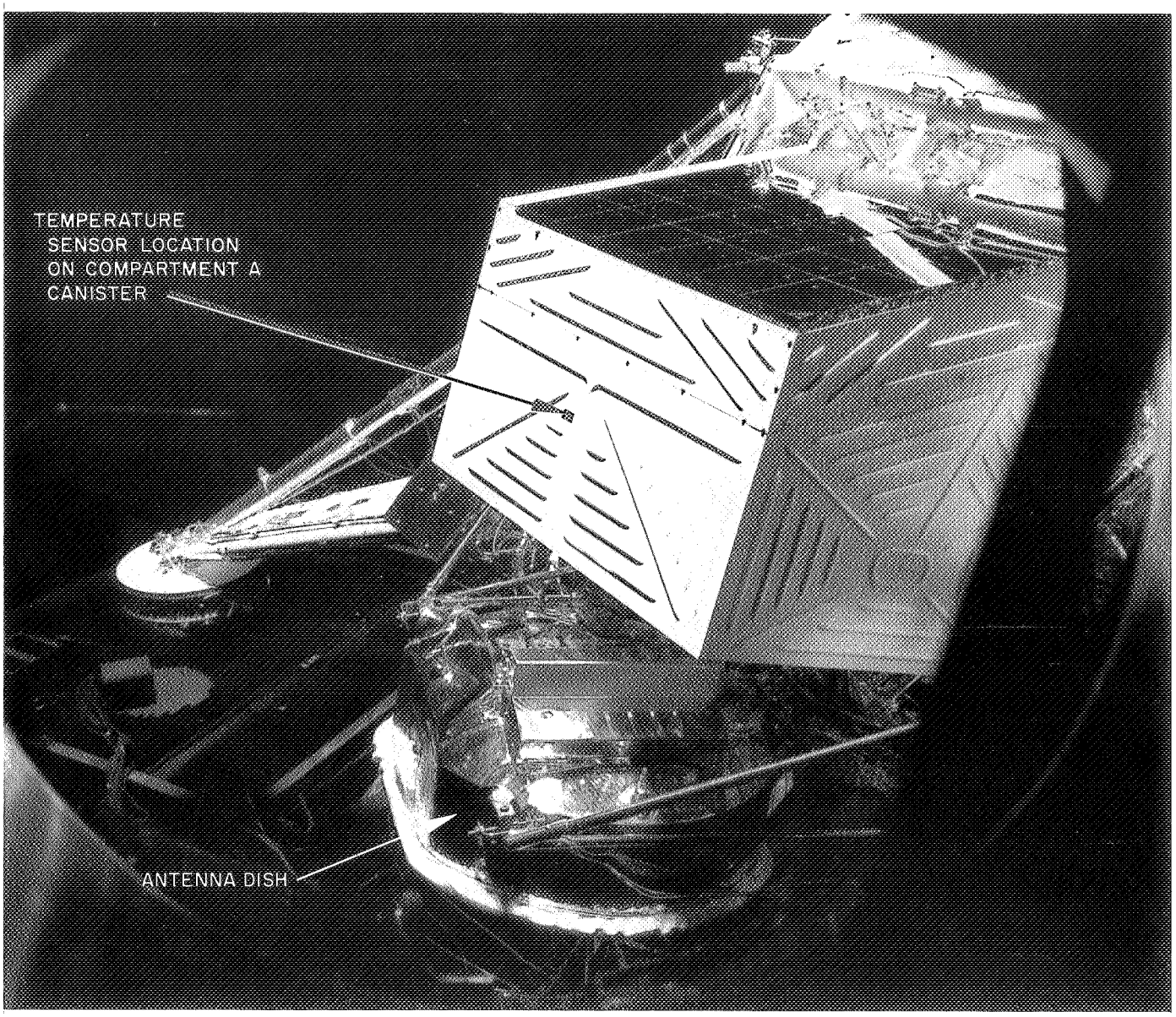

Fig. IV-4. *Surveyor* model showing compartment A

The following, more detailed, list of environmental parameters and thermal properties is of significance in arriving at lunar surface temperatures:

(1) Spacecraft landing site.
  (a) 2.58° south latitude.
  (b) 43.35° west longitude.

(2) Outboard face.
  (a) Angle with spacecraft Z-Z axis 21 ±1°.

(3) Configuration factors from outboard face as measured on prototype spacecraft.
  (a) 0.69 (compartment A to space).
    0.03 (compartment A to antenna dish).
    0.28 (compartment A to lunar surface).
  (b) 0.69 (compartment B to space).
    0.02 (compartment B to antenna dish).
    0.29 (compartment B to lunar surface).

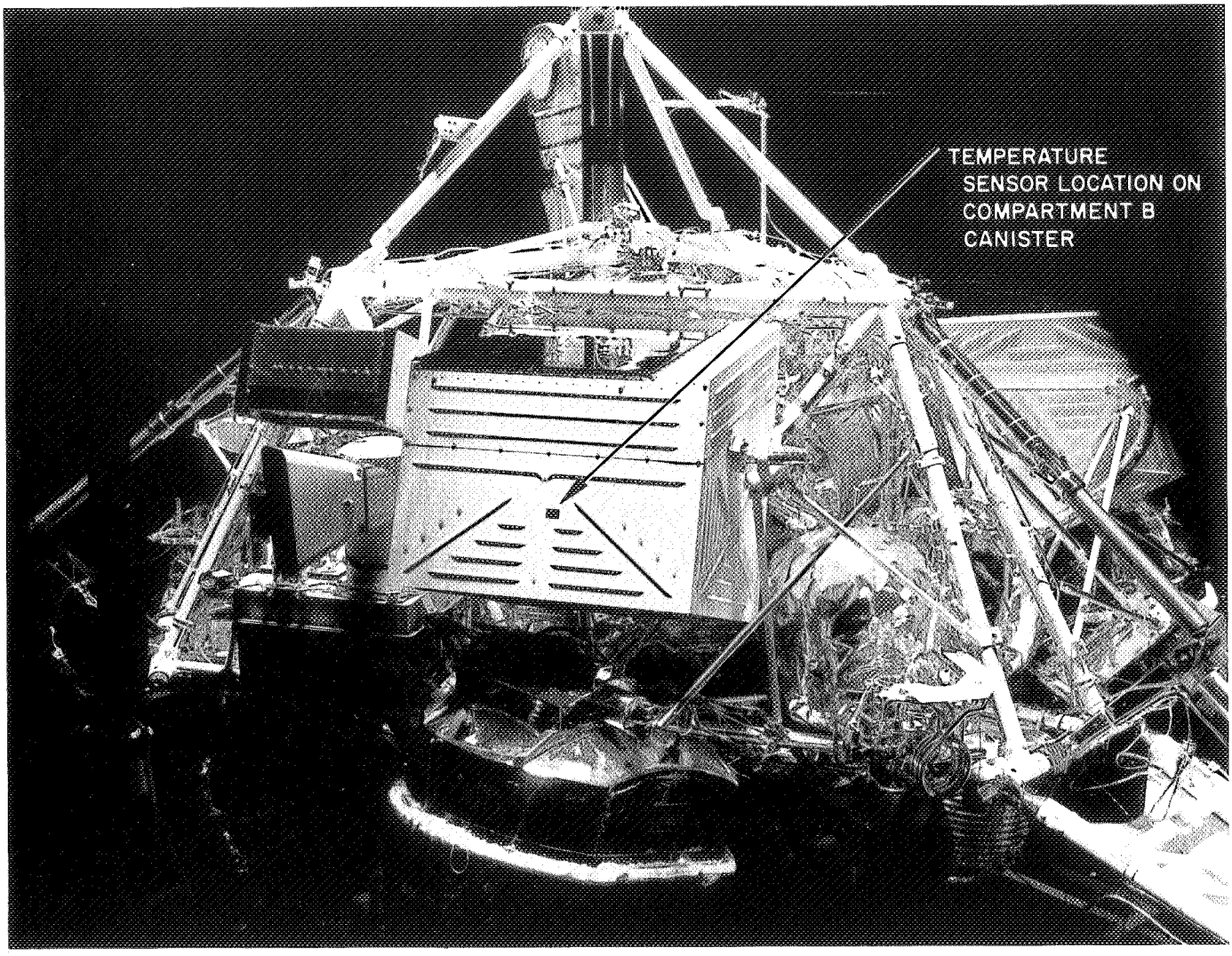

Fig. IV-5. Surveyor model showing compartment B

(4) Compartment canister properties.

(a) $\varepsilon_H = 0.87 \pm 0.02$ (infrared hemispherical emittance).

(b) $\alpha = 0.20 \pm 0.02$ (solar normal absorptance).

(c) Material: 2024 aluminum, 0.4 mm (0.016 in.) thick, coated with inorganic white paint.

(d) Typical side dimension on compartment: approximately 0.5 m.

(5) Antenna dish properties.

(a) Construction: Parabolic antenna dish consisting of fiberglass honeycomb sub-structure with aluminum foil bonded to honeycomb and vapor-deposited aluminum covering aluminum foil. Vapor-deposited aluminum appears dimpled because of 6.25-mm (0.25-in.) fiberglass honeycomb sub-structure to which thin face sheets are bonded.

(b) Thermal properties: $\alpha = 0.10 \pm 0.02$ (solar normal absorptance of dish); $\varepsilon_H = 0.04^{+0.02}_{-0.01}$ (infrared hemispherical emittance of dish).

(6) Temperature data accuracy: $\pm 3°C$ for all temperature data[2].

[2]Because of the preliminary nature of the spacecraft temperature data presented here, the accuracy of the curves, faired through the data points shown in Figs. IV-7 and IV-8, is quoted as $\pm 3°C$. However, especially for the data during the lunar afternoon, there may be an additional error of $\pm 3°C$ in individual data points. Further data reduction is necessary to improve accuracy.

(7) Conduction effects between outboard face of canister and adjacent sides have not been evaluated because no temperature sensors exist on adjacent sides.

Figure IV-6 shows the approximate landed spacecraft orientation. The extent of shading of the outboard face throughout the lunar day is shown in Figs. IV-7 and IV-8. The angle between a normal to the canister outboard face and the solar rays is presented in Figs. IV-9 and IV-10. It should be noted that, for the computations shown in Figs. IV-9 and IV-10, the sun was assumed to move in a plane passing through the landing site and tilted 3° to the north. Representative raw temperature data are plotted in Figs. IV-7 and IV-8. Shading produced by the solar panel and planar array antenna is primarily responsible for the sudden changes in canister temperatures during portions of the lunar day.

C. *Initial Engineering Analysis of Raw Data*

1. Lunar Surface Temperature Calculation

The calculations were performed on the basis of data transmitted by the compartment B sensor on *Surveyor I*.

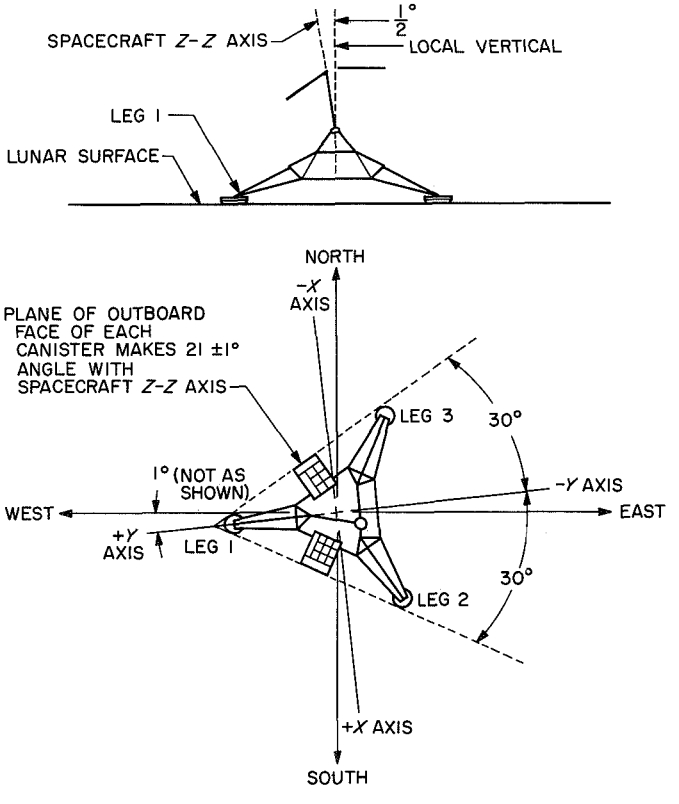

Fig. IV-6. *Surveyor I* spacecraft landed orientation

It has been assumed that only radiative heat interchange takes place between the sources (Fig. IV-11).

The radiant flux density balance for the compartment surface can be expressed by

$$\varepsilon_1 \sigma T_1^4 = (F_{12} - F_{13})\,\varepsilon_1 \varepsilon_2 \sigma T_2^4 + F_{13}\,\varepsilon_1 \varepsilon_2 \sigma T_3^4 + (F_{12} - F_{13})\,\rho_2 \alpha_{1S} S \sin \phi + \alpha_{1S} S \cos \beta \pm \dot{q} \quad (1)$$

where

T_1 = compartment surface temperature

T_2 = lunar surface temperature

T_3 = lunar surface temperature in shadow

S = solar irradiation constant

F_{12} = geometric view factor from 1 to 2

F_{13} = geometric view factor from 1 to 3

σ = Boltzmann's constant

α_{1S} = compartment surface solar absorptance

ε_1 = compartment surface emittance

ε_2 = lunar surface emittance

ρ_2 = lunar reflectivity to solar irradiation

ϕ = sun angle (between lunar surface and sun rays)

β = angle between sun rays and normal to compartment surface from Fig. IV-8

$\dot{q}$ = conduction heat flux between inside and outside of compartment wall

By rearranging Eq. (1), we have

$$\sigma T_2^4 = \frac{\sigma T_1^4}{\varepsilon_2 (F_{12} - F_{13})} - \frac{F_{13}}{F_{12} - F_{13}} \sigma T_3^4 - \frac{\alpha_{1S} S}{\varepsilon_1 \varepsilon_2 (F_{12} - F_{13})} \times [(F_{12} - F_{13})\,\rho_2 \sin \phi + \cos \beta] \pm \frac{\dot{q}}{\varepsilon_1 \varepsilon_2 (F_{12} - F_{13})} \quad (2)$$

For compartment B, $F_{13} \cong 0$; thus,

$$\sigma T_2^4 = \frac{\sigma T_1^4}{\varepsilon_2 F_{12}} - \frac{\alpha_{1S} S}{\varepsilon_1 \varepsilon_2 F_{12}} (F_{12}\,\rho_2 \sin \phi + \cos \beta) \pm \frac{\dot{q}}{\varepsilon_1 \varepsilon_2 F_{12}} \quad (3)$$

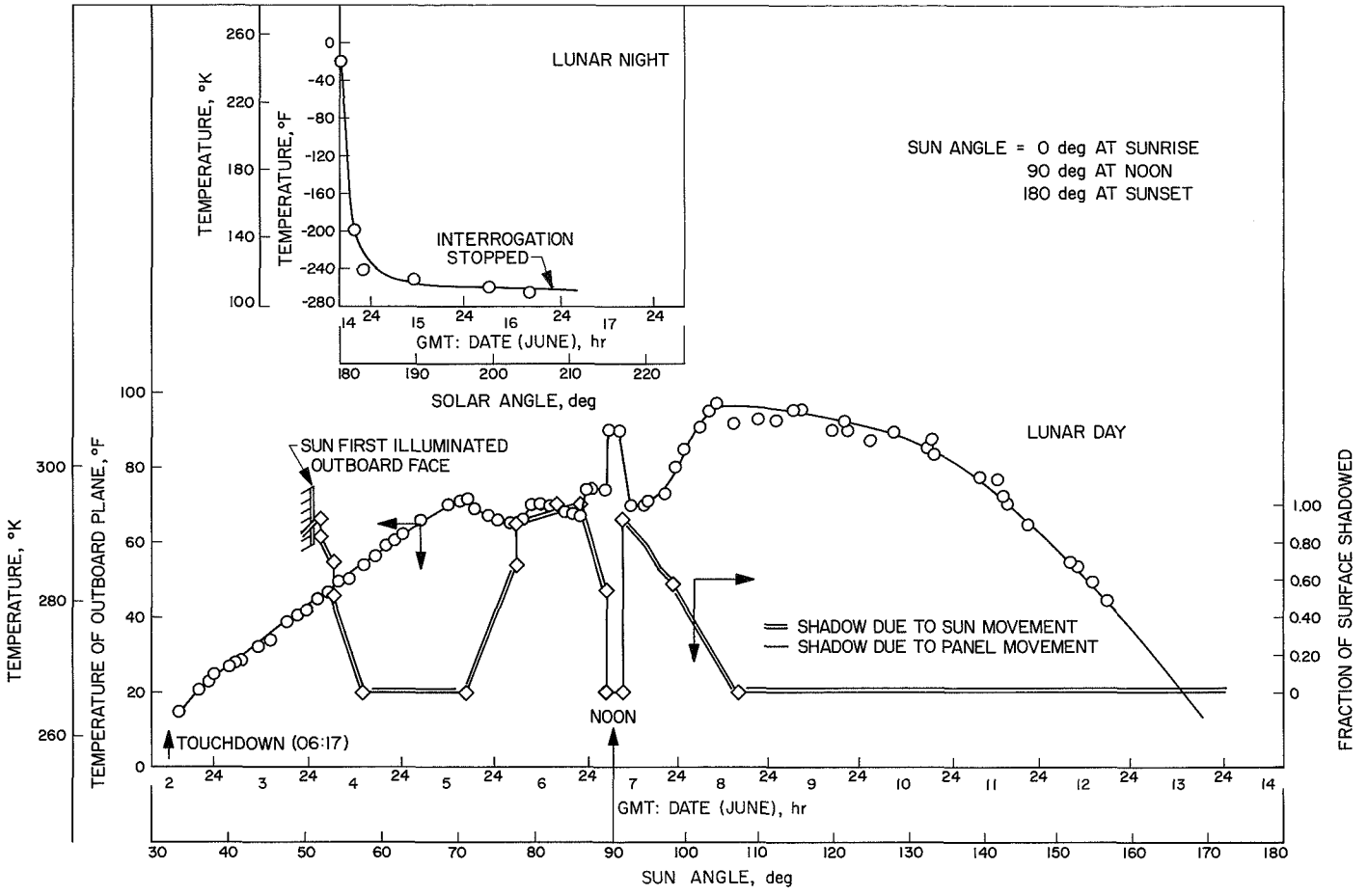

Fig. IV-7. Temperature and shadow of outboard face of compartment A during first lunar day and night

In calculating lunar surface temperatures for the lunar day, it was assumed that $\dot{q} = 0$; for the lunar night, however, the heat flow is allowed from the inside toward the outside of the compartment. Under these conditions, Eq. (3) can be rewritten as:

$$\sigma T_2^4 = \frac{\sigma T_1^4}{\varepsilon_2 F_{12}} - \frac{\alpha_{1S} S}{\varepsilon_1 \varepsilon_2 F_{12}} (F_{12} \rho_2 \sin \phi + \cos \beta) \qquad (4)$$

(for lunar day)

$$\sigma T_2^4 = \frac{\sigma T_1^4}{\varepsilon_2 F_{12}} - \frac{\dot{q}}{\varepsilon_1 \varepsilon_2 F_{12}} \qquad (5)$$

(for lunar night)

The numerical values used in calculations are:

$S = 1352 \pm 27$ w/m²

$\varepsilon_1 = 0.87 \pm 0.02$

$\alpha_{1S} = 0.2 \pm 0.02$

$\sigma = 5.675 \times 10^{-8}$ w/m² °K⁴

$\varepsilon_2 = 1.0$

$\rho_2 = 0.052$ (value assumed for simplicity)

A value $\dot{q}$ was taken as 2.7 ± 0.6 w/m². This value was estimated from cold-wall vacuum chamber tests on a prototype spacecraft.

Figure IV-12 represents the lunar surface brightness temperature as calculated from Eqs. (4) and (5). In this figure, the dashed curve results from a view factor ($F_{12} = 0.314$) that corresponds to an angle of 21° 47′ between the local normal of the lunar surface and the outboard compartment face; the solid curve is for $F_{12} = 0.336$ and corresponds to an angle of 19° 9′. In both cases, the lunar surface is assumed to be an infinite

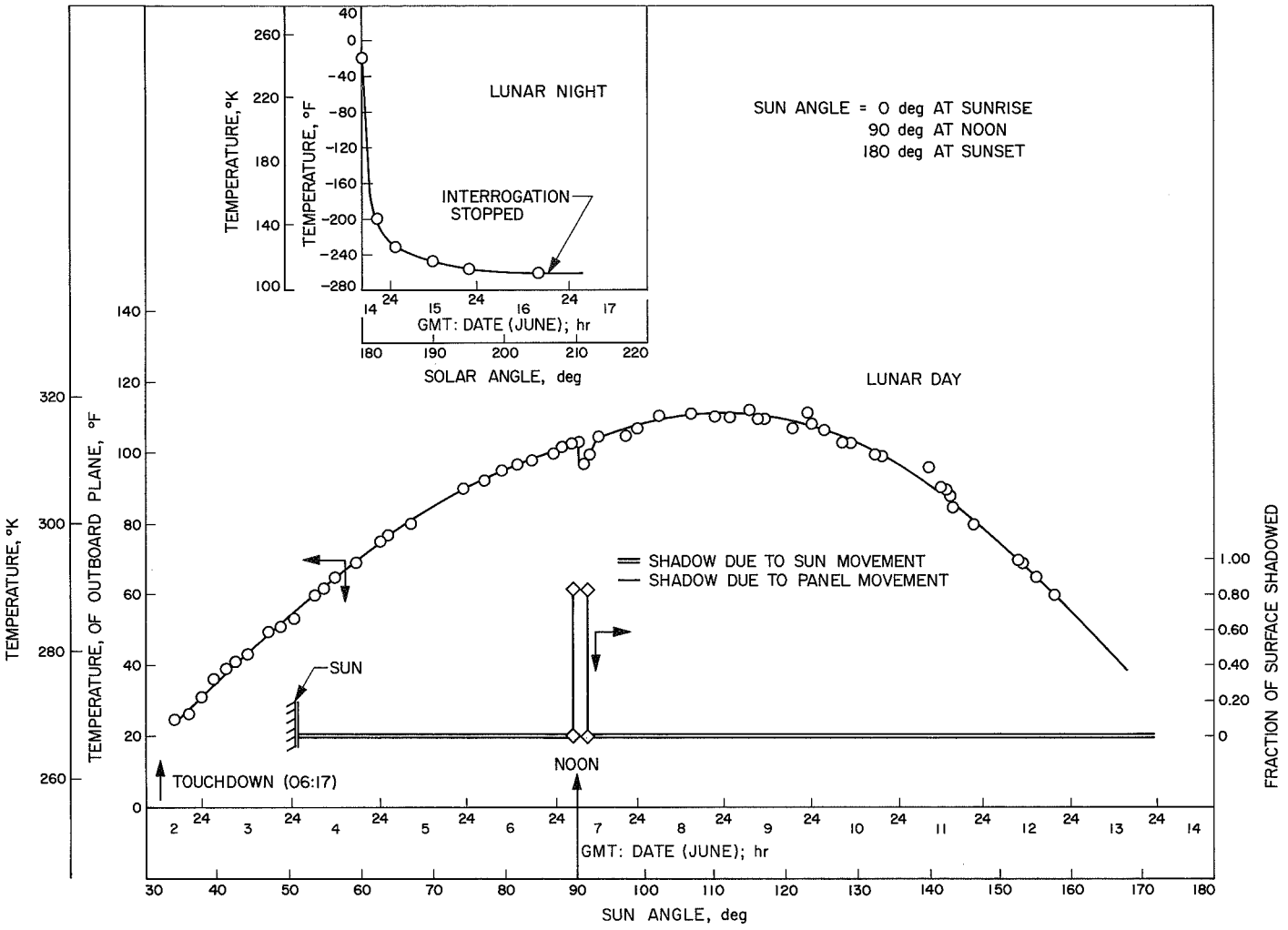

Fig. IV-8. Temperature and shadow of outboard face of compartment B during first lunar day and night

plane. It is seen that rather accurate knowledge of the geometric view factor is desirable to obtain good results.

In view of uncertainties in compartment temperature reading, as well as numerical values used, an error analysis was performed to examine the accuracy of lunar surface temperature calculations by the method described. The results for constant configuration factor $F_{12} = 0.314$ are shown in Fig. IV-13.

D. Comparison of Surveyor I and Earth-Based Lunar Surface Temperatures

The lunar surface brightness temperatures calculated from *Surveyor I* and for $F_{12} = 0.314$ are shown as the dashed curve in Fig. IV-2. There is good agreement near lunar noon and after sunset with the earth-based curve for a value of the thermal parameter between 250 and 1000. This indicates that the lunar surface material adjacent to *Surveyor I* is highly insulating and probably finely granulated.

It is speculated that a major part of the discrepancy during the lunar morning is due to directional thermal emission of the lunar surface.

E. Apparent Lack of Dust on Spacecraft

The question of whether or not any lunar dust was raised at the surface and deposited on the spacecraft is of interest from both the standpoints of scientific and spacecraft operation. If large quantities of dust were raised, it would be noticeable in spacecraft thermal performance because of the resulting increase in thermal finish solar absorptances. The spacecraft thermal behavior

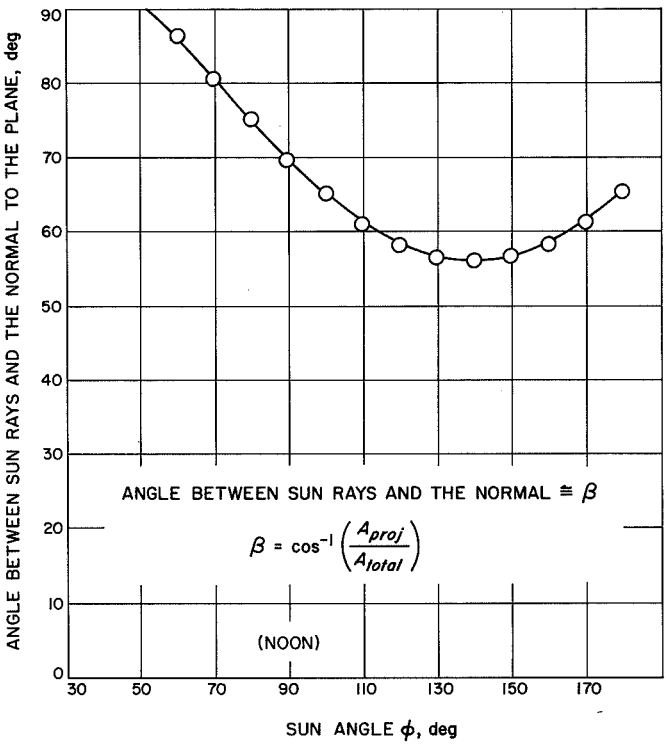

Fig. IV-9. Angle between sun rays and the normal to outboard plane of compartment A during first lunar day

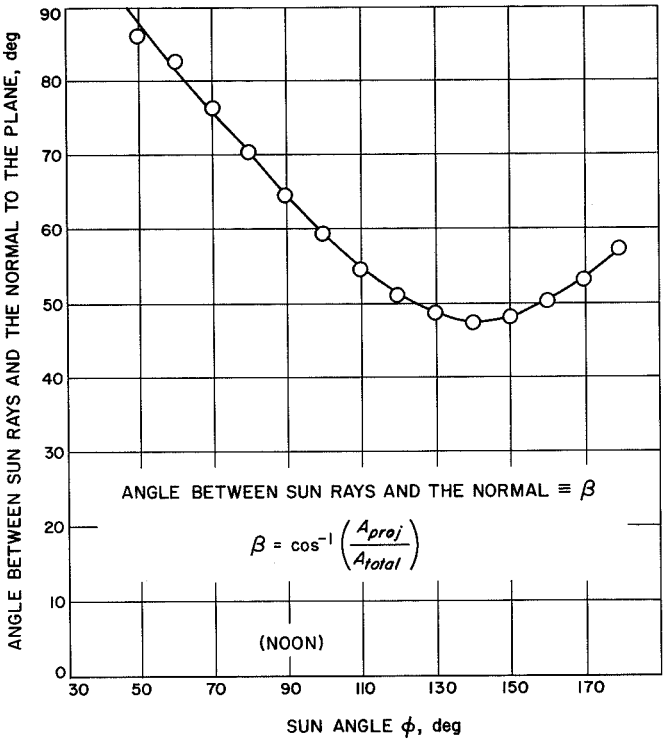

Fig. IV-10. Angle between sun rays and the normal to outboard plane of compartment B during first lunar day

did not indicate any such changes in thermal properties; therefore, it is implied that no significant amount of lunar dust was raised.

TV pictures were taken of the compartment Vycor glass radiators; compartment A is shown in Fig. IV-14(a) and compartment B in Fig. IV-14(b). Both pictures were taken on June 11, 1966, and show what appear to be small particles randomly distributed over the radiators. It is possible that these particles are material deposited on the mirrors by the air conditioner during the period in which the spacecraft was on the launch pad, or by the nose fairing during boost. Samples of the type of particles deposited by the air conditioner were obtained in tests prior to encapsulation of the spacecraft; these particles generally are small fibers rather than particulate matter. At this time, it is not possible to determine whether the particles seen in the pictures are of lunar or earth origin.

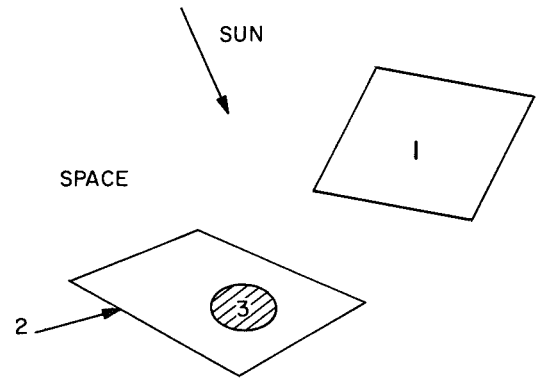

1. COMPARTMENT B OUTBOARD FACE (ASSUMED FLAT)
2. LUNAR SURFACE (INCLUDING SHADOW)
3. SPACECRAFT SHADOW ON LUNAR SURFACE

Fig. IV-11. Thermal balance geometry

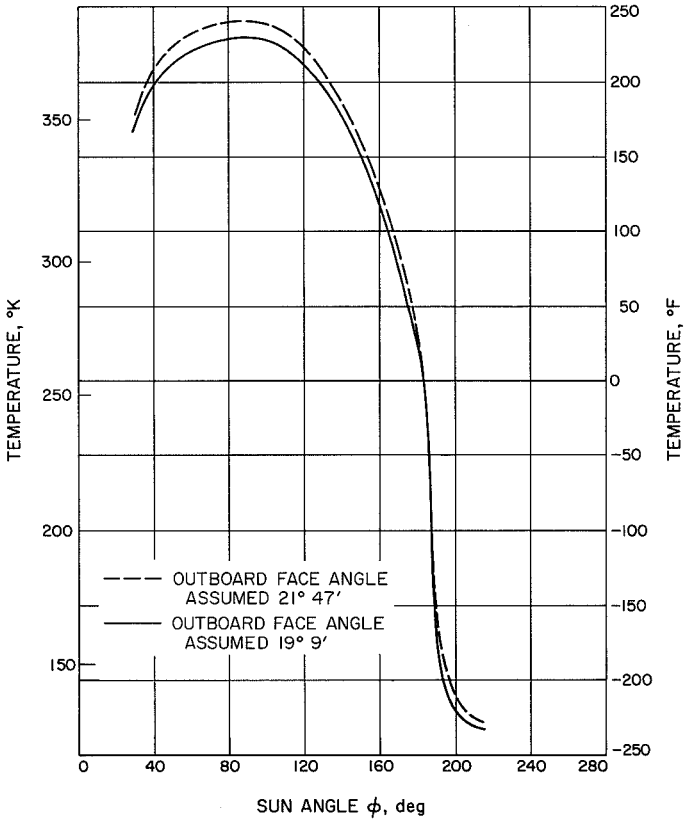

Fig. IV-12. Lunar surface brightness temperature derived from measurements of compartment B sensor

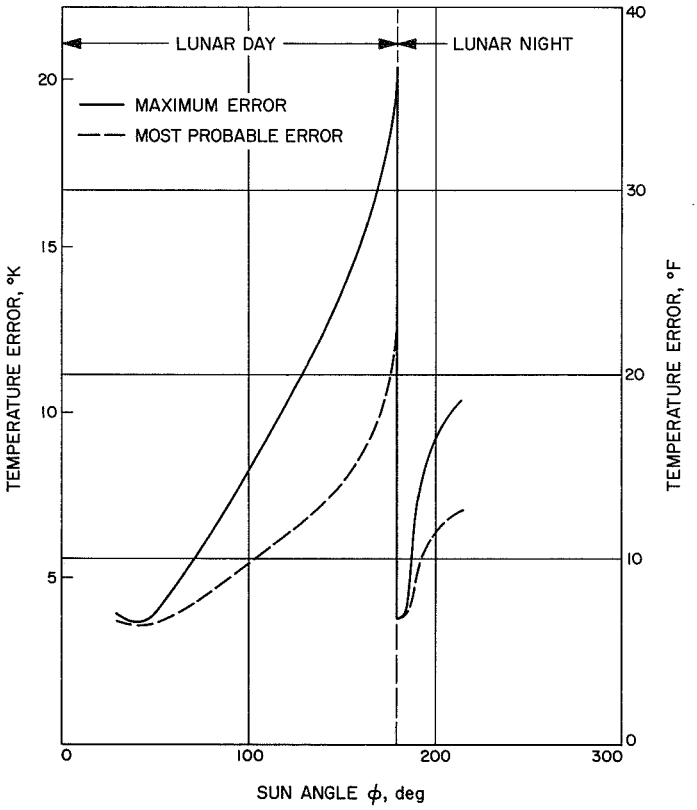

Fig. IV-13. Errors in lunar surface brightness temperature determination based on compartment B data

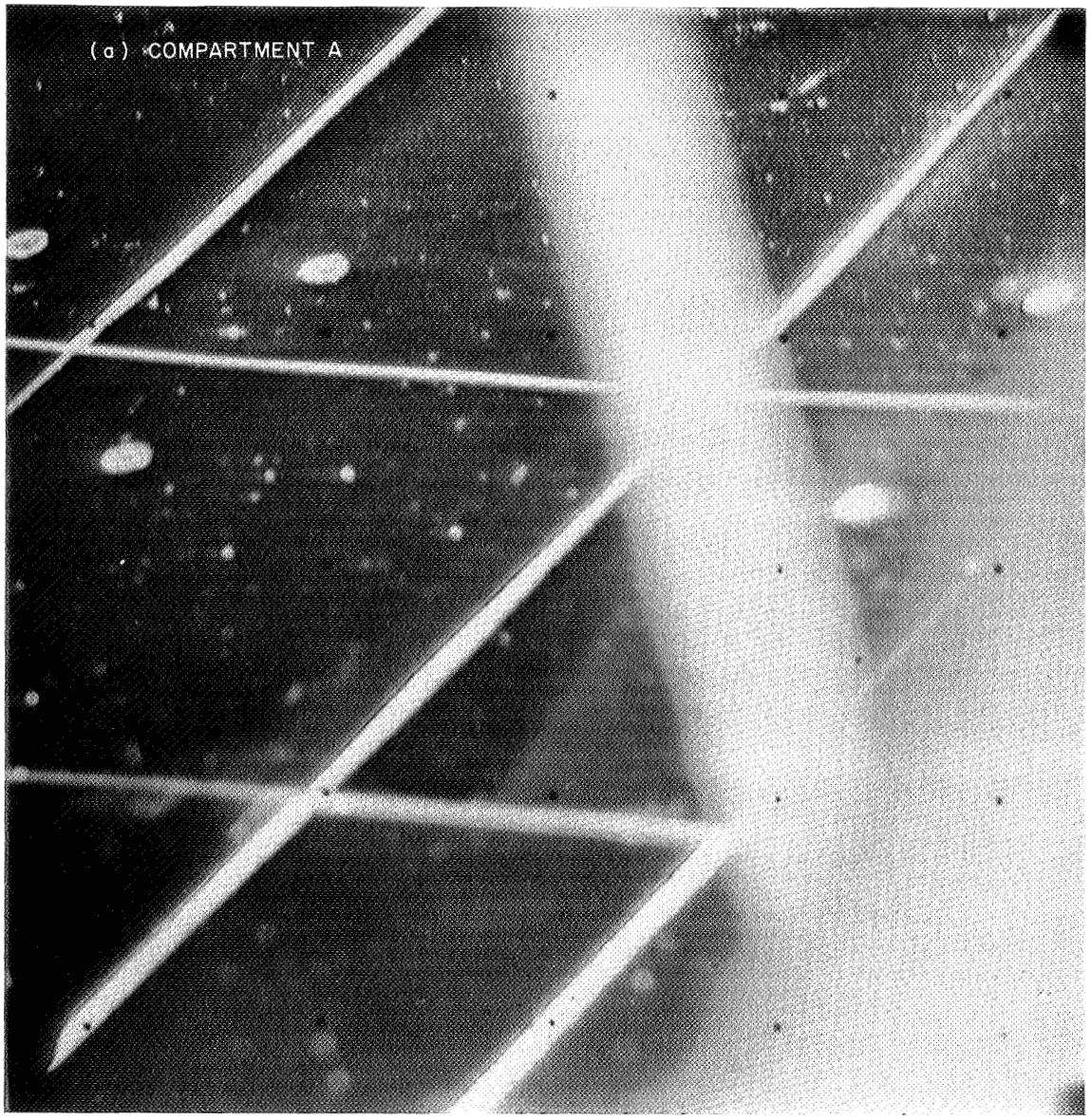

Fig. IV-14. Compartment Vycor glass radiators

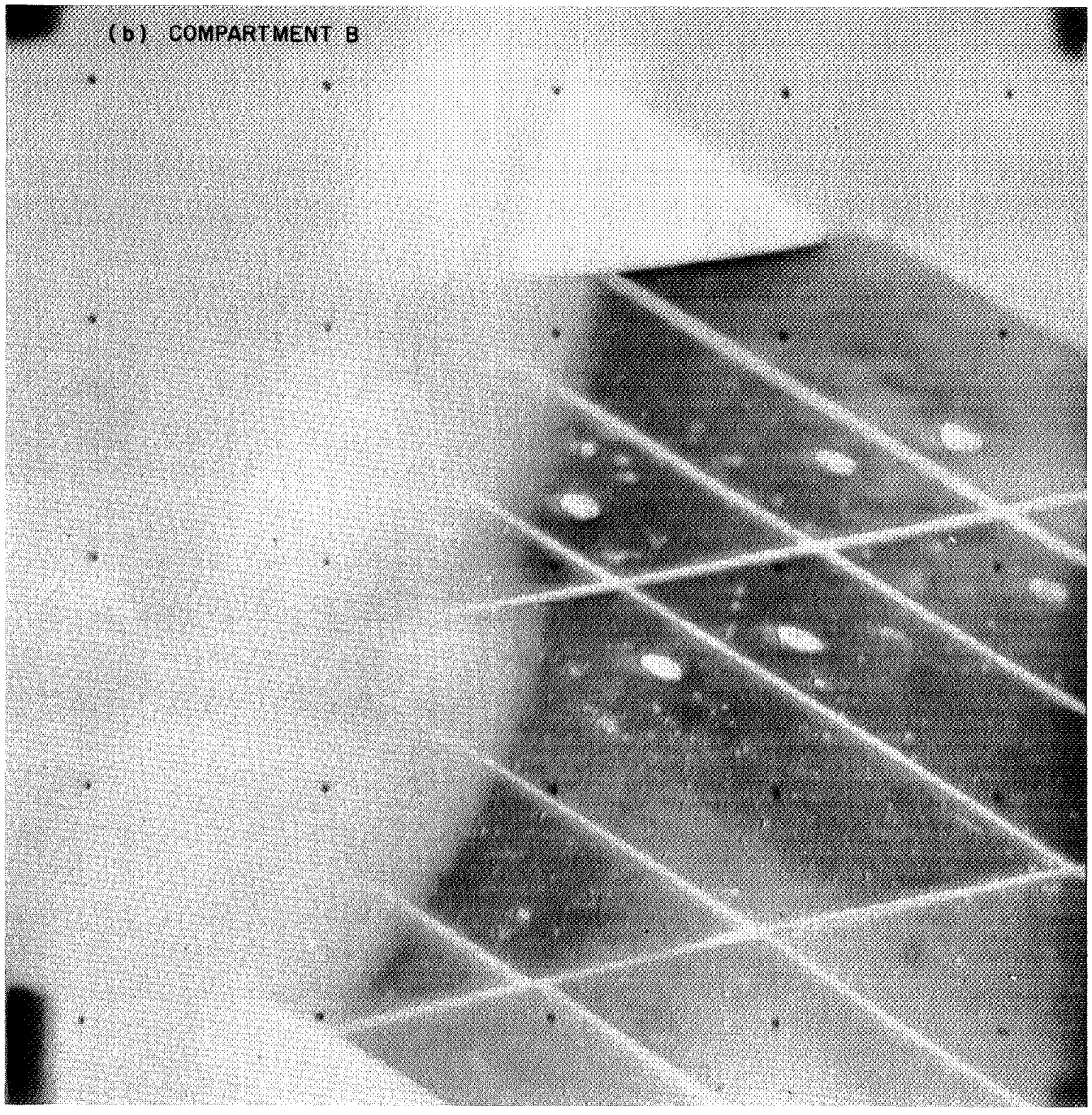

Fig. IV-14. Compartment Vycor glass radiators (cont'd)

REFERENCES

IV-1. Saari, J. M., and Shorthill, R. W., *Isothermal and Isophotic Contours for the Lunar Disk Through a Lunation*, Document D1-82-9552, The Boeing Co., 1966.

IV-2. Sytinskaya, N. N., *Astronomicheskii Zhurnal*, pp. 295–301, 1953.

IV-3. Saari, J. M., and Shorthill, R. W., *Nature*, Vol. 205, p. 964, 1965.

IV-4. Shorthill, R. W., and Saari, J. M., *Science*, Vol. 150, p. 210, 1965.

IV-5. Saari, J. M., and Shorthill, R. W., Document D1-82-0530, The Boeing Co., 1966.

IV-6. Jaeger, J. L., "Surface Temperature of the Moon," *Australian Journal of Physics*, Vol. 6, p. 10, 1952.

ACKNOWLEDGMENT

Thanks are extended to H. Knudsen of Hughes Aircraft Company for spacecraft data description and to W. Jaworski for the data analysis.

V. LUNAR SURFACE ELECTRICAL PROPERTIES

W. E. Brown

Two radar systems were used on *Surveyor I* in order to perform various engineering functions during the touchdown sequence: altitude marking radar (AMR), which provided data at ranges of from approximately 350 to 75 km, and the radar altimeter doppler velocity sensor (RADVS) radar, which provided data from 11 km to touchdown. The various radar parameters are summarized in Table V-1. During the radar operation, signal strength was telemetered; it was hoped that these data could be converted to effective radar cross sections so that information of scientific value could be extracted. This work was not completed in time for this writing; therefore, a preliminary and partial analysis of the available data is presented here which, in general, represents the status of the data reduction.

Table V-1. Summary of Surveyor radar parameters

Parameter	Altitude marking radar	Range radar	Doppler radar (three beams)
Frequency, Mc	9,300	12,900	13,300
Wavelength, cm	3.22	2.32	2.25
Pulse width, μsec	3.2	Continuous wave	Continuous wave
Power radiated, dbm	62.5	25	33.5, 31.9, 33.4
Pulse recurrence frequency, pulses/sec	350	—	—
Antenna gain, db	36.3	29.2	28, 28, 28.6
Off normal angle, deg	6	0	25
Telemetry bandwidth, cps	$\simeq$2	$\simeq$2	$\simeq$2
Sampling rate/sec	1	1	1
Below 6 km	—	2	2
Gain states	1	3	3
IF bandwidth, kc	—	10	10

A. Altitude Marking Radar

The AMR signal strength measurements are a strong function of the duration of the echo as seen by the radar receiver. The calibration curves available provide for two echo widths: 3 and 10 μsec. In order to establish a reference for future analysis, a first estimate of the radar cross section was calculated using the parameters given in Table V-1 and altitudes based upon a constant velocity of 2.7 km/sec with an event mark at 95 km. The result is shown in Fig. V-1. The relatively high value for this estimate, as well as the gradual falloff toward the lower altitudes, indicates that the echo duration was > 3 μsec and was not beamwidth-limited. It may be possible to estimate the echo duration more accurately and extract the range dependence in order to provide a better estimate of the effective radar cross section. Radar cross section is defined as the ratio of the effective radar target area to the geometric target area.

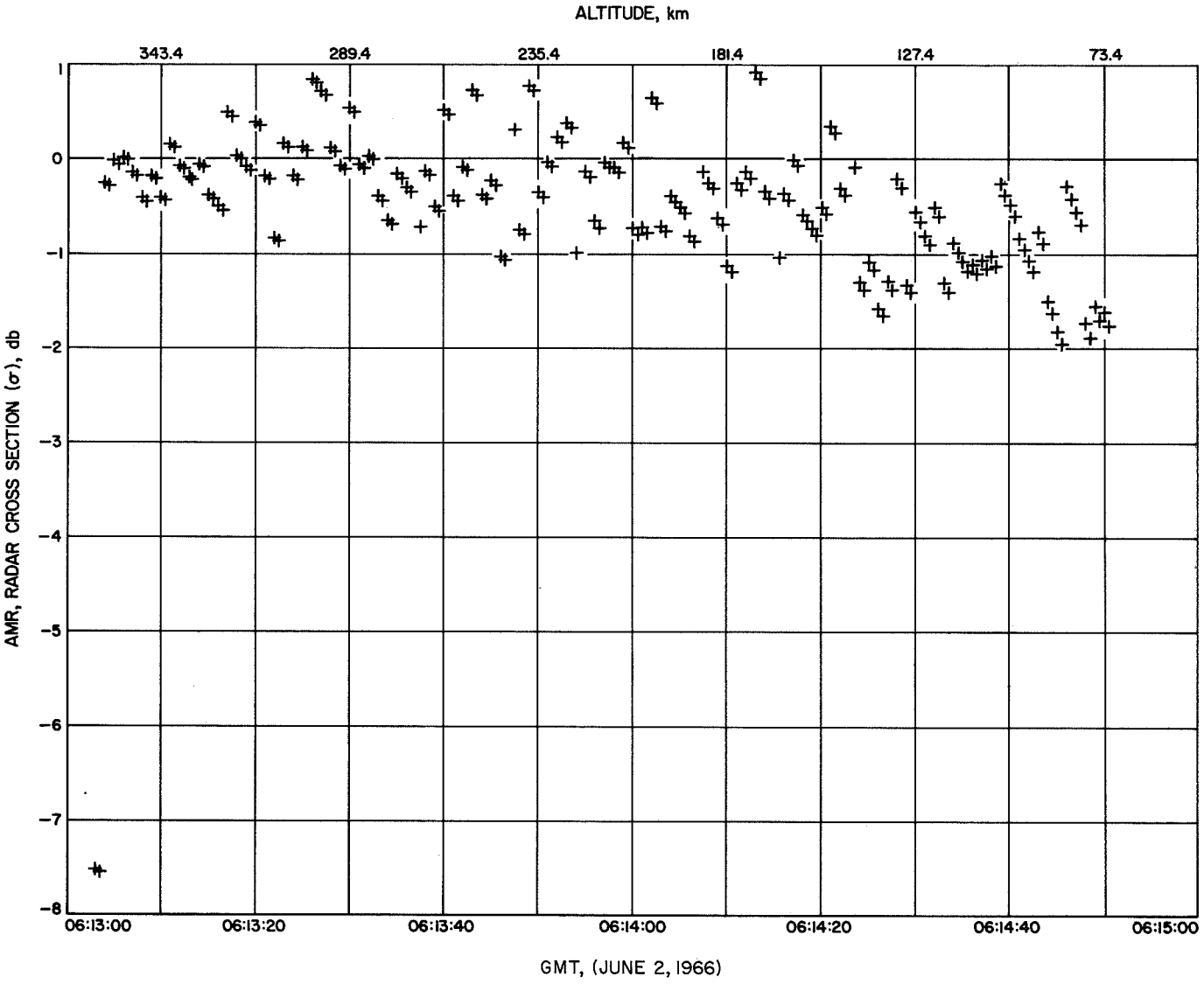

Fig. V-1. Radar cross section from AMR

B. Radar Altimeter and Doppler Velocity Sensor Radar

1. Doppler

The RADVS radar has four antenna beams; three of these beams were 25° off normal, and one was vertical. The performance of the radar was such that it is convenient to consider the two separately; thus, the RADVS radar is divided into two parts for this report. Beams 1, 2, and 3 were approximately oriented to the southwest, northwest, and northeast, respectively, in lunar coordinates. Each beam traced a path of 5500 m in length across the lunar surface.

Values for radar cross section were computed from each of the telemetered data points by using existing calibration equations, and range and velocity points that were derived and telemetered from the RADVS system. The existing calibration equations are based upon an unmodulated signal. The actual echo, however, is modulated by the scintillation effect. Since the relation between input power and output signal strength voltage is more logarithmic than linear for this radar, the averaging that takes place on the spacecraft before telemetry would introduce a sizable error in the determination of the average signal strength. Therefore, the radar cross-section curves shown in Figs. V-2 through V-4 represent a first estimate, and do not include any attempt to correct for weighted integration. The numbers indicate the gain state; the actual points are located at the place where a decimal point would occur just before the number. At, or adjacent to, gain state changes, the value of radar cross section is incorrect and represents a transition point between two voltages.

It can be noted in the beam 1 record that the relative radar cross section increased for a period of approximately 25 sec, which corresponds to ranges of 2500 to 1200 m along the surface from the *Surveyor* touchdown location. The general nature of the behavior suggests that the beam passed over a crater at this time.

2. Range

The vertical beam of the RADVS system apparently had a wider range of signal amplitude fluctuation, which was expected as a consequence of scintillation from specular-like reflections. The radar cross section shown in Fig. V-5 indicates a gap between gain 3 and gain 2. This gap may well be the result of the mentioned weighted integral effect. In all cases, the absolute values of radar cross section are not to be taken as factual; they represent estimates only and could be in error by several decibels, particularly in Figs. V-1 and V-5.

C. Conclusions

(1) Radar cross-section values are approximately as expected from earth-based measurements.

(2) Echo was returned by the visible surface or within 30 to 60 cm of the surface.

(3) Plumes of the vernier engines had no measurable effect upon the radar signal strength.

(4) One of the off-normal beams traversed a crater-like surface anomaly approximately 1 km wide and 2 km southwest of the touchdown point.

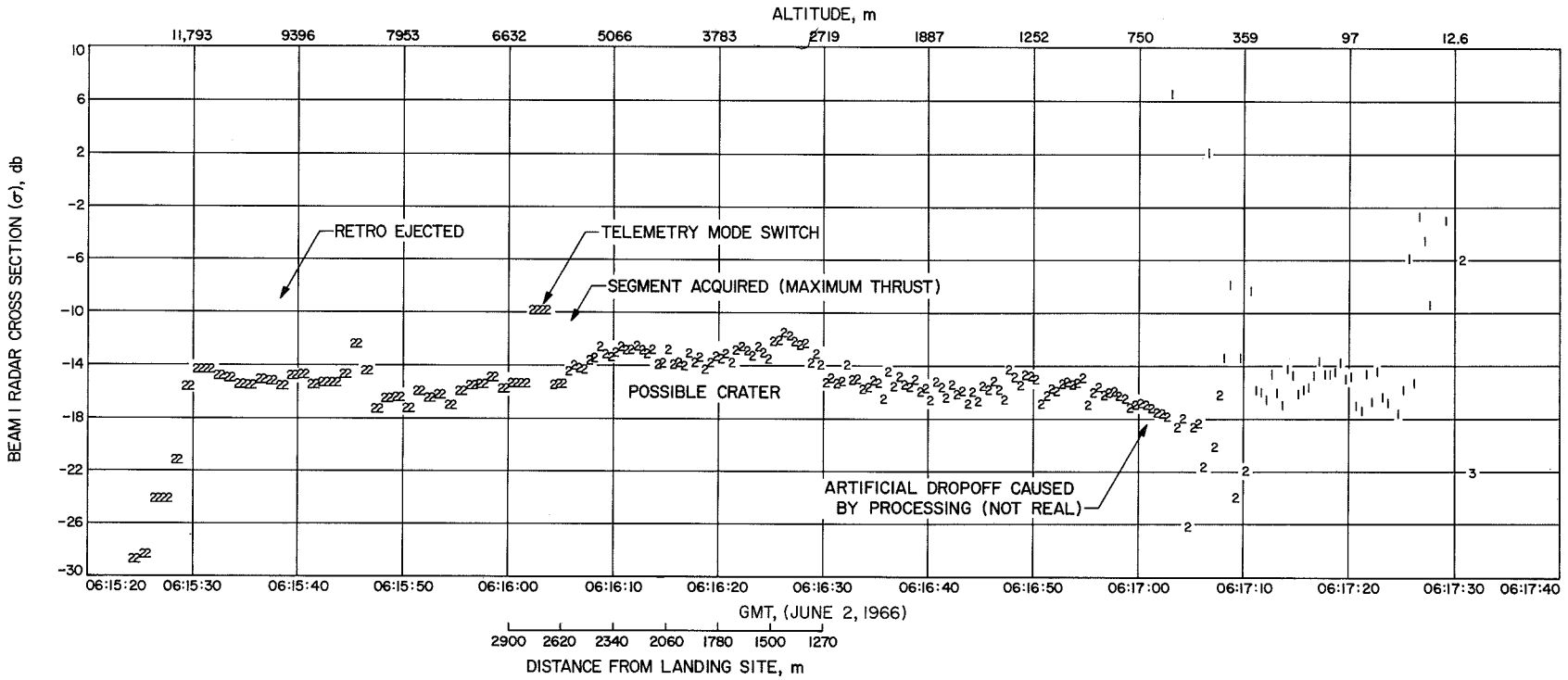

Fig. V-2. Beam 1 radar cross section

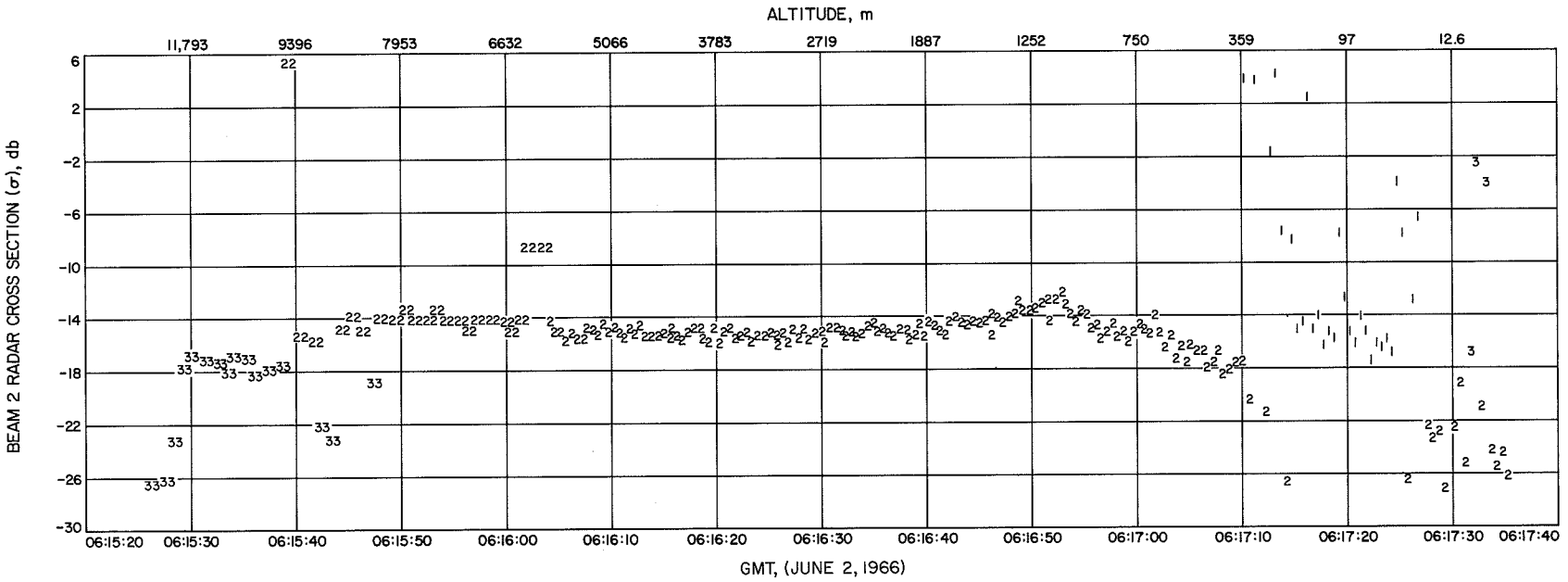

Fig. V-3. Beam 2 radar cross section

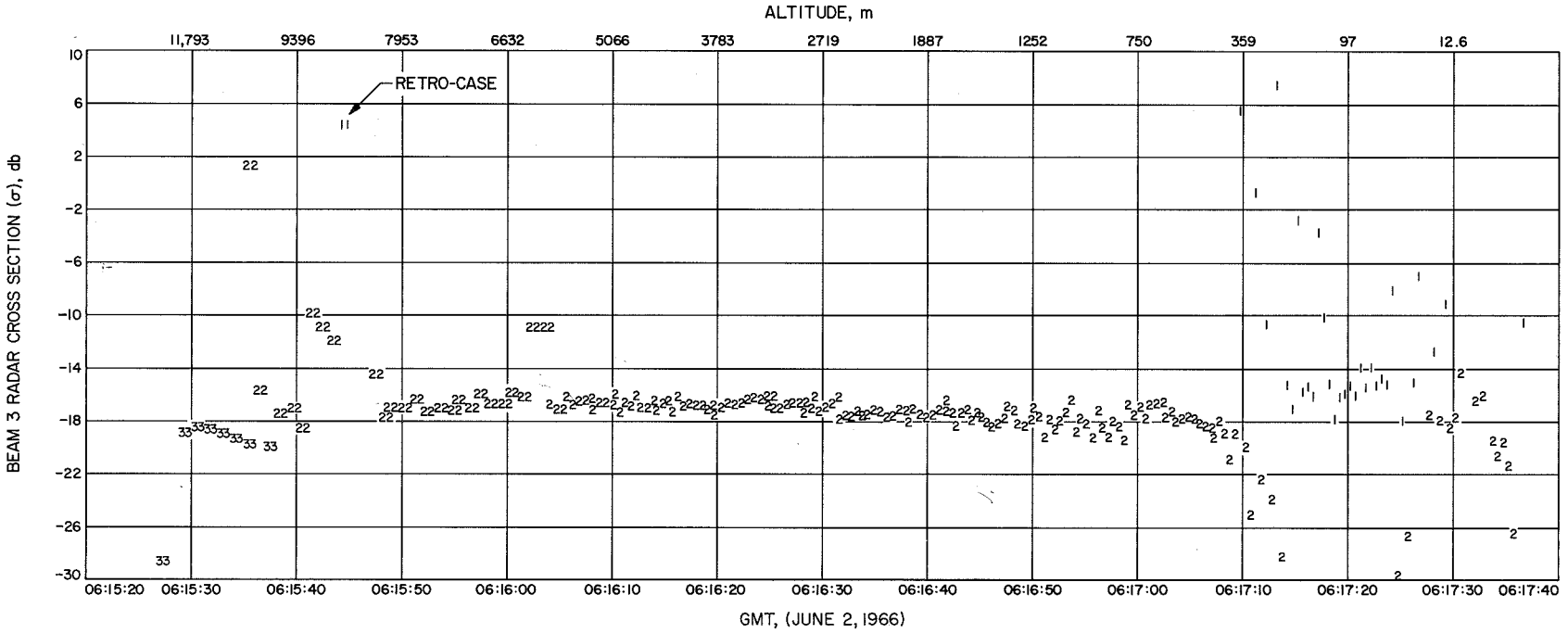

Fig. V-4. Beam 3 radar cross section

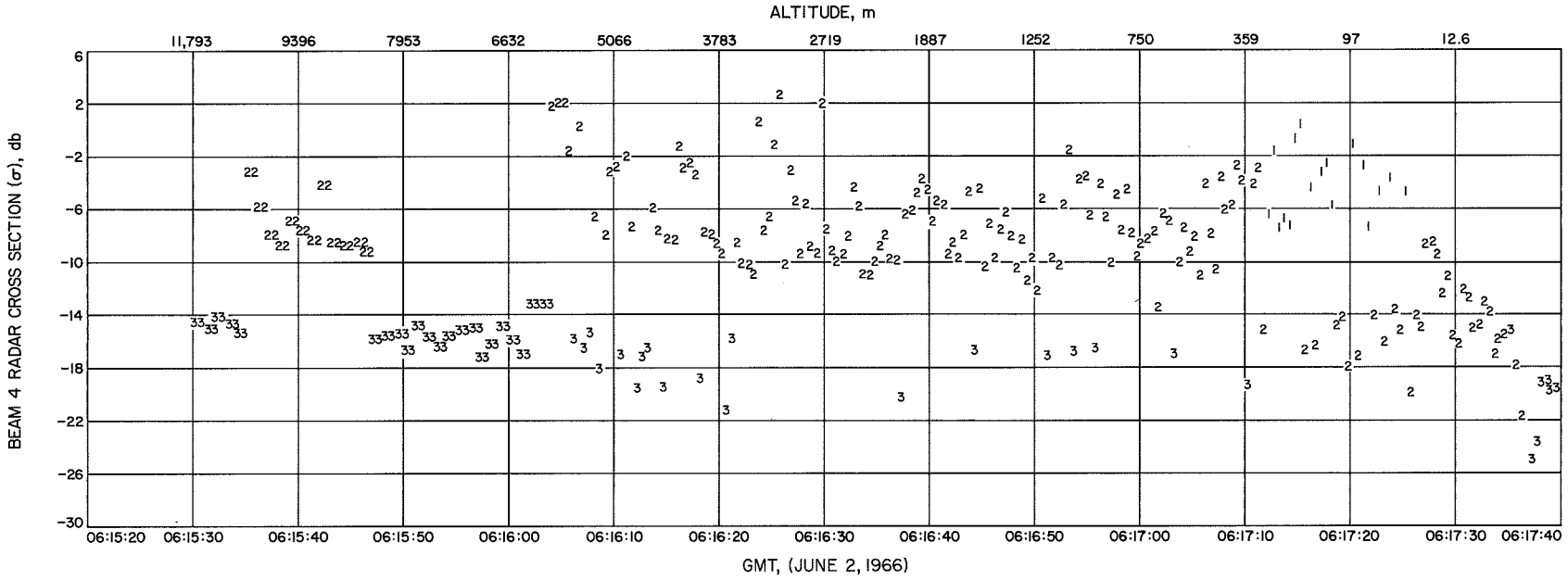

Fig. V-5. Beam 4 (vertical) radar cross section

VI. LUNAR SURFACE MECHANICAL PROPERTIES

E. M. Christensen, S. A. Batterson, H. E. Benson, C. E. Chandler,
R. H. Jones, R. F. Scott, E. N. Shipley,
F. B. Sperling, and G. H. Sutton

A. Observations and Explanations

The interpretation of the lunar surface properties discussed here is based on: (1) pictures that show the lunar surface area disturbed by the footpads and the crushable blocks and (2) histories of axial loads in the shock absorber on each of the three legs during the landing (Fig. VI-1). The dimensions of the landing gear assembly are shown in Fig. VI-2 and further discussed in Ref. VI-1; their motions during landing are shown schematically in Fig. VI-3. The spacecraft landed at a vertical velocity of approximately 3.6 m/sec (11.6 ft/sec) with probably less than 0.3-m/sec (1-ft/sec) horizontal velocity. At touchdown, the angle between the plane of the three footpads and the local lunar surface was approximately 1.2°. At rest on the surface, the spacecraft frame is now estimated to be parallel to the local lunar surface (dimensions of spacecraft) within 1°.

Figure VI-4 shows the time records of the axial load, as measured by a strain gage, on each shock absorber. (Computer-simulated landing data for landing on a hard surface are presented in Fig. VI-5.) It can be seen that surface contact for all three footpads was almost simultaneous, indicating that the spacecraft mast (Fig. VI-1) at touchdown was approximately normal to the surface. The footpads impacted at intervals of approximately 0.01 sec. Footpad 2 touched first, followed by footpad 1 and then footpad 3.

The record also shows that, following the primary impact, the spacecraft rebounded clear of the surface (approximately 500 msec after initial touchdown) with a secondary impact occurring approximately 1.0 sec after the initial impact, thus indicating that the footpads rebounded about 6 cm (2.5 in.) from the surface. The second impact developed maximum loads equal to approximately one-quarter of the maximum loads developed during initial impact. The maximum vertical load applied to a footpad by the lunar surface material during initial impact was approximately 230×10^6 dynes (approximately 500 lb), determined by analysis. Conversion of this load into a dynamic pressure applied to the surface depends on the footpad area in contact with the soil at the instant the load is measured. Since the lower portion of the footpad is a truncated cone (Fig. VI-2), this contact area depends primarily on the penetration depth; thus, a maximum loading of between 4×10^5 and 7×10^5 dynes/cm^2 (6 and 10 psi) was applied to the surface during the dynamic stages of the impact. The static load required to support the spacecraft on the three landing pads is approximately 3×10^4 dynes/cm^2 (0.5 psi). The earth weight of the spacecraft at the time of landing was 643 lb; its mass was 20.0 slugs (292 kg).

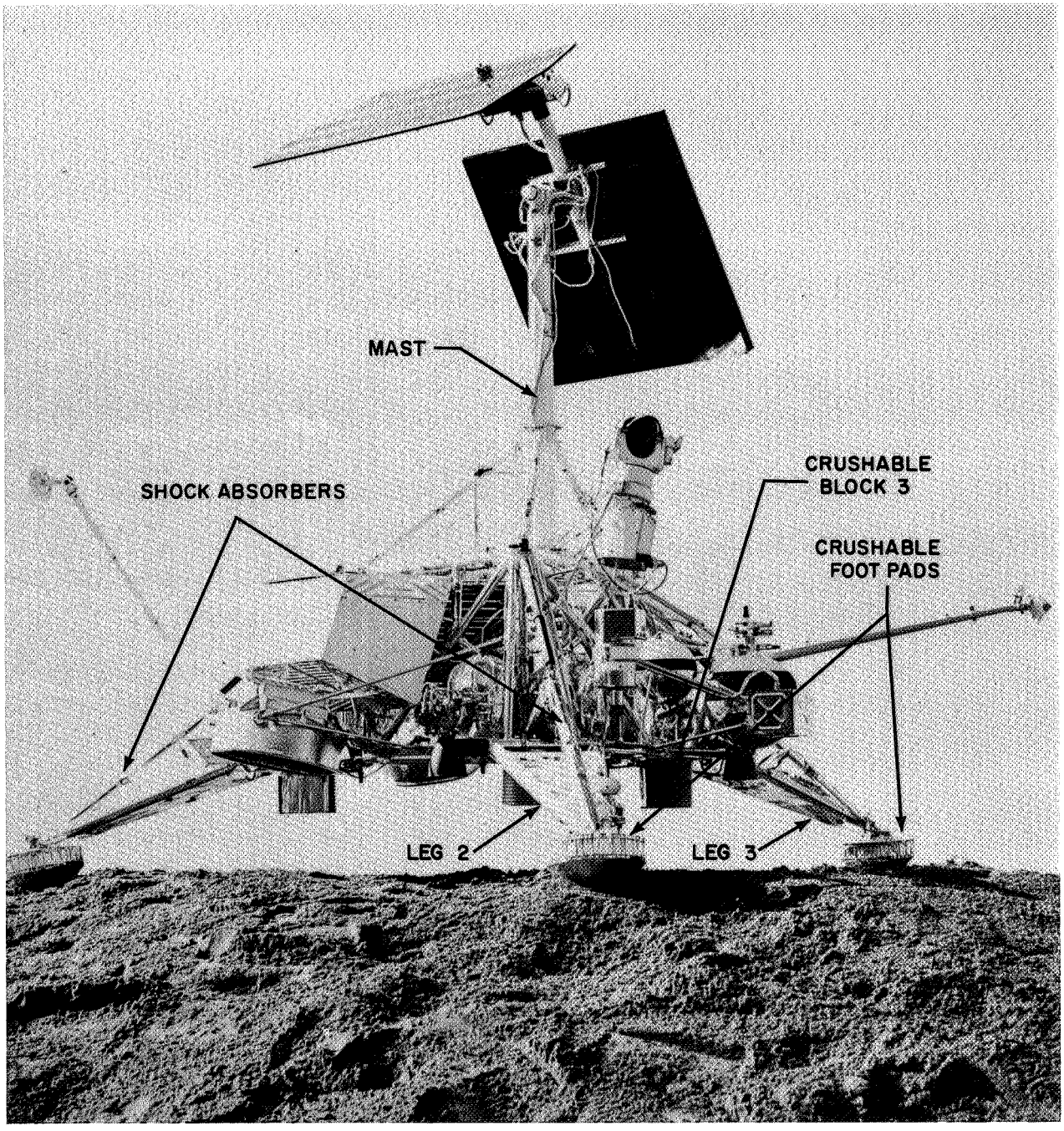

Fig. VI-1. *Surveyor spacecraft*

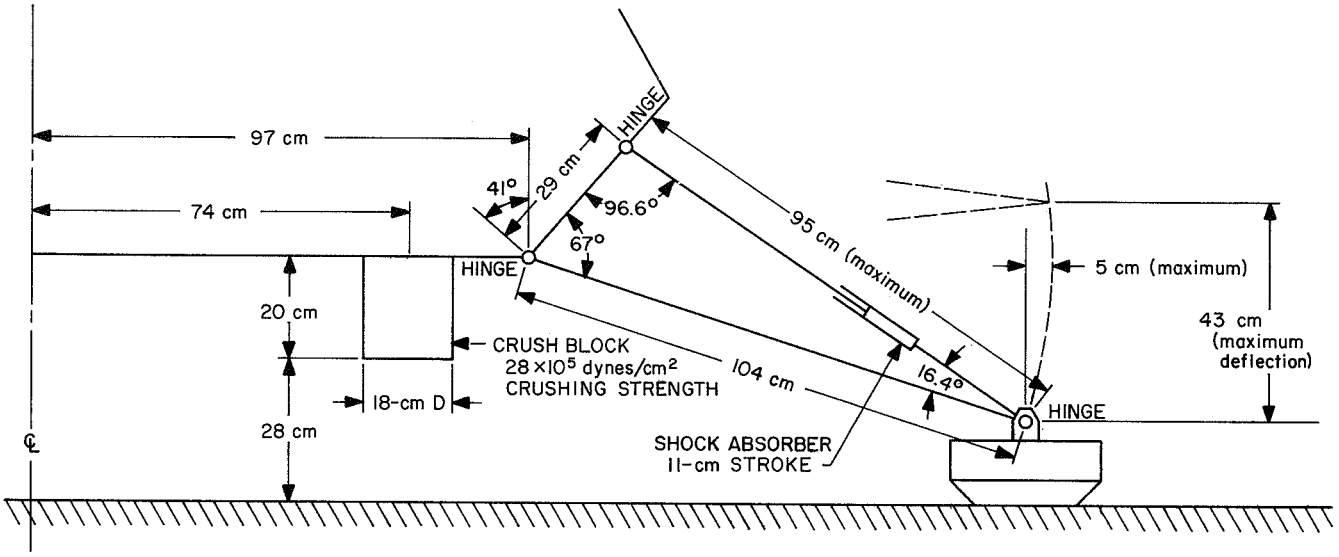

FOOTPAD DETAIL

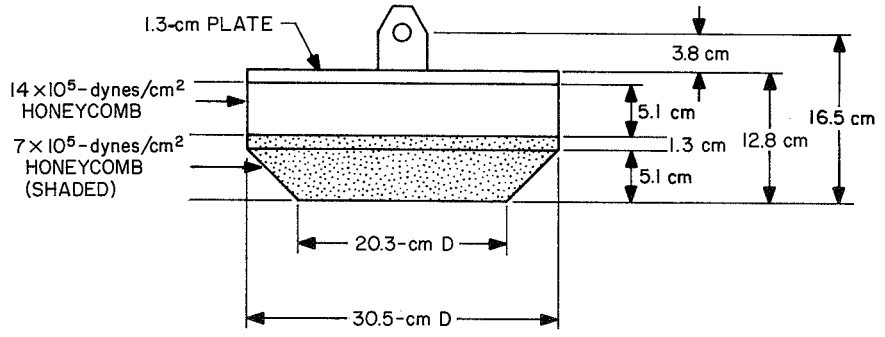

Fig. VI-2. Dimensions of landing gear assembly

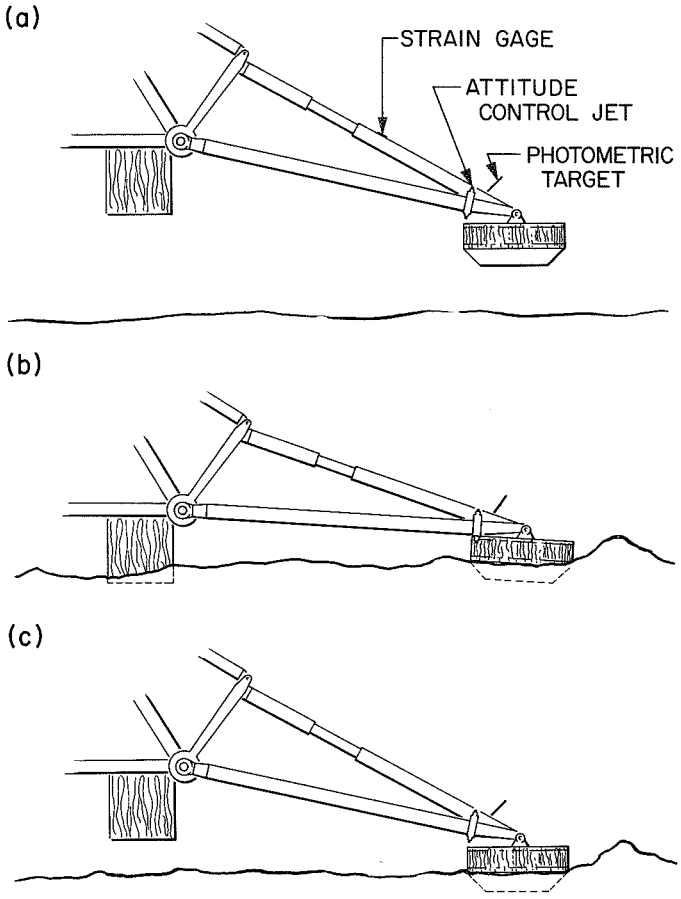

Fig. VI-3. *Surveyor* landing leg assembly, showing articulation in events during landing. [Assembly is shown fully extended in (a); during landing, the shock absorber compresses and the footpad moves up and away from the spaceframe, as shown in (b); assembly is shown re-extended after landing in (c).]

Oscillations of the forces in all the shock absorbers are seen to follow the second impact (Fig. VI-4) with a maximum peak-to-peak amplitude of several hundred pounds and a frequency near 7 cps. The oscillations are in phase and of about equal amplitude (maximum amplitude displacement of spacecraft center of gravity is approximately 0.2 cm), thus indicating a rectilinear vertical mode. The frequency of the oscillations is related to the elasticity of the spacecraft structure and the lunar surface material. Consequently, for frequencies appreciably lower than 7 cps, the spacecraft is well coupled to the moon. This observation is important for a lunar seismograph experiment, in which the seismographic sensor is mounted rigidly to the spacecraft frame, since it permits one to expect reliable recording of seismographic signals with frequencies below 7 cps. Higher-frequency signals would be attenuated, with the possible exception of certain discrete resonant frequencies.

The appearance of the disturbed lunar surface near footpad 2 (Fig. III-1 of this part of this Technical Report) and footpad 3 (Fig. VI-6) indicates a similar behavior of the material displaced by the two footpads. They appear to have landed in a granular material, to have extended laterally approximately 5 cm (2 in.) during impact (as shown in Figs. VI-2 and VI-3), forcing the surface material away, and then to have drawn back to their final position. Footpad 1 is not visible to the TV camera. (To better understand the spacecraft shadow progressions during the lunar day, see Fig. IV-4 of Ref. VI-1.)

At footpads 2 and 3, there is a throwout pattern over the surface (Figs. III-1 and VI-6), including rays of apparently fine-grained material, to a distance of 0.5 to 0.8 m (1.5 to 2.5 ft) from the edge of the footpad. Nearer the footpad, the lunar material was displaced to form a raised rim. The sides of the depression and the rim have a chunky or blocky appearance (Figs. VI-7 and VI-8); the blocks or clumps of material are irregular, have a range of sizes, and appear to consist of aggregates of fine-grained material, rather than of individual stones or pebbles. The basic grain size seems to be below the limit of resolution of the narrow-angle pictures in the 600-line mode, about 0.5 mm (0.02 in.) at the distance of footpad 2. Footpad 2 movements during landing caused some small deformations of the surface adjacent to the footpad on the side nearest the camera (Fig. VI-9). The deformations resulted in an irregular pattern of cracks or fissures at the surface of the material.

Very late in the second lunar day, a good picture of the top of footpad 2 was obtained (Fig. VI-10) with the sun 6° above the horizon. It is interesting to note the texture on the top of the footpad, which also is observable on other pictures of footpad 2 taken within hours of Fig. VI-10. The reason for the texture is unknown, but two possibilities are a texture in the paint or a layer of fine lunar material. However, if it were lunar material of sufficient thickness to be visible, it should have been observed earlier when the camera clearly photographed the adjacent lunar material. Under bright light conditions, the uncovered white paint on the top of the light pad will saturate the camera, and thereby obscure the true nature of the surface. There was no known event that could have deposited the material during the 5-wk period preceding the picture shown in Fig. VI-10.

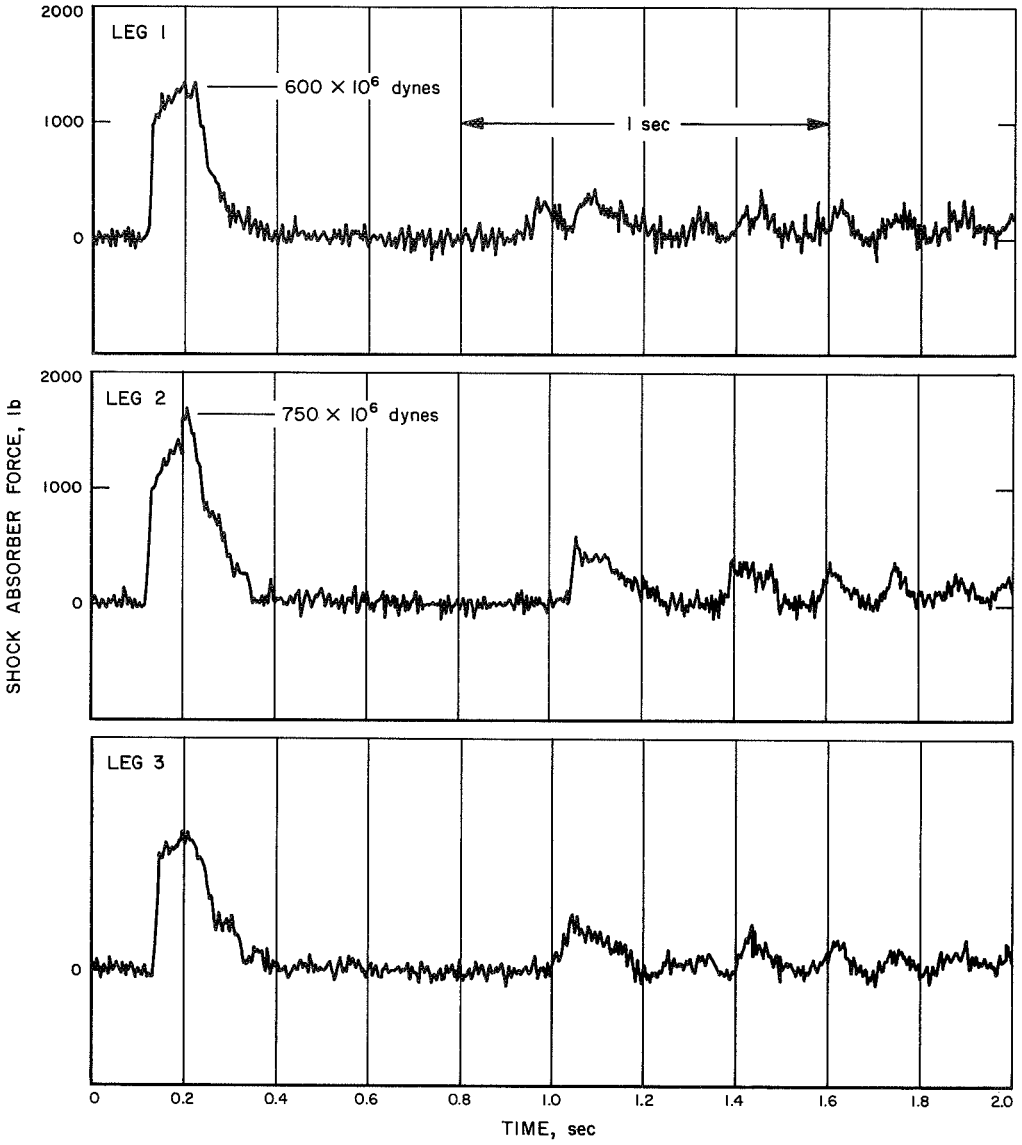

Fig. VI-4. Axial shock absorber strain gage data. (Maximum force developed by shock absorber 3 is not shown because of uncertainties in No. 3 strain gage calibration.)

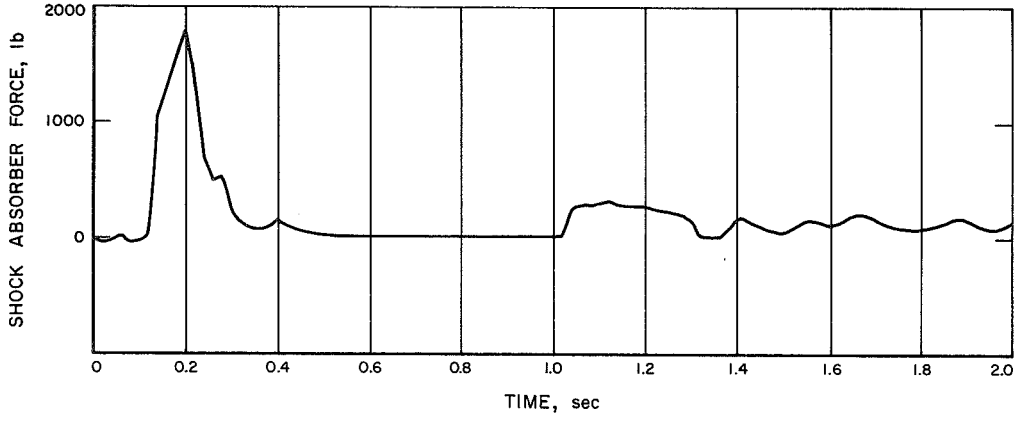

Fig. VI-5. Computer-simulated axial shock absorber strain gage data for landing on a hard surface

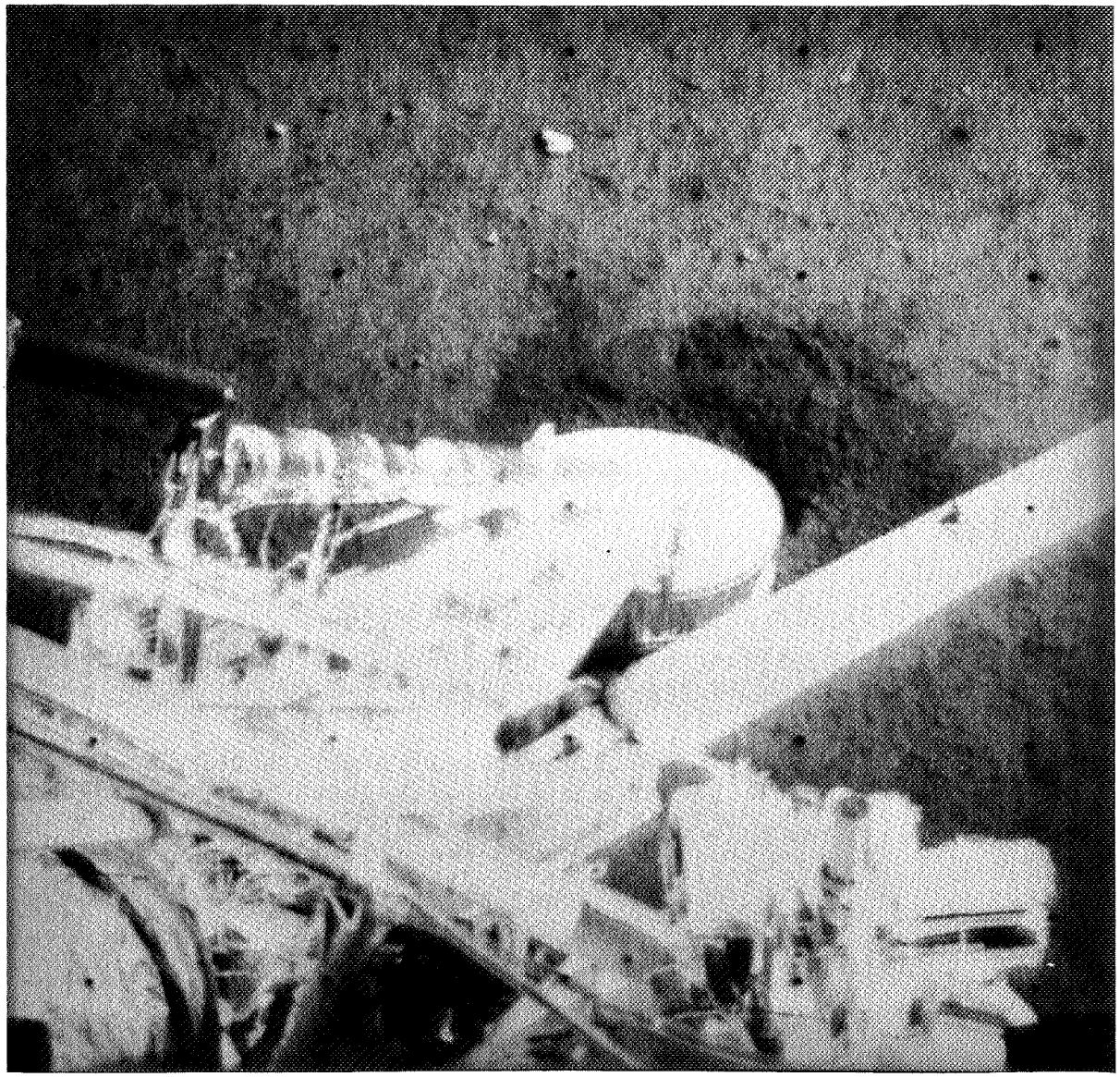

Fig. VI-6. Wide-angle picture of footpad 3 (Note similarity of throwout material to material shown in Fig. III-1.)

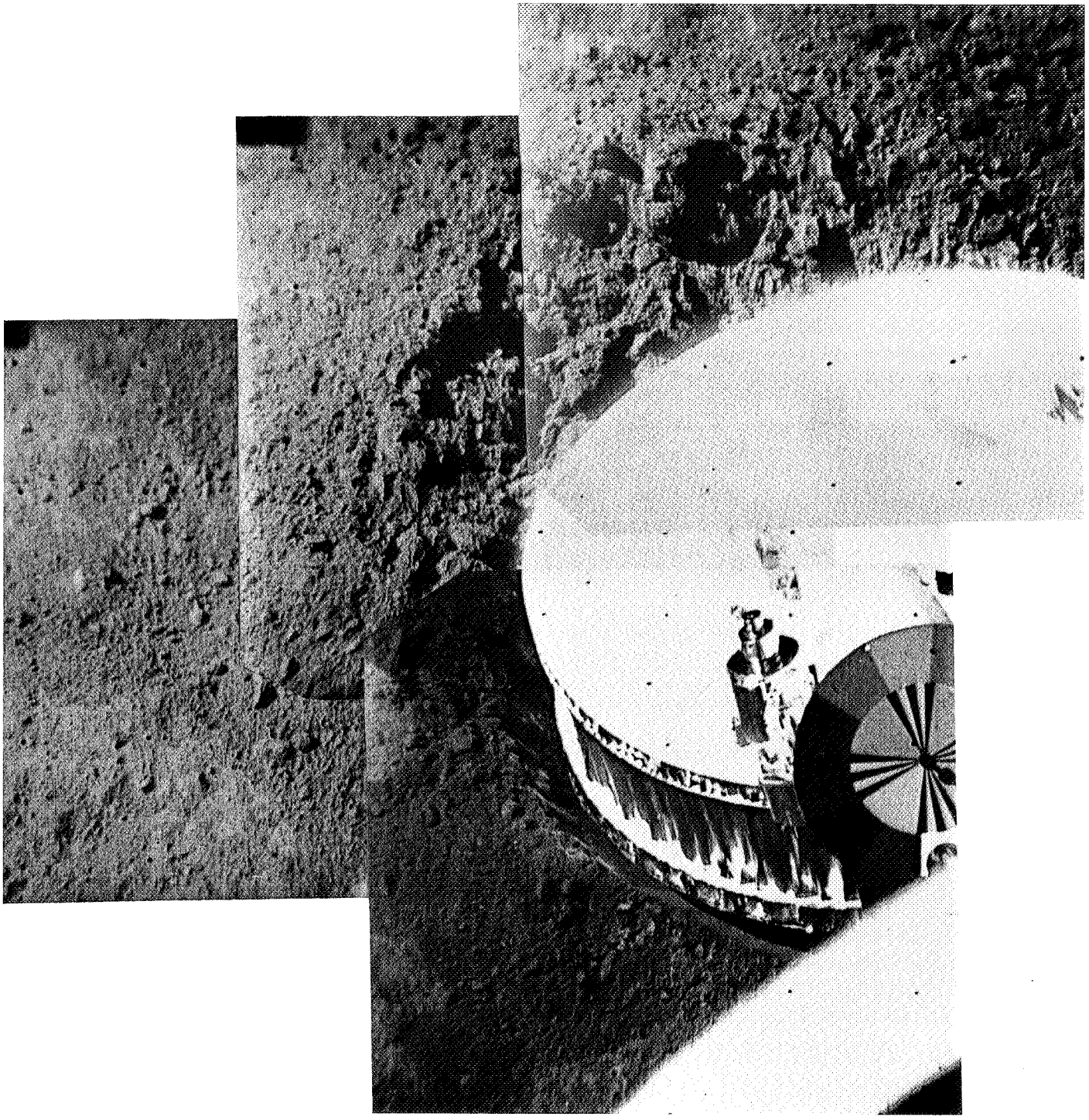

Fig. VI-7. Mosaic of computer-processed narrow-angle pictures of footpad 2 area taken on June 4, 1966. (Sun angle is 54°.)

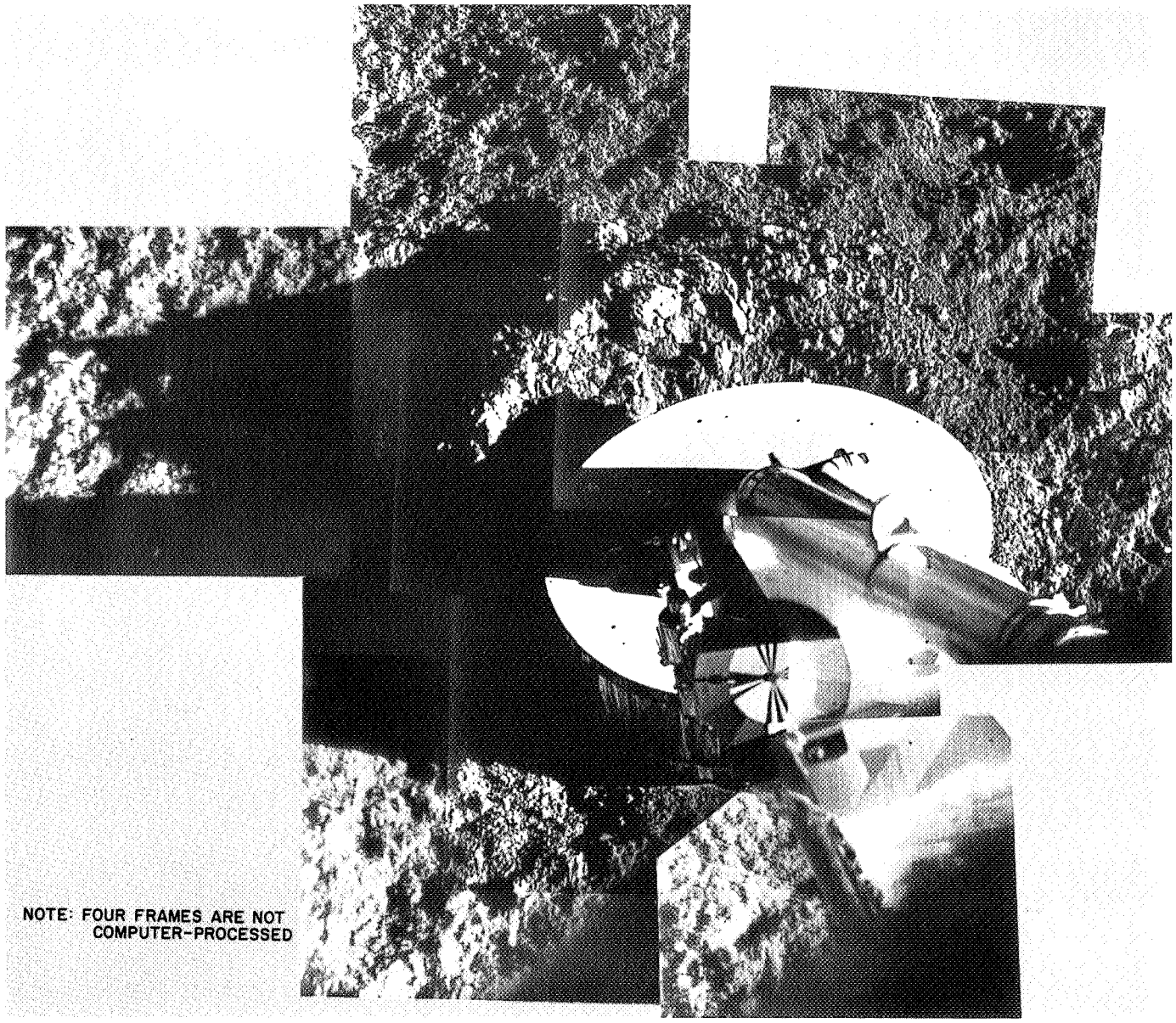

Fig. VI-8. Mosaic of computer-processed narrow-angle pictures of footpad 2 area taken on June 13, 1966. (Sun angle is 10°.)

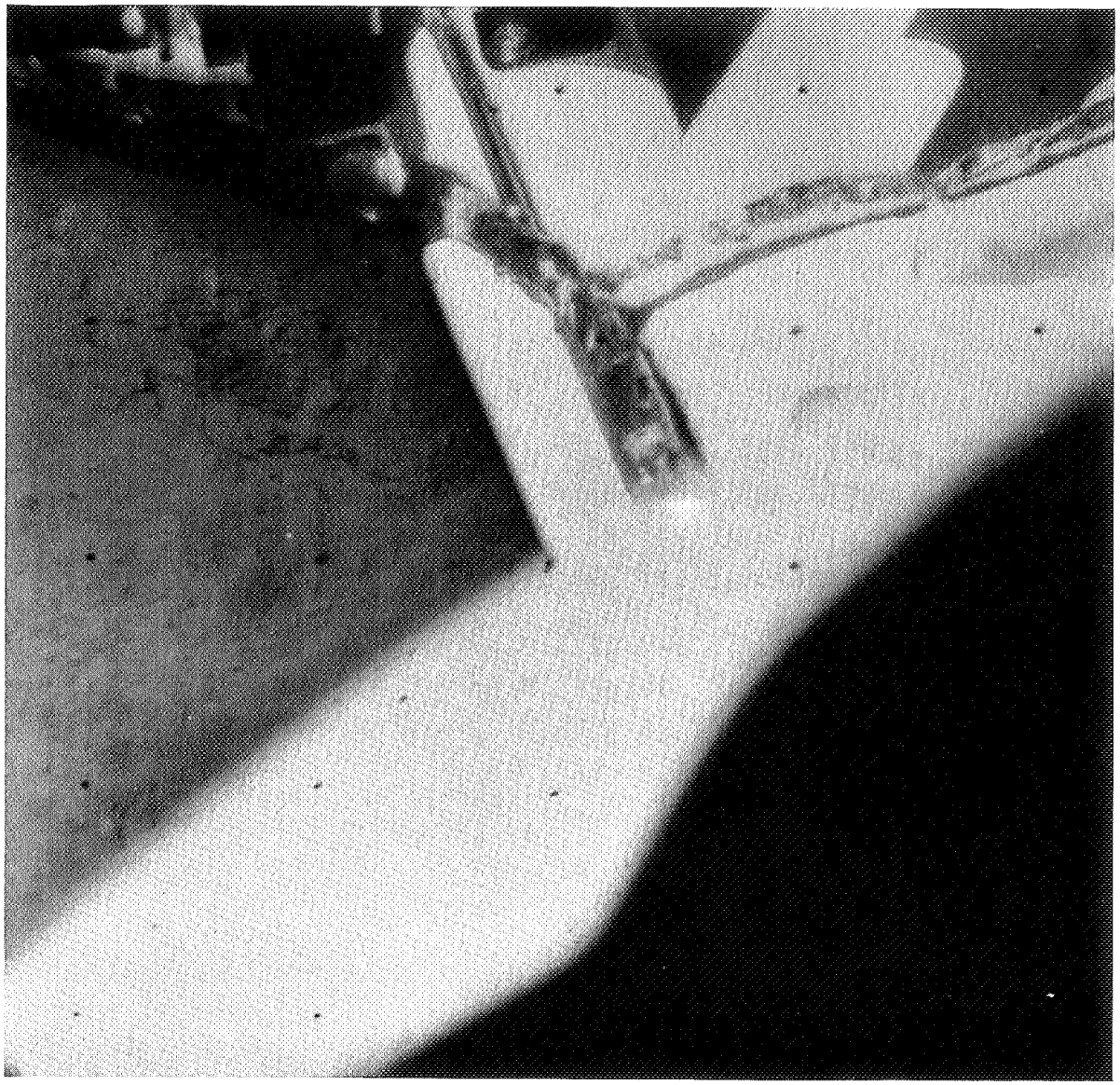

Fig. VI-9. Narrow-angle picture of disturbed lunar surface material near footpad 2. (Disturbed lunar material is in the approximate area in which the exhaust of the attitude control jet impinged on the surface.)

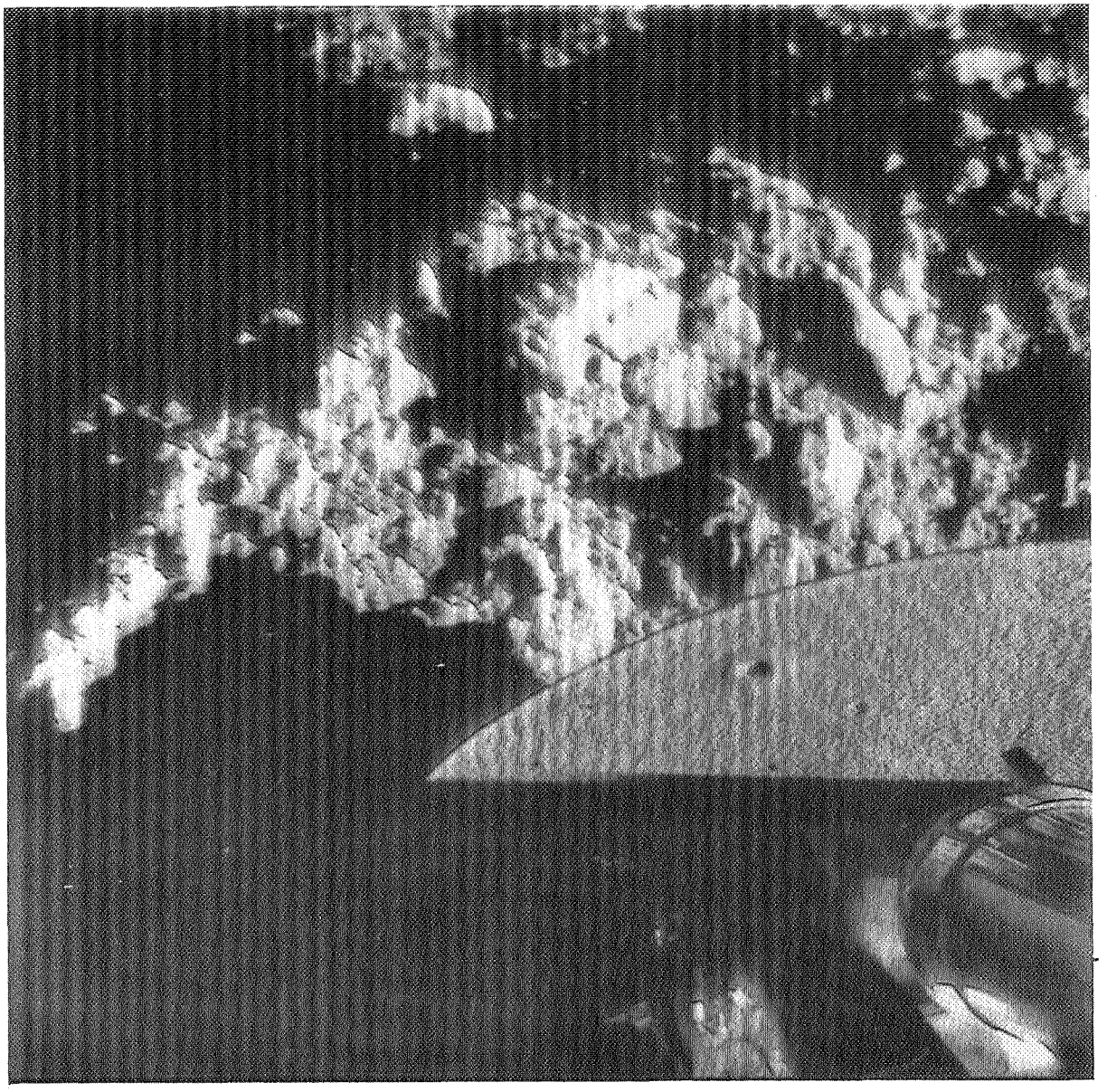

Fig. VI-10. Narrow-angle picture of footpad 2. (Sun angle is 6° above horizon; texture on pad top is unexplained.)

The maximum depth of footpad penetration can only be approximated, particularly since it is not known whether the final position represents the maximum penetration. The penetration of the pads in their final position has been estimated from shadow measurements and observations of numerous photographs. Assuming that there is no pad crushing, the best estimate is that the bottom surface of pad 2 is 4 to 8 cm (1.5 to 3 in.) below the adjacent undisturbed surface (Figs. VI-8 and VI-11); the bottom surface of footpad 3 penetrated at least 3 cm (1.25 in.). By using morning and afternoon shadow measurements, it has been determined that the top of footpad 2 is 9 cm (3.5 in.) above the lunar surface to the west of the footpad and 5 cm (2 in.) above the lunar surface to the east of the pad. The material for approximately 5 to 10 cm (2 to 4 in.) beyond the footpads cannot be seen because the footpads are above the surface, and the camera lines of sight to the far edge of footpads 2 and 3 are, respectively, 46° and 36° below the horizon. The crest of the ridge of disturbed material near footpad 2 is approximately 15 cm (6 in.) beyond the far side of the footpad.

Fig. VI-11. Narrow-angle picture of footpad 3. (Sun angle is 25°; camera angle from which this picture was taken enabled the surface in foreground of footpad to be seen.)

Studies of the low-velocity impact of flat-based objects into cohesionless soils indicate that the crest of the crater formed by the impact occurs less than 1 diameter beyond the edge of the projectile. As the projectile penetrates the soil, some of the material formerly occupying the crater cavity is thrown outward as an overlay, and some material is pushed downward and laterally to form the crater rim. The appearance of the soil and measurements made from the pictures of the *Surveyor I* footpads are compatible with these observations. It can be concluded, therefore, that some of the lunar surface soil was thrown out and some was displaced laterally by the impact of the footpad; however, it is not possible to estimate to what extent the material was volumetrically displaced by the impact because of the area obscured by the footpads.

Pictures of a depression in the lunar surface under (cylindrical) crushable block assembly 3 (Figs. VI-12 and VI-13) indicate that it also made contact with the lunar surface. It has not been possible to identify any lunar surface depression under crushable block assembly 1 because of the spacecraft shadows in that area, including late afternoon shadowing by leg 1. The area beneath crushable block assembly 2 and the crushable blocks themselves cannot be seen with the *Surveyor* TV camera. However, the symmetry of the impact and the general local flatness of

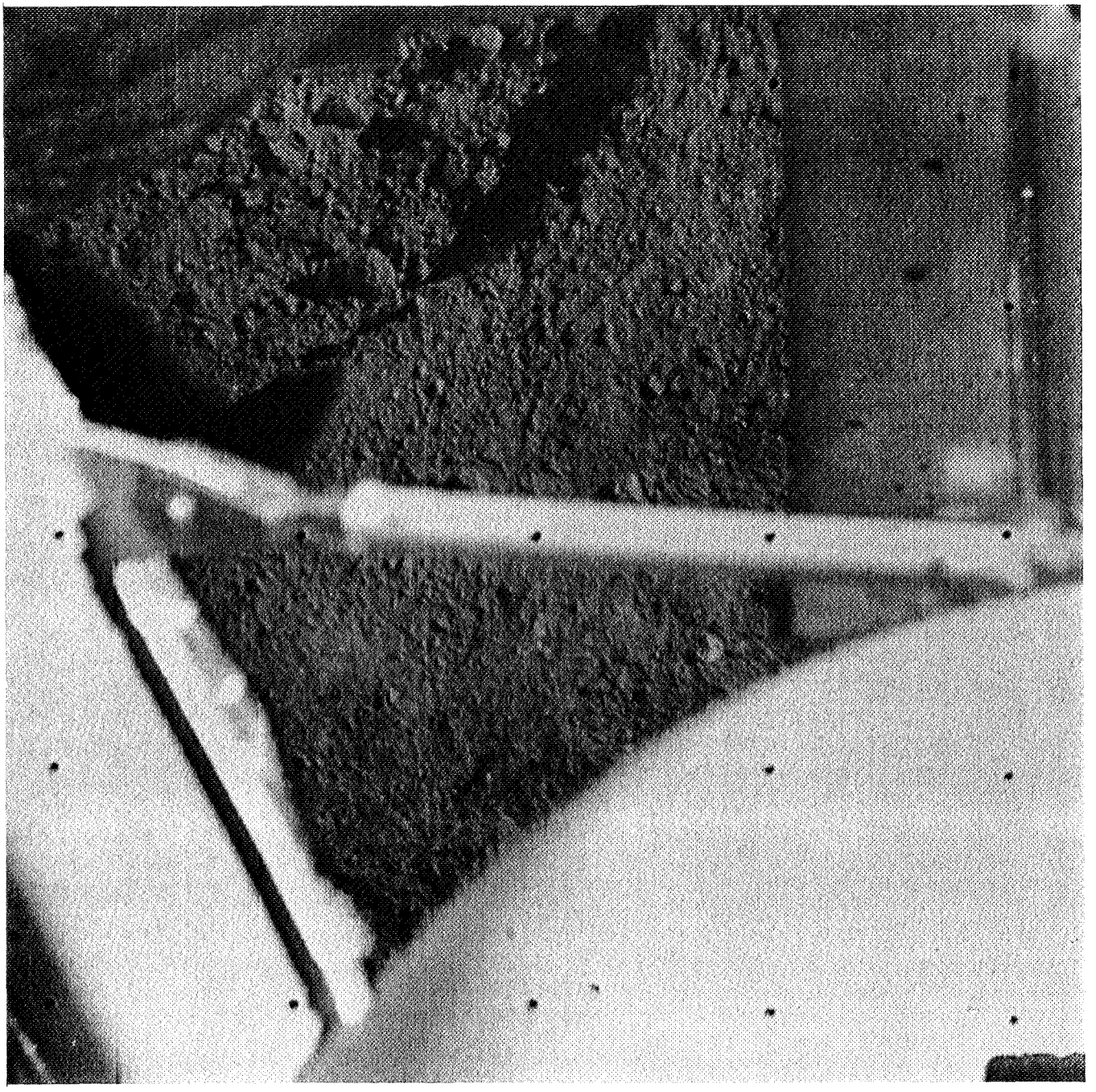

Fig. VI-12. Computer-processed picture of surface depression made by crushable block assembly 3. (Note depression made in upper left-hand corner; part of a propellant tank obscures the imprint in extreme left-hand corner. Sun angle is 41° and from the right of the picture.)

the lunar surface lead to the conclusion that all of the crushable blocks made contact with the lunar surface.

Measurements of depression shadows, made by the block 3 assembly, indicate a depression depth of approximately 2 cm (0.75 in.). The depression, or imprint, (Figs. VI-12 and VI-13) was not made by block 3 itself. The sharp outline of the imprint was made by the thermal insulator that partly surrounds the block (Fig. VI-14). It is conjectured that, as the block penetrated the moon's surface, some lunar material moved outward into the annular segment between the block and insulator. Then, as

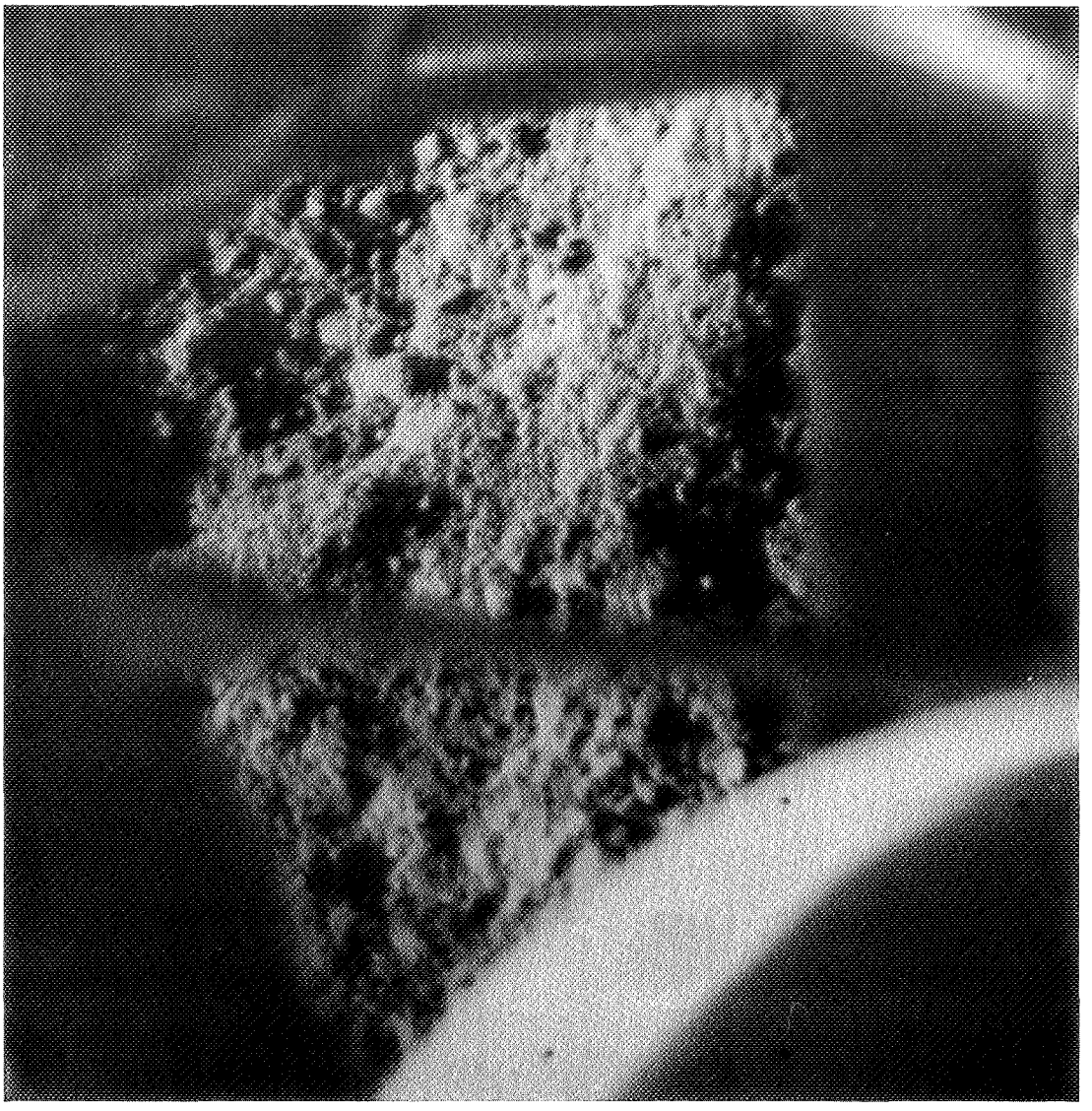

Fig. VI-13. Block assembly imprint taken late on the second lunar day. (Sun angle is 22° and from the left of picture. No noticeable change in the disturbed material has been observed during a time period greater than 5 wk.)

the spacecraft rose, some material remained in the depression. This explains the fact that the lunar material in the imprint does not have a crushed appearance and that the material was not sprayed out around the imprint. Factors that can be postulated from the above and from the study of the pictures are:

(1) Block assembly 3 penetrated more than 2 cm (0.75 in.).

(2) Lunar material is compressible to some extent because an appreciable depression was formed with only a slight visible raising of adjacent material. (This is tentative because of the small percentage of depressed area and of the visible surrounding region.)

(3) Lunar material has cohesion; i.e., the edge remains standing at an angle of at least 58°. (In Figs. VI-12 and VI-13, the edge appears vertical; however, the camera line of sight to block 3 is 58° above the horizon.)

To determine whether any surface erosion could be caused, the attitude-control jet on leg 2 (Figs. VI-3 and VI-7) was operated after landing. This jet used cold nitrogen gas to produce a thrust of 0.06 lb. It was located

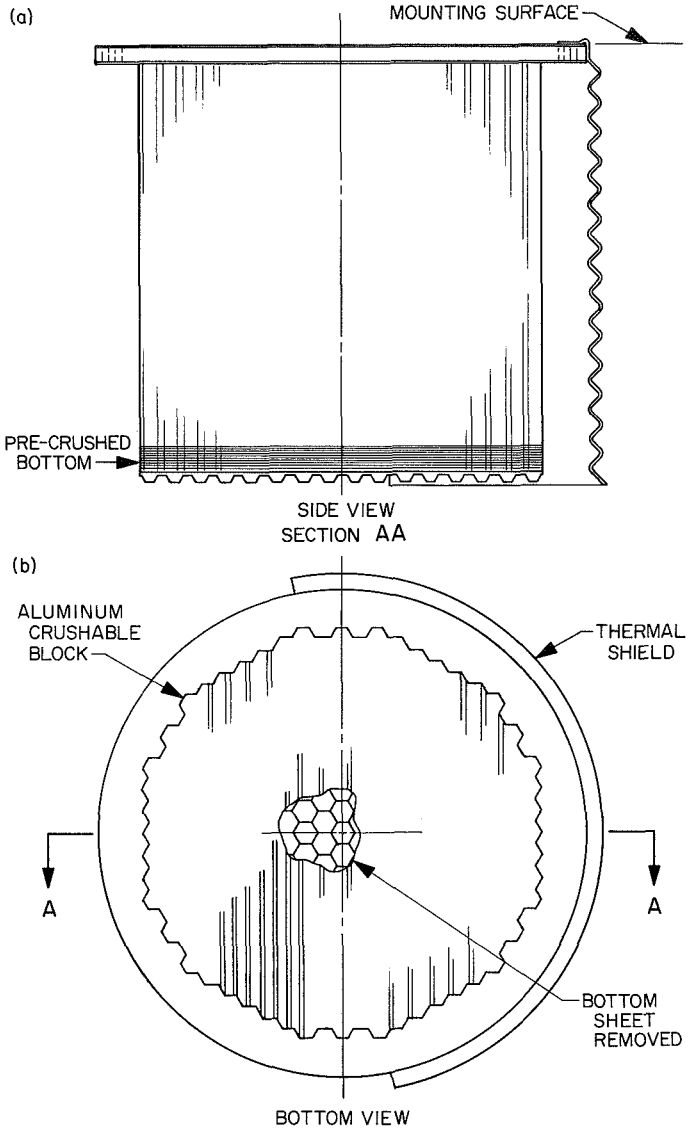

Fig. VI-14. Two views of crushable block assembly 3 including thermal shield: (a) side view and (b) bottom view

approximately 12 cm (5 in.) from, and at an angle of 72° to, the surface. Pictures were taken before, during, and after the firings, which consisted of short pulses repeated for periods up to 12 sec. The pulse duration was 20 msec with a 30-msec pause between pulses. No soil disturbance has been observed except for a single anomaly. Pictures taken after the firing indicate the existence of a slight dimple crater in the surface in the approximate area in which the gas jet struck the lunar material (Fig. VI-9); however, the pictures taken before the firing are inadequate for determining whether the feature was present prior to the firing.

No change in the spacecraft position or attitude has been detected after the landing transient subsided. Within a few minutes after touchdown, locking devices were actuated to prevent any further motion of the shock absorbers, which might result from hydraulic fluid leakage. Examination of late afternoon photographs of the first and second lunar days of the footpad 2 and 3 areas revealed no detectable movements of (1) any lunar particles down to the limit of photographic resolution or (2) the relative position of the pads to the lunar surface. Similarly, no change in the lunar material has been observed around the block 3 imprint.

B. Analysis of Touchdown Dynamics

The spacecraft final descent velocities and attitudes were determined by studying and correlating the velocity data from the radar altimeter and doppler velocity sensor, the three gyro angular rates about the spacecraft axis (as indicated by the gyroscopes), and the precise timing of the final descent and touchdown events. By use of lunar gravity free-fall equations from vernier engine cutoff to touchdown, the vertical landing velocity was calculated. The spacecraft gyro data show that no significant angular motions occurred between vernier engine cutoff and the spacecraft settling onto the surface.

By using the above velocity and spacecraft performance data, analytical simulations of the landing dynamics have been performed. These analyses are based upon extensive computer landing simulation studies, which were confirmed by full-size vehicle drop tests prior to the *Surveyor I* mission (Ref. VI-2). Simulated-landing computer runs were performed assuming a rigid lunar surface as well as a "soft" surface, in which the vertical ground force acting upon each footpad is represented by an equation of the following form:

$$F_V = C_1 + C_2 Z + C_3 \dot{Z}^2$$

where Z represents the penetration into the lunar soil material, $\dot{Z}$ the penetration velocity, and C_1, C_2, and C_3 are characteristic lunar surface coefficients (i.e., C_1 is the force statically exerted by the topmost layer of the lunar surface material, C_2 is the increase in static bearing strength with penetration, and C_3 is the dynamic soil effects). Other soil force equations are under investigation for the determination of potential soft surfaces that would simulate the *Surveyor I* results.

There are various soil types that could have produced the *Surveyor I* strain gage traces and be consistent with the

observed penetrations. However, for all of them, the static bearing strength on the top surface layer must be in the range of 0 to 7×10^5 dynes/cm^2 (0 to 10 psi). For higher values, very little, if any, penetration would have occurred because the maximum dynamic load imposed on the surface by the footpads was approximately 10 psi. Assuming a low value in this range, a rather steep increase in static bearing strength with penetration and/or a high dynamic factor would be required to reproduce the *Surveyor I* results. On the other hand, a high top surface bearing strength (within the above range) would be associated with a small increase in static strength versus penetration and/or a material with a low dynamic effect. Either behavior is conceivable in a homogeneous material, as well as in a layered material. In a homogeneous material, the bearing strength changes versus penetration are continuous; in a layered material, step function changes occur.

To be satisfactory, an evaluation of lunar surface conditions and events during landing must be based on a reasonable comparison between the results of the computer simulations and the observance of the *Surveyor I* landing performance. However, because of the limited amount of available data and the difficulty in determining the footpad penetration accurately, the dynamic analysis may result in a number of different, but adequate, solutions; i.e., it will not necessarily produce conclusive evidence as to the nature of the lunar surface.

Preliminary results of these investigations show that the rigid surface landing agrees well with *Surveyor I* data with respect to pulse shape, elapsed time between first and second impact, and reimpact pulse shape (Fig. VI-5). The time to build up to the peak shock absorber forces was essentially the same for *Surveyor I* and the rigid surface landing simulation. However, for the hard-surface simulations, the peak forces are 10 and 15% too high, and the duration of the first impact pulse is slightly too short. These discrepancies seem to be due primarily to the observed penetration into the lunar material.

To date, some soft surface simulations have been performed that show good correlation with the shock absorber force–time histories through initial and secondary impact. Also, penetrations of footpads and blocks within the limits established by the TV picture analysis have been duplicated by soils that have a bearing strength of 4×10^5 dynes/cm^2 (6 psi) in the top layer and a density of 1.2 to 1.5 g/cm^3 (2.3 to 3.0 slugs/ft^3). However, further investigations are required to extend and confirm these values and to establish limiting relationships between penetration and surface mechanical properties.

Within the limitations of the available data from *Surveyor I*, investigations are continuing as to which of the soil behavior possibilities did exist during the *Surveyor I* landing.

The hard-surface analysis indicates that a landing under the *Surveyor I* conditions should have resulted in very little, if any, footpad crushing, even on an absolutely rigid surface. It is not possible to establish from the TV pictures whether or not any crushing took place.

C. Interpretations

The appearance of the disturbed lunar surface material near the footpads and the rim of the impact depression suggest that the surface is a granular soil-like medium with fine grain size below the resolving capability of the TV system. On disruption by the impact, some fine-grained material was thrown out in a spray, possibly from an original surface layer, and the underlying material was broken up to some extent. It appears that the material displaced by the footpads was both thrown and pushed out.

The behavior of the material is consistent with its possession of a distinct, but small, amount of cohesion; because it is somewhat compressible, its manner of deformation appears to be qualitatively similar to that which might be exhibited by a terrestrial, damp, fine-grained soil.

The appearance of the lunar surface and the nature and depths of the depressions formed during landing are very similar at footpads 2 and 3, so that, at least to the scale of *Surveyor*, the material properties seem to be horizontally homogeneous.

There is an uncertainty in the vertical homogeneity of the lunar surface at the *Surveyor I* landing site. Landing dynamic simulations, to date, are unable to differentiate between a hard surface (static bearing capacity greater than 7×10^5 dynes/cm^2 or 10 psi) overlain by a weaker material to a depth of 2.5 to 7.5 cm (1 to 3 in.), a vertically homogeneous material, or some intermediate material. However, observations of some of the indigenous craters tend to substantiate the vertical homogeneity concept.

The lunar surface did create a maximum dynamic resistance of 4 to 7×10^5 dynes/cm^2 (6 to 10 psi) when *Surveyor I* landed. The static bearing capacity and other

soil properties that would produce such a dynamic effect have not been conclusively determined.

A number of materials that have a wide range of properties can develop a specific static bearing capacity. By assuming a static bearing capability of 4×10^5 dynes/cm^2 (6 psi), one possibility is a soil with a cohesion in the range of 1.3 to 4×10^3 dynes/cm^2 (0.02 to 0.05 psi) and a friction angle between 30° and 40°, at a density typical of terrestrial soil (1.5 g/cm^3, or 3 slugs/ft^3, Fig. VI-15).

In the absence of observable spacecraft settling or physical change of the lunar surface material between the initial and the second lunar day, TV pictures indicate that the lunar material is reasonably stable with respect to the time and temperature changes during that interval.

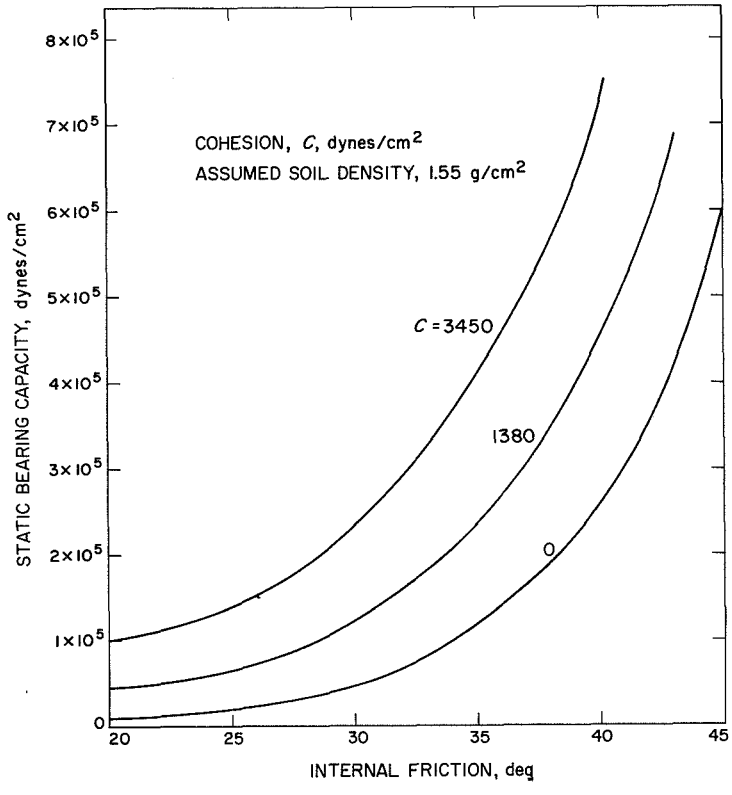

Fig. VI-15. Possible static bearing capacity of a 30.5-cm-diameter footing on moon

REFERENCES

VI-1. *Surveyor I Mission Report: Part I. Mission Description and Performance,* Technical Report No. 32-1023, Jet Propulsion Laboratory, Pasadena, Calif., August 31, 1966.

VI-2. Sperling, F., and Garba, J., *Surveyor I Landing Dynamics,* Technical Report No. 32-1035, Jet Propulsion Laboratory, Pasadena, Calif. (to be published).

ACKNOWLEDGMENT

To acknowledge each of the many persons in various organizations who contributed to this part of this Technical Report would be a lengthy task; therefore, thanks are extended to all for individual efforts. Appreciation is extended particularly to John Garba, JPL, who contributed significantly to the landing dynamic simulation studies; and Robert Spencer and Don Schofield for studies and interpretations of TV pictures with respect to spacecraft interactions with the lunar surface.

VII. ASTRONOMY

R. H. Norton, J. E. Gunn, W. C. Livingston, G. A. Newkirk, and H. Zirin

On June 14, 1966, an attempt was made to photograph the outer solar corona with the *Surveyor I* TV camera after the solar disk had set below the western horizon. On the basis of the dynamic range of the camera system, it was believed possible to record the corona beyond 10 solar radii, i.e., beyond 2.5° from the center of the sun. The predicted setting time of the upper limb of the sun was 15:44 GMT on June 14, 1966. Because of an uncertainty in this time, a picture-taking sequence was initiated at 15:26 GMT. From an azimuth approximately 60° south of west, the camera mirror was gradually stepped westward; at 15:40 GMT, the camera was pointed to the sunset azimuth. Approximately 43 pictures were taken of the solar corona between 15:40 and 16:10 GMT. Four representative pictures are shown in Fig. VII-1, relevant data are given in Table VII-1. In the figure, one of the spacecraft omni-antennas appears to the right of the corona.

No detailed analysis or reduction of the frames, other than a visual examination, has been made at this time; however, two conclusions have been reached from the visual examination: (1) A measurable radiance out to an estimated 3 to 4 solar radii from the center of the disk has been definitely recorded. (2) A very prominent coronal streamer appears on the frames, pointing slightly south of the ecliptic. Comparison of these photographs with ground-based coronal measurements (Fig. VII-2) leaves little doubt concerning the reality of this feature. In Fig. VII-2, the indicated directions are heliocentric; the approximate lunar horizon is shown by the dashed line. On June 14, the ecliptic intersects the western horizon some 2° north of the west point and inclines 3.2° to the north of the local vertical. The apparent slope of the horizon relative to the frames is a function of the azimuth to which the camera points.

One notable feature is that the horizontal extent of the corona is larger than expected, leading one to speculate that some of the diffuse light observed in these frames is due to scattering in a lunar atmosphere or to scattering in the optical system. A decision on such a speculation cannot be made until the data have been thoroughly analyzed and, in fact, may not be possible from the type of observations that have been performed.

Table VII-1. *Surveyor I* TV pictures of solar corona (June 14, 1966)

File	GMT	View angle, deg	Exposure, sec	Iris
36240	15:46:11	6.4	0.15	f/4.0
36246	15:51:32	6.4	1.2	f/5.6
36273	16:02:40	6.4	1.2	f/4.0
36307	16:04:52	25.3	1.2	f/4.0

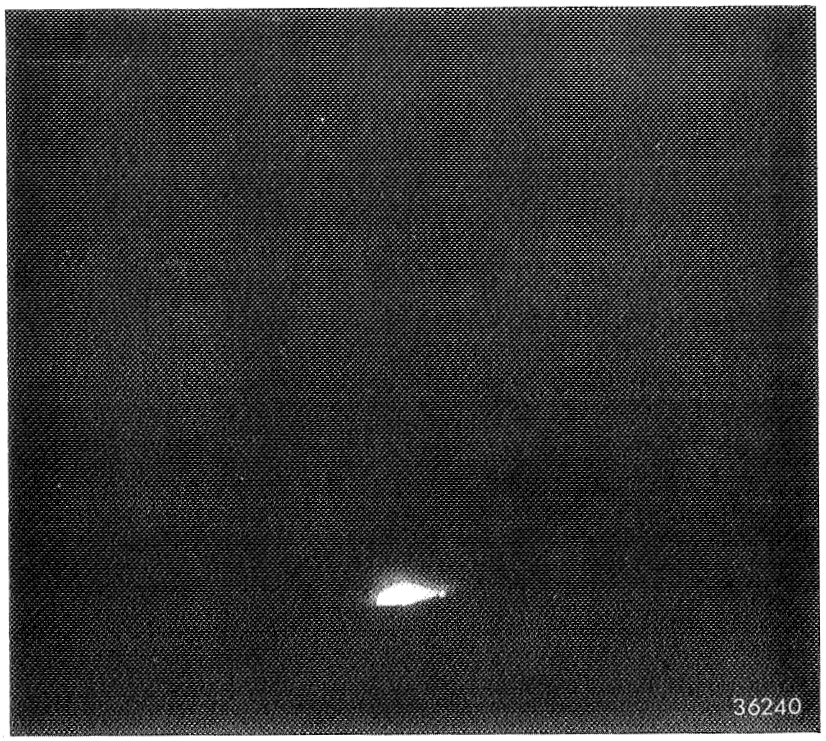

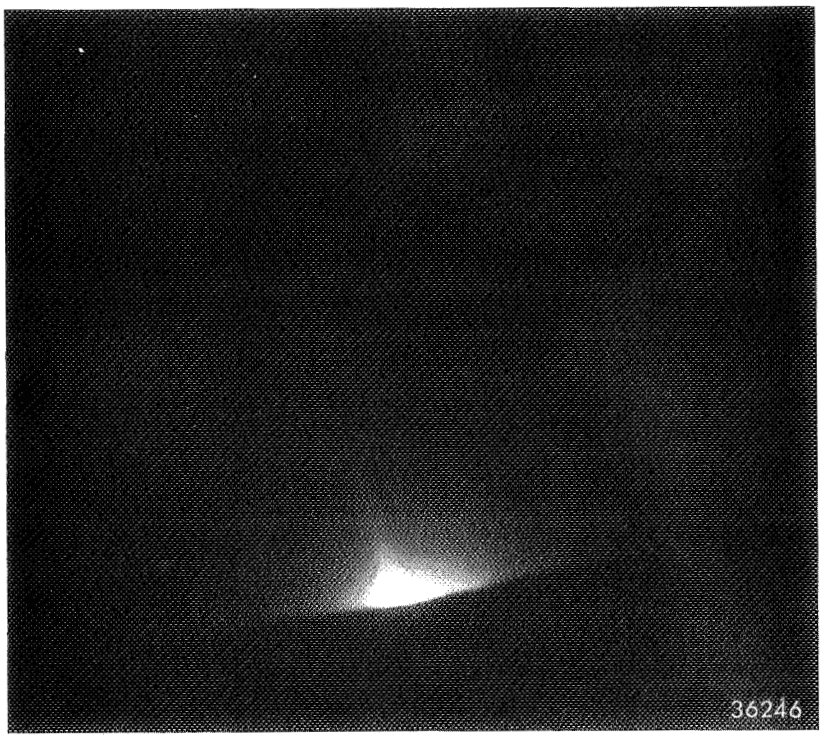

Fig. VII-1. *Surveyor I* pictures of solar corona

Fig. VII-1. *Surveyor I* pictures of solar corona (cont'd)

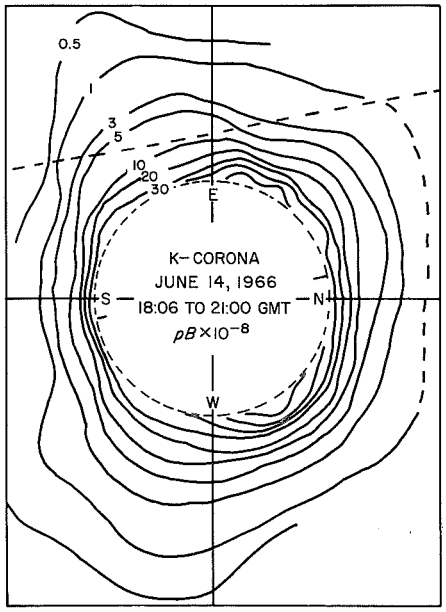

Fig. VII-2. Comparison of *Surveyor I* observations [Fig. VII-2(a)] with ground-based observations [Fig. VII-2(b)]. [Isopleths of product of degree of polarization times radiance in corona are shown in Fig. VII-2(b), which is by courtesy of the High Altitude Observatory.]

ACKNOWLEDGMENT

Appreciation is extended to R. T. Hansen, of the High Altitude Observatory, for the corroborative unpublished K-coronameter observations.

APPENDIX A

Observations of Dust Particles

W. A. Hagemeyer

On June 11, 1966, and July 12, 1966, TV pictures were taken of the compartment radiators, which are located on the top of thermal compartments A and B (shown in Fig. IV-17 of Ref. A-1). These radiators are Vycor glass mirrors, aluminized on the back surface. On June 11, a color survey was taken of one location on the top of each of the compartments. On July 12, a complete survey was taken of the top of compartment A and a duplicate of the location on the top of compartment B, through only the clear filter.

A comparison of identical pictures, taken on the separate lunar days, has revealed some changes in apparent dust locations.

Figure A-1(a) and (b) shows the top of compartment A on June 11 and on July 12. The circled areas in the pictures indicate particles that do not appear in the other picture. Note that particles that appear on June 11 do not appear on July 12 and vice versa. Fig. A-1(b) shows a portion of a radiator mirror, which apparently broke during the lunar night. (This broken mirror is shown more clearly in Fig. A-2). Some of the new particles may be pieces of the broken mirror. The energy released by the breakage of this mirror would not be expected to dislodge particles on adjacent radiators.

Figure A-3(a) and (b) shows compartment B on June 11 and on July 12, both through the clear filter. Note that there are not as many differences readily apparent. However, several particles have apparently disappeared, while at least one new one has appeared. No radiator mirrors were broken on this compartment.

Prior to final encapsulation within the nose fairing, the spacecraft was thoroughly cleaned to minimize the number of loose particles.

During the launch operations, the spacecraft was continuously bathed in a stream of conditioned air, filtered through a 0.3-micron filter. The air conditioning system is known to deposit small fibers, not particulate matter.

Subsequent to the *Surveyor I* flight, a camera similar to that used on the spacecraft was used in the laboratory to take pictures of various substances on a similar radiator. A sun elevation angle of 60°, measured from the sunset location for *Surveyor I*, was simulated. These photographs could not detect fibrous lint-type particles (Fig. A-4). Ordinary sand, with particle sizes varying from 0.075 mm (0.005 in.) to 2.5 mm (0.1 in.), produced an effect similar to that seen on the moon (Fig. A-5).

The large circular spots are plugs covering the radiator attachment screws. These plugs are 5.00 mm (0.200 in.) in diameter. The mirror is 0.500 mm (0.020 in.)-thick glass, bonded to a tapered aluminum substrate that has a minimum thickness of 1 mm (0.040 in.). Each radiator consists of four of the mirror segments with one attachment screw through each segment. Radiators are aligned perpendicular to the spacecraft Z-Z axis, within a tolerance of approximately 5°.

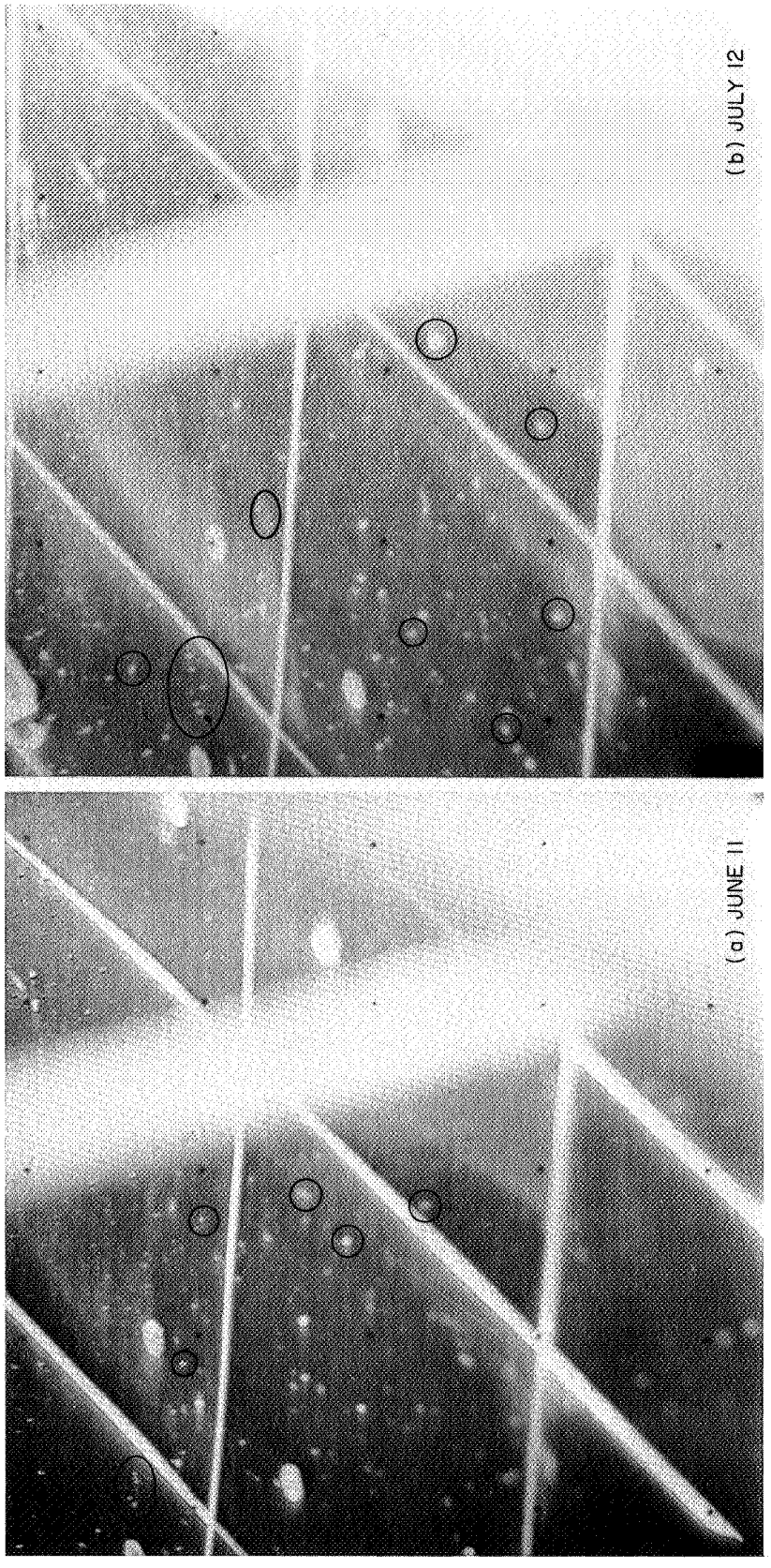

Fig. A-1. Top of thermal compartment A

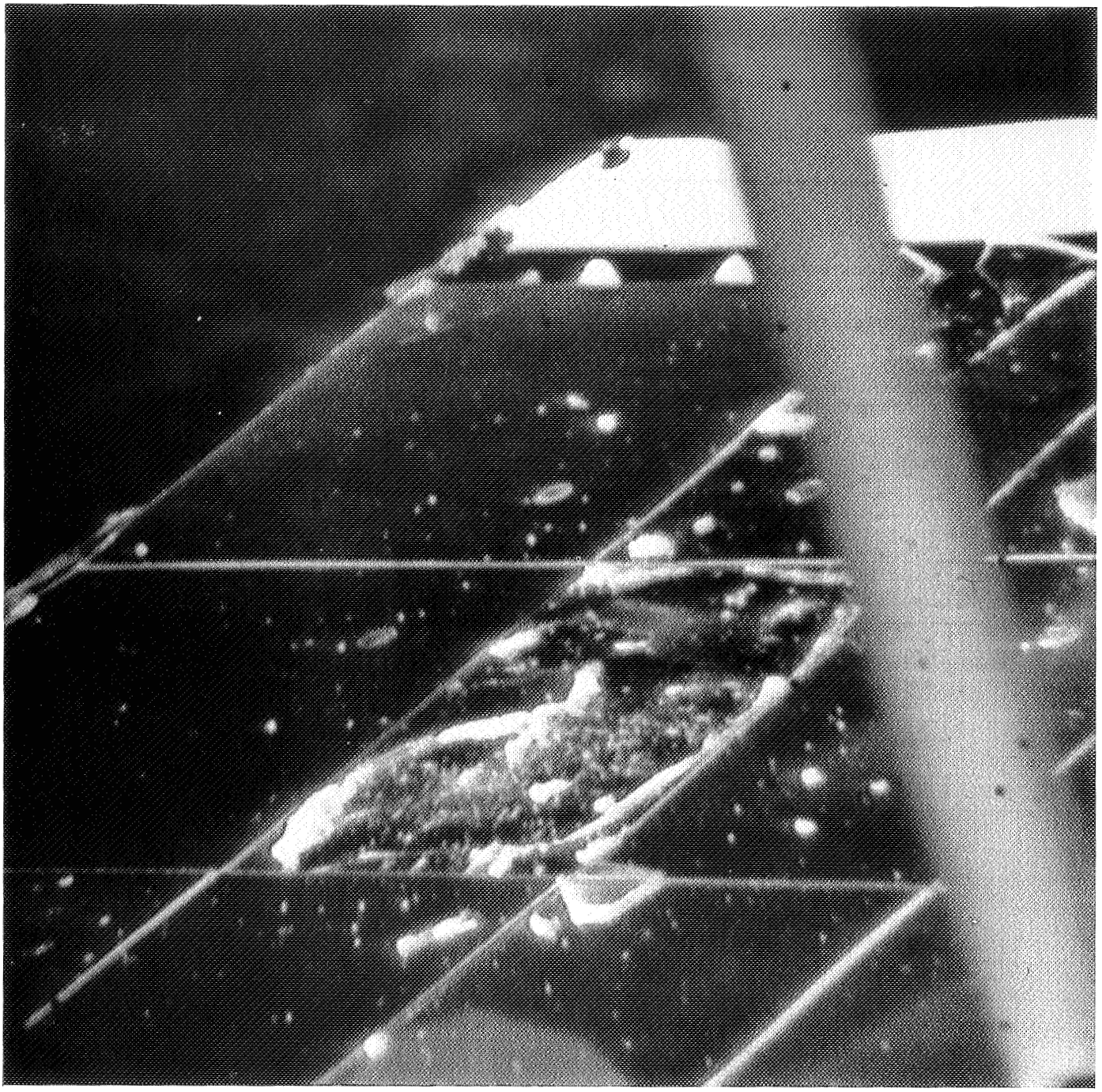

Fig. A-2. Compartment A on July 12, showing one segment of Vycor glass presumably shattered during lunar night

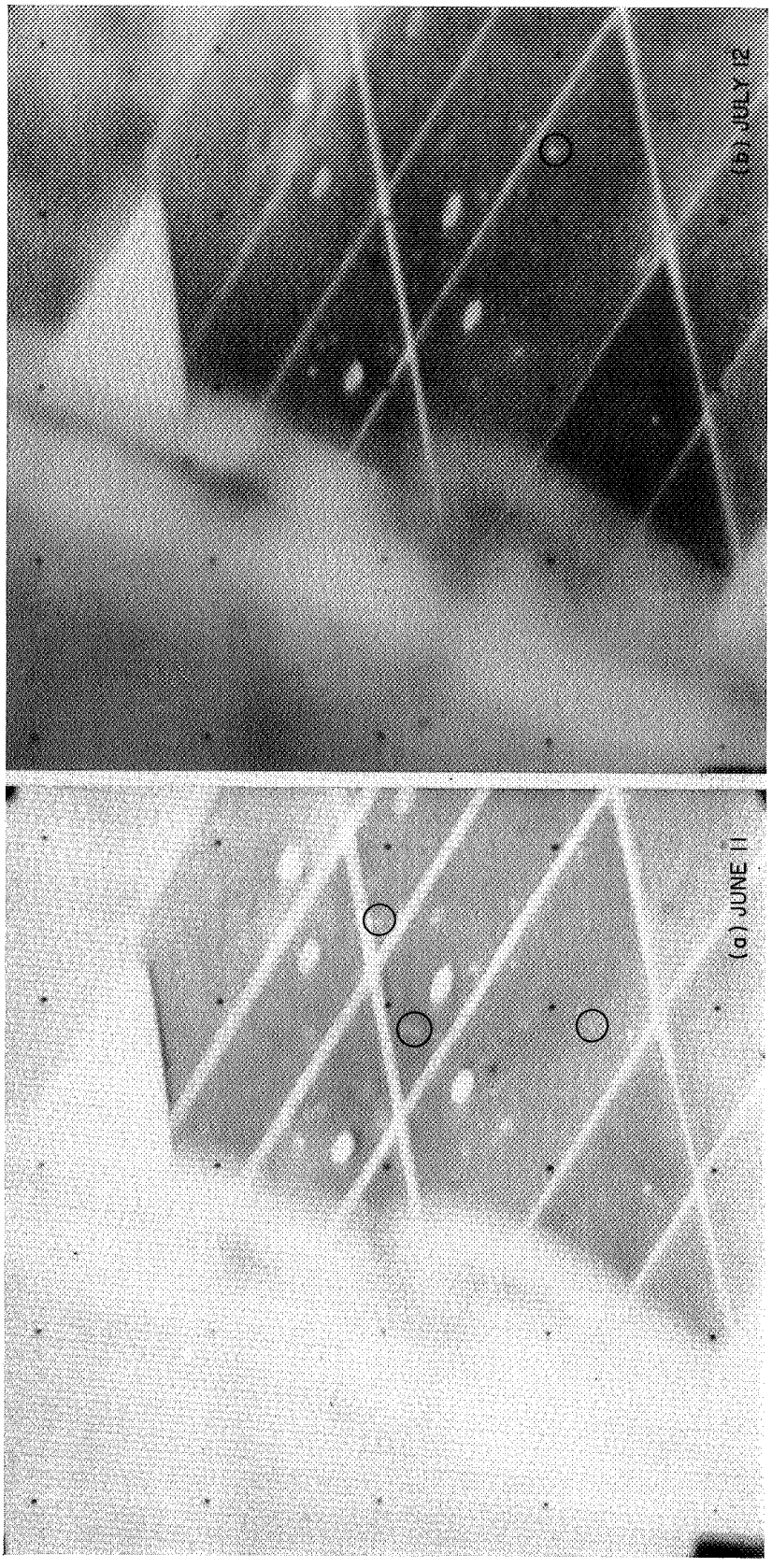

Fig. A-3. Top of thermal compartment B. (Both pictures were taken through clear filter.)

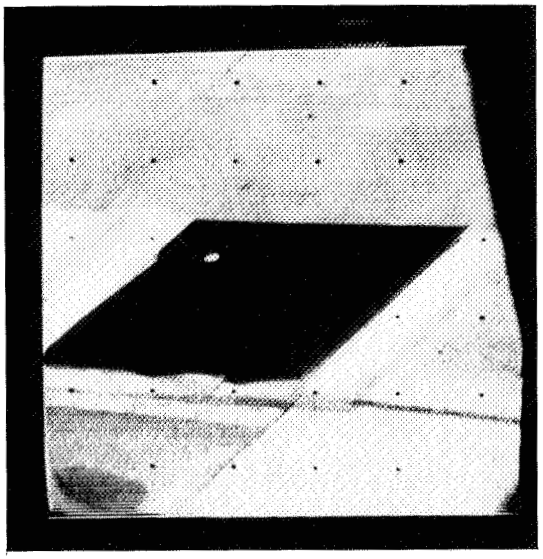

Fig. A-4. Polaroid picture of substances on radiator: ordinary room lint

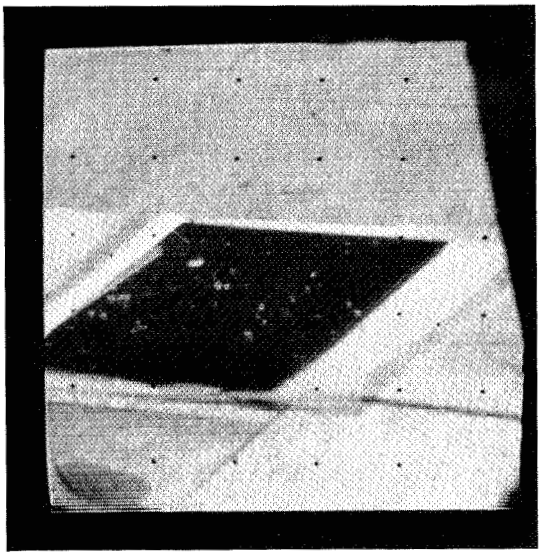

Fig. A-5. Polaroid picture of substances on radiator: largest particle 2.500 mm (0.100 in.); 100-mm focal length

REFERENCE

A-1. *Surveyor I Mission Report: Part I. Mission Description and Performance*, Technical Report No. 32-1023, Jet Propulsion Laboratory, Pasadena, Calif., August 31,1966.

APPENDIX B

Surveyor Scientific Evaluation Advisory Team and Working Groups

L. D. Jaffe

The *Surveyor* Scientific Evaluation Advisory Team was established to provide advice concerning scientific interpretation of data obtained from *Surveyor* engineering test flights. In addition to the main advisory team, five associated working groups were formed to provide more detailed consideration of specific technical areas. Advisory team members include the Principal Investigators on later *Surveyor* missions, the Jet Propulsion Laboratory *Surveyor* Project Scientist, and the National Aeronautics and Space Administration *Surveyor* Program Scientist. Part II of this mission report was prepared primarily by these groups. Membership for *Surveyor I* was as follows:

A. Surveyor Scientific Evaluation Advisory Team

L. D. Jaffe, Chairman	Jet Propulsion Laboratory
W. M. Alexander	Temple University
S. A. Batterson	Langley Research Center
S. E. Dwornik	NASA Headquarters
R. F. Scott	California Institute of Technology
E. M. Shoemaker	U. S. Geological Survey
G. H. Sutton	Columbia University
A. Turkevich	University of Chicago

B. Working Groups

1. Lunar Surface Topography

T. Vrebalovich, Chairman	Jet Propulsion Laboratory
W. M. Alexander	Temple University
T. H. Bird	Jet Propulsion Laboratory
J. L. Dragg	Manned Spacecraft Center
E. C. Morris	U. S. Geological Survey
J. J. Rennilson	Jet Propulsion Laboratory
E. M. Shoemaker	U. S. Geological Survey
A. Turkevich	University of Chicago

2. Lunar Surface Thermal Properties

J. W. Lucas, Chairman	Jet Propulsion Laboratory
J. E. Conel	Jet Propulsion Laboratory
R. B. Erb	Manned Spacecraft Center
R. R. Garipay	Hughes Aircraft Company
W. A. Hagemeyer	Jet Propulsion Laboratory
A. Lachenbruch	U.S. Geological Survey
J. M. Saari	The Boeing Company

3. Lunar Surface Electrical Properties

W. E. Brown, Jr., Chairman	Jet Propulsion Laboratory
A. R. Barringer	Barringer Research, Ltd.
R. A. Dibos	Hughes Aircraft Company
A. E. Dickinson	Jet Propulsion Laboratory
G. B. Gibson	Manned Spacecraft Center
D. O. Muhleman	Cornell University

4. Lunar Surface Mechanical Properties

E. M. Christensen, Chairman	Jet Propulsion Laboratory
S. A. Batterson	Langley Research Center
H. E. Benson	Manned Spacecraft Center
C. E. Chandler	Jet Propulsion Laboratory
R. H. Jones	Hughes Aircraft Company
R. F. Scott	California Institute of Technology
E. N. Shipley	Bellcomm, Inc.
F. B. Sperling	Jet Propulsion Laboratory
J. A. Stallkamp	Jet Propulsion Laboratory
G. H. Sutton	Columbia University

5. Astronomy

R. H. Norton, Chairman	Jet Propulsion Laboratory
J. E. Gunn	Jet Propulsion Laboratory
W. C. Livingston	Kitt Peak National Observatory
G. A. Newkirk	High Altitude Observatory
H. Zirin	Mt. Wilson and Palomar Observatories